

Graz University of Technology  
Faculty of Civil Engineering  
Institute of Hydraulic Structures and Water Resources Management  
Hermann-Grengg Laboratories Graz

# ULTRASONIC VELOCITY PROFILE MEASUREMENTS IN EXPERIMENTAL HYDRAULICS

Diploma Thesis  
by  
Thomas Geisler

Submitted in Partial Fulfillment of  
the Requirements for the Degree of  
*“Diplom-Ingenieur”*  
of Civil Engineering / Economics

Graz, Austria

June 2001

Revised in December 2002

Dipl.-Ing. Thomas Geisler

Institute of Hydraulic Structures and Water Resources Management  
Graz University of Technology, Austria  
Stremayrgasse 10, A-8010 Graz

Tel: +43 316 873-8351, Fax: +43 316 873-8357  
e-mail: [thomas.geisler@TUGraz.at](mailto:thomas.geisler@TUGraz.at)

We approve the thesis of Thomas Geisler.

A handwritten signature in black ink, appearing to read 'Roman Klasinc', written over a horizontal line.

Prof. Roman Klasinc  
Head of Hermann-Grengg Laboratories  
Thesis Advisor

A handwritten signature in black ink, appearing to read 'Helmut Knoblauch', written over a horizontal line.

Helmut Knoblauch  
Assistant Professor

Meinen Eltern,

Josefa und Ernest Geisler,

und meiner Freundin Klaudia,

in Liebe und Dankbarkeit.

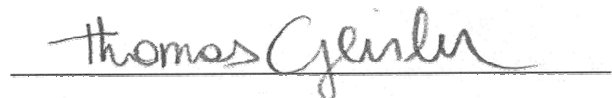
---

## Erklärung

---

Ich erkläre hiermit, dass ich die vorliegende Arbeit nach bestem Wissen und Gewissen selbstständig und ohne fremde Hilfe verfasst, andere als die angegebenen Quellen nicht benutzt und die wörtlich oder inhaltlich entnommenen Stellen als solche gekennzeichnet habe.

Graz, im Juni 2001

A handwritten signature in cursive script that reads "Thomas Geisler". The signature is written in black ink and is positioned above a horizontal line.

Thomas Geisler

---

## Kurzfassung

---

Das Ultraschall-Puls-Doppler Verfahren zur nicht-invasiven Messung von Geschwindigkeitsprofilen stellt eine der neuesten Entwicklungen im wasserbaulichen Versuchswesen dar. Das Verfahren gestattet die unmittelbare Messung der Geschwindigkeit an einer Vielzahl von Punkten innerhalb des Schallkegels, wodurch sowohl eine räumliche als auch eine zeitliche Erfassung der zu untersuchenden Strömung möglich wird. Herkömmliche Instrumente müssen dagegen aufgrund ihrer punktförmigen Messung immer wieder neu positioniert werden, um ein komplettes Geschwindigkeitsprofil aufzunehmen.

Mit dem Erwerb des UVP-Monitor XW-3-PSi der Firma Met-Flow steht dieses Verfahren im Hermann-Grengg Laboratorium der Technischen Universität Graz zur Verfügung. Mit diesem Gerät wurden neben der Messung von Geschwindigkeitsprofilen in voll durchströmten Rohrleitungen und in offenen Gerinnen auch Wasserstandsmessungen durchgeführt. Die vorliegende Arbeit präsentiert die durchgeführten Versuche, widmet sich aber auch ausführlichst der Erzeugung und Ausbreitung von Ultraschall sowie der Messmethodik.

Versuche an Plexiglas-Rohren verschiedenen Durchmessers bestätigen die Eignung des UVP-Monitors zur berührungslosen Geschwindigkeitsmessung. Die Untersuchungen am offenen Gerinne werden indessen durch Reflexionen der Ultraschallwellen an der Wasseroberfläche und der Gerinnesohle beeinträchtigt. Die gleichzeitige Messung der Geschwindigkeitsprofile und der Wasserstände konnte zur Zeit noch nicht zufrieden stellend verwirklicht werden.

### *Schlagwörter:*

Ultraschall-Puls-Doppler Verfahren; Geschwindigkeitsmessung; Wasserbauliches Versuchswesen; UVP-Monitor; Rohrhydraulik; Gerinnehydraulik; Wasserstandsmessung

---

## Abstract

---

Velocity measurements provide the fundamental data on which hydraulic analysis and design is based. The ultrasound-pulse-Doppler method for the non-intrusive measurement of entire velocity profiles is one of the latest advances in fluid engineering. In contrast to conventional measurement techniques, where the measurement apparatus has to be moved to detect a complete velocity profile, the ultrasound-pulse-Doppler method offers instantaneous results, thereby allowing calculation of flow as a function of both space and time.

An ultrasound-pulse-Doppler device, the UVP-Monitor model XW-3-PSi from Met-Flow, was recently acquired by the Hermann-Grengg Laboratories. This thesis reports on the results of employing the UVP-Monitor in the studies of both pipe flow and open channel flow. A broad review of the generation and propagation of ultrasound is given, followed by a detailed description of the measurement technique and the experiments performed to test the technique in practical application.

Measurements conducted on Plexiglas pipes of various diameters demonstrate the ability of the UVP-Monitor to investigate pipe flow non-intrusively. The study of open channel flow, however, is found to be affected by multiple ultrasound reflections between the free surface and the bottom of the channel. Attempts to measure surface level and flow velocities simultaneously show less promising results, but improvements may be made in the future.

*Keywords:*

Ultrasound-pulse-Doppler method; Velocity measurement; Experimental hydraulics; UVP-Monitor; Pipe flow; Open channel flow; Surface level measurement

---

## Acknowledgements

---

As with most projects, teamwork delivers the best results. This thesis is no exception and I wish to express my gratitude to the people below who participated in the successful completion of my work.

Prof. Roman Klasinc shared his substantial knowledge in experimental hydraulics and gave guidance in all aspects of the research. Helmut Knoblauch offered universal support and continuously encouraged me during the writing of this thesis. Gerald Schweighofer introduced me to the UVP-Monitor, while Walter Felgitsch, Walter Hubinger and Joachim Steingruber helped in the various experiments. Olivier Mariette, Technical Specialist of Met-Flow, provided helpful advice and graciously allowed the reproduction of some of his figures in this thesis.

I would also like to thank Stephen Berkebile for the proofreading. He was an excellent reviewer and has offered many helpful suggestions and criticisms.

Prof. Roman Klasinc and Prof. Günther Heigerth, Head of the Institute of Hydraulic Structures and Water Resources Management, are grateful to the Oesterreichische Nationalbank for partially funding the instrumentation for ultrasonic velocity profile measurements at the Hermann-Grengg Laboratories Graz.



---

## Table of Contents

---

|  |      |
|--|------|
| LIST OF FIGURES.....                     | xii  |
| LIST OF TABLES .....                     | xvii |
| 1 INTRODUCTION.....                      | 1    |
| 1.1 Thesis Motive.....                   | 2    |
| 1.2 Research Objectives .....            | 2    |
| 1.3 Tasks Completed.....                 | 2    |
| 1.4 Thesis Contents .....                | 3    |
| 2 GENERAL PROPERTIES OF ULTRASOUND ..... | 5    |
| 2.1 Ultrasonic Waves .....               | 5    |
| 2.2 Acoustic Velocity.....               | 6    |
| 2.3 Acoustic Impedance .....             | 8    |
| 2.4 Scattering.....                      | 10   |
| 2.5 Attenuation.....                     | 13   |
| 2.6 Reflection and Refraction.....       | 16   |
| 2.7 Generation of Ultrasound.....        | 20   |
| 2.8 Transducer Design.....               | 23   |
| 2.9 Ultrasonic Sound Field.....          | 26   |

|      |   |    |
|------|---|----|
| 3    | ULTRASONIC VELOCITY PROFILE MEASUREMENTS..... | 31 |
| 3.1  | Doppler Effect.....                           | 32 |
| 3.2  | Principle of Ultrasound-Pulse-Doppler.....    | 35 |
| 3.3  | Doppler Angle.....                            | 37 |
| 3.4  | Signal Sampling.....                          | 39 |
| 3.5  | Measurable Depth and Measurable Velocity..... | 41 |
| 3.6  | Measurement Window.....                       | 44 |
| 3.7  | Spatial Resolution.....                       | 47 |
| 3.8  | Velocity Resolution.....                      | 49 |
| 3.9  | Temporal Resolution.....                      | 50 |
| 3.10 | Measurement Equipment.....                    | 52 |
| 4    | INVESTIGATION OF PIPE FLOW.....               | 55 |
| 4.1  | General Test Setup.....                       | 56 |
| 4.2  | Measurement Planes.....                       | 58 |
| 4.3  | Particle Seeding.....                         | 60 |
| 4.4  | Software Parameter.....                       | 61 |
| 4.5  | Validation of Transmission Angle.....         | 63 |
| 4.6  | Turbulent Flow and Velocity Average.....      | 65 |
| 4.7  | Analysis of Sample Profiles.....              | 67 |
| 4.8  | Computation of Pipe Discharge.....            | 73 |
| 4.9  | Summary.....                                  | 78 |

|     |                                       |    |
|-----|---------------------------------------|----|
| 5   | STUDY OF OPEN CHANNEL FLOW.....       | 79 |
| 5.1 | Test Facilities .....                 | 80 |
| 5.2 | Measurement of Velocity Profiles..... | 80 |
| 5.3 | Identification of Artifacts .....     | 83 |
| 5.4 | Surface Level Measurement.....        | 84 |
| 5.5 | Summary .....                         | 90 |
| 6   | CONCLUSIONS AND RECOMMENDATIONS.....  | 91 |
| 7   | REFERENCES.....                       | 93 |

---

## List of Figures

---

|   |    |
|---|----|
| Figure 1-1: Main testing floor at the Hermann-Grengg Laboratories Graz. ....  | 1  |
| Figure 2-1: Propagation of sound. Longitudinal waves (left) and transverse waves (right). ....                                    | 5  |
| Figure 2-2: Speed of sound versus temperature in pure water. ....   | 8  |
| Figure 2-3: Scattering. Point reflector (left) and rough interface (right).....   | 10 |
| Figure 2-4: Monopole (a) and dipole (b) radiation together compose Rayleigh scattering (c). ....                                  | 11 |
| Figure 2-5: Mie scattering of a rigid (solid line) and an elastic (dashed) spherical scatterer. ....                              | 12 |
| Figure 2-6: Backscatter amplitude of Rayleigh scatterers (a) and particles in the Mie regime (b). ....                            | 12 |
| Figure 2-7: Attenuation of ultrasound for four different frequencies<br>in water as a function of distance. ....                  | 14 |
| Figure 2-8: Attenuation function of Plexiglas. ....   | 15 |
| Figure 2-9: Change of pulse waveform due to attenuation and dispersion;<br>transmitted pulse (left), received pulse (right). .... | 15 |
| Figure 2-10: Reflection and refraction of ultrasound on interface. ....   | 16 |
| Figure 2-11: Critical angle of incidence. ....  | 17 |
| Figure 2-12: Acoustic pressure at the boundary of steel and water for normal incidence. ....                                      | 19 |
| Figure 2-13: Transmission coefficients for several wall materials<br>as a function of the angle of incidence. ....                | 19 |
| Figure 2-14: Direct (above) and converse (below) piezoelectric effect. ....   | 21 |
| Figure 2-15: Schematic representation of a 1-3 piezo-composite plate. ....  | 22 |
| Figure 2-16: Sample pictures of immersion transducers (left) and contact transducers (right). ....                                | 23 |
| Figure 2-17: Main components of an ultrasonic transducer. ....  | 23 |

|   |    |
|---|----|
| Figure 2-18: Shortest possible pulses obtained from a transducer a) without and b) with backing layer (left) and the Fourier transform of the pulses (right). | 24 |
| Figure 2-19: Layer structure of an immersion transducer.  | 25 |
| Figure 2-20: Schematic illustration of the formation of an ultrasonic beam.   | 26 |
| Figure 2-21: Influence of excitation mode on the axial sound pressure in the near-field region.   | 27 |
| Figure 2-22: Axial sound pressure in the far-field region and its approximation.  | 28 |
| Figure 2-23: Angular variation of the beam amplitude in the far-field region; CW (a) and PW (b) excitation.   | 29 |
| Figure 3-1: Ultrasonic velocity profile measurements of open channel flow.  | 31 |
| Figure 3-2: Doppler effect for sound waves; moving receiver (a), moving source (b), and moving reflector (c).   | 32 |
| Figure 3-3: Functional principle of ultrasound-pulse-Doppler.   | 35 |
| Figure 3-4: Doppler angle variation for a given flow direction and its effect on the detected velocity component.   | 37 |
| Figure 3-5: Effect of Doppler angle error on velocity measurement.  | 38 |
| Figure 3-6: Sampling of a sine wave using a frequency (a) above and (b) below twice the Nyquist frequency ( $2f_N$ ).   | 40 |
| Figure 3-7: Backfold of detected frequency due to aliasing.   | 40 |
| Figure 3-8: Relationship between measurement depth and measurable velocity for common working frequencies.  | 42 |
| Figure 3-9: Measurable velocity for an operating frequency of 2 MHz as a function of the Doppler angle $\alpha$ .   | 43 |
| Figure 3-10: Measurable velocity for an operating frequency of 4 MHz as a function of the Doppler angle $\alpha$ .  | 43 |
| Figure 3-11: Terms related to the measurement window and their position inside the ultrasonic beam.   | 45 |

|  |    |
|--|----|
| Figure 3-12: Sampling of the gated echo signal at specific times separated by the time interval $\Delta t_s$ . ..    | 46 |
| Figure 3-13: Relationship between channel width and distance.<br>Regular (a) and overlapping (b) volumes.....        | 48 |
| Figure 3-14: Effect of high (a) and low (b) velocity resolution. ....  | 50 |
| Figure 3-15: Timing of velocity profile measurements with<br>multitasking operating system (Windows NT).....         | 50 |
| Figure 3-16: Temporal resolution as a function of measurement depth and<br>pulse repetitions per profile.....        | 52 |
| Figure 3-17: UVP Monitor model XW-PSi. Main unit (left) and transducer (right). ....                                 | 53 |
| Figure 3-18: Sample screenshot of UVP-XW online software (version 2.1). ....   | 54 |
| Figure 4-1: Inverted siphon model "Düker Oitenbach" as viewed in flow direction. ....                                | 55 |
| Figure 4-2: Test pipes, numbered 1 to 3 (according to size).<br>Overview (left) and close-up of elbows (right). .... | 56 |
| Figure 4-3: Inlet structure of the inverted siphon at low (left) and medium (right)<br>discharge conditions.....     | 57 |
| Figure 4-4: Positioning of the transducer (a) and measurement planes<br>as viewed in the direction of flow (b).....  | 58 |
| Figure 4-5: Support for fixing the transducer on the pipes. ....   | 59 |
| Figure 4-6: Position of test sections along the pressure pipes of the inverted siphon.....                           | 59 |
| Figure 4-7: Sediment feeder used for flow seeding.....   | 60 |
| Figure 4-8: Refraction of ultrasound at the pipe wall. General case (a) and test situation (b). ....                 | 63 |
| Figure 4-9: Relationship between transmission angle, measurement line and pipe diameter. ....                        | 64 |
| Figure 4-10: Random particle movement (a) in turbulent flow<br>causes velocity fluctuation over time (b). ....       | 65 |
| Figure 4-11: Mean time average profile computed with all velocities included (All). ....                             | 66 |

|   |    |
|---|----|
| Figure 4-12: Same data, but average profile computed without zero velocities (Zero).....                                | 66 |
| Figure 4-13: Sample velocity profile obtained at section m on pipe 1<br>showing undistorted turbulent flow.....         | 67 |
| Figure 4-14: Reflection at the back wall of a straight pipe<br>causes axial symmetry of the velocity profile. ....      | 68 |
| Figure 4-15: Sample velocity profile obtained at section de2 on pipe 3<br>showing distorted turbulent flow.....         | 69 |
| Figure 4-16: Flow pattern at the elbow showing strong eddies at the inward bend . ....                                  | 70 |
| Figure 4-17: Color plot of sample profile m on pipe 1 showing<br>velocity fluctuations (F) and rear pipe wall (R). .... | 71 |
| Figure 4-18: Color plot of sample profile de2 on pipe 3 showing<br>irregular flows patterns (*) and artifacts (A). .... | 72 |
| Figure 4-19: Flow rate computation by means of velocity profile measurements. ....                                      | 74 |
| Figure 4-20: Computation of pipe discharge as implemented in the in UVP-MFX review program. ...                         | 75 |
| Figure 4-21: Velocity profiles obtained at section m on pipe 1<br>showing undistorted symmetrical flow. ....            | 77 |
| Figure 4-22: Velocity profiles obtained at section m on pipe 3 showing severe profile distortions. ....                 | 77 |
| Figure 5-1: Contours of constant velocity (left) and velocity profile (right)<br>for flow in narrow channels.....       | 79 |
| Figure 5-2: Test facilities for employing the UVP-Monitor in the study of open channel flow. ....                       | 80 |
| Figure 5-3: Experimental setup for velocity profile measurements in wavy flow. ....                                     | 81 |
| Figure 5-4: Comparative diagram showing velocity profiles obtained<br>by UVP-Monitor and current meter. ....            | 82 |
| Figure 5-5: Comparative color plot showing apparent movement of<br>artifacts (A) for different maximum depths.....      | 83 |
| Figure 5-6: Experimental setup for surface level measurements (left) and Fafnir probe (right).....                      | 84 |

|   |    |
|---|----|
| Figure 5-7: Color plot of surface level measurement completed<br>at an angle of 90° to the surface (4 MHz). ..... | 86 |
| Figure 5-8: Comparative diagram showing above measurement and<br>surface level obtained by Fafnir probe. ....     | 86 |
| Figure 5-9: Color plot of surface level measurement completed<br>at an angle of 75° to the surface (4 MHz). ....  | 87 |
| Figure 5-10: Comparative diagram showing above measurement and<br>surface level obtained by Fafnir probe. ....    | 87 |
| Figure 5-11: Color plot of surface level measurement completed<br>at an angle of 60° to the surface (4 MHz). .... | 88 |
| Figure 5-12: Comparative diagram showing above measurement and<br>surface level obtained by Fafnir probe. ....    | 88 |
| Figure 5-13: Color plot of surface level measurement completed<br>at an angle of 90° to the surface (2 MHz). .... | 89 |



---

## List of Tables

---

|   |    |
|---|----|
| Table 2-1: Values for the wavelength of ultrasound in steel, water and air, depending on frequency....                    | 6  |
| Table 2-2: Sound velocity and acoustic impedance of selected materials.....   | 9  |
| Table 2-3: Typical values for ultrasonic attenuation coefficients. ....   | 14 |
| Table 2-4: Critical angles of incidence for common pairs of materials. ....   | 18 |
| Table 2-5: Electroacoustical properties of assorted piezoelectric materials.....  | 20 |
| Table 2-6: Sound field properties in 20°C water as a function of<br>transducer diameter and operating frequency. ....     | 30 |
| Table 3-1: Spatial resolution, i.e., channel width, as a function of<br>cycles per pulse and operating frequency. ....    | 48 |
| Table 4-1: Cross-sectional dimensions of the Plexiglas test pipes.....  | 56 |
| Table 4-2: Expected flow rates and average velocities<br>in the inverted siphon pipes for tested discharges.....          | 57 |
| Table 4-3: Software parameters as applied to the pipe flow experiments<br>with UVP-XW 1.0 program.....                    | 61 |
| Table 4-4: Measurable velocity and resolution (temporal, spatial, velocity)<br>for the pipe flow experiments.....         | 62 |
| Table 4-5: Effect of limited spatial resolution on the determination of<br>the transmission angle for pipe 1.....         | 64 |
| Table 4-6: Relative errors in the flow rate computation at section m<br>showing poor agreement for pipe 2 and 3. ....     | 76 |
| Table 5-1: Software parameters as applied to the free-surface flow experiments<br>with UVP-XW 2.0 program. ....           | 81 |
| Table 5-2: Measurable velocity and resolution (temporal, spatial, velocity)<br>for the free-surface flow experiments..... | 82 |

|   |    |
|---|----|
| Table 5-3: Software parameters as applied to the surface level measurements<br>with the UVP-MFX 2.0 program. .... | 85 |
| Table 5-4: Spatial and temporal resolution of surface level measurements. ....                                    | 85 |

---

# 1 Introduction

---

Due to their complexity, many problems in the field of hydraulics still defy complete theoretical analysis, even with modern computing facilities. A combination of past experience, theory and dimensional analysis will provide partial or complete solutions to a number of problems. However, there still remain many problems that are tractable only through experimentation, for example the design of complex hydraulic structures. A qualified researcher is able to use the results from experiments to predict conditions on a full-scale prototype. Furthermore, model tests are essential to validate the results of numerical simulations.

Hydraulic testing at the Graz University of Technology started as early as the turn of the century and is closely associated with Philipp Forchheimer and Armin Schoklitsch. In 1964 on the initiative of Hermann Grengg, a modern laboratory was built, which now bears his name. Since 1998, Prof. Roman Klasinc has taken on the leadership of the laboratory. Today, the laboratory staff provides hydraulic analysis and testing through physical modeling, computer modeling, field investigations, and analytical studies. More than 300 model tests have been carried out for projects throughout Austria and abroad, as well as for basic research purposes.



*Figure 1-1: Main testing floor at the Hermann-Grengg Laboratories Graz.*

The facilities at the Hermann-Grengg Laboratories include an indoor testing hall with about 1,100 m<sup>2</sup> floor space for scale models, a 70 m<sup>3</sup> overhead reservoir, and supporting mechanical and electrical workshops. A pump station with a capacity of 1000 l/s supplies the testing floor through an automated flow delivery and measurement system.

---

## **1.1 Thesis Motive**

---

In model testing, measurements of various quantities such as pressure, velocity and viscosity are an essential part of analysis and operational control. For the measurement of velocity, a multitude of methods and devices has been developed over the years. The ultrasound-pulse-Doppler technique for velocity profile measurements represents a modern measurement method that is able to obtain complete velocity profiles as a function of time. A device providing this measurement technique, the UVP-Monitor, was recently acquired by the Hermann-Grengg Laboratories Graz. The author was one of the first who was given the opportunity to gain practical experience with this instrument. He then decided to study the measurement technique in more detail to provide a helpful guidance for other users of the ultrasound-pulse-Doppler method in the field of experimental hydraulics.

---

## **1.2 Research Objectives**

---

The main purpose of this thesis is to summarize the principles of ultrasonic velocity profile measurements. Included in this thesis are results from laboratory experiments investigating flow through pipes and free-surface flow. Particular emphasis in this research has been placed on the authentic understanding and clear presentation of the measurement technique. Additionally, the thesis should promote the exchange of information and experience with researchers and scientists in hydraulic laboratories and other relevant fields where ultrasonic velocity profile measurements may be conducted.

---

## **1.3 Tasks Completed**

---

All parts of this thesis were completed at the Hermann-Grengg Laboratories Graz. The author attained practical experience with ultrasonic velocity profile measurements while investigating the inverted siphon model. Over time, familiarity was gained with the UVP-Monitor, a device for ultrasonic velocity profiling. After the experimental phase of the thesis was finished, the author studied papers, articles and books concerning this specific measurement method and ultrasound in general. Additional information for this thesis was found in the Internet. The information from the literature and the experimental results were then compiled and presented in this thesis with conclusions and recommendations given by the author.

---

## 1.4 Thesis Contents

---

The thesis is divided into the following chapters:

The **first** chapter presents a brief introduction to experimental hydraulics and reviews the history of the Hermann-Grengg Laboratories Graz. It describes the importance of model tests in general and, particularly, of velocity measurement. The research objectives of the thesis and a description of the tasks completed are also included in this chapter.

The **second** chapter explains the basic physical principles of ultrasound. After defining the term *ultrasound*, the chapter describes the propagation and generation of ultrasonic waves. Acoustic properties of selected materials frequently used in test models are given as well. The chapter also covers the design of ultrasonic transducers and gives a description of the ultrasonic field in front of a transducer.

The **third** chapter takes a deeper look at the technique behind ultrasonic velocity profile measurements. The principles of the ultrasound-pulse-Doppler method are explained in more detail. A description of the key measurement parameters and their influence on spatial, temporal and velocity resolution is given. The chapter ends with a brief portrayal of the UVP-Monitor, a representative device for ultrasonic velocity profile measurements.

The next two chapters present the results of employing ultrasonic velocity profile measurements at the Hermann-Grengg Laboratories. While the **fourth** chapter describes the application of ultrasonic velocity profile measurements to the study of pipe flow, the **fifth** chapter examines the potential for measurement of both flow velocity and surface level in open channel flow. The setup and the respective measurement parameters are explained in detail. A brief summary of the experiments conducted is given at the end of each chapter.

The **sixth** chapter contains conclusions derived from the results of the experimental research and presents further recommendations concerning future measurements with the ultrasound-pulse-Doppler method.

The **seventh** and last chapter lists the literature sources that were used for this thesis, with links to the Worldwide Web.



---

## 2 General Properties of Ultrasound

---

Any acoustic wave above the normal range of human hearing, i.e., above 20,000 Hertz, is called *ultrasound*. In practice, the term usually refers to much higher frequencies used for applications, such as 4,000,000 Hertz for ultrasonic velocity profile measurements. Sound waves behave in many ways as light waves do, and optical analogies are frequently useful in describing acoustical phenomena. Thus, sound waves can be reflected, refracted, diffracted, and scattered, and many of the differences in behavior between sound and light waves simply reflect the very great difference in wavelengths.

This chapter will review the basic physical principles, which are most relevant for ultrasound applications in fluid engineering. Characteristic values for selected materials frequently used in experimental hydraulics are given as well.

---

### 2.1 Ultrasonic Waves

---

Sound waves are mechanical vibrations that propagate in a host medium. Solids support the propagation of both longitudinal waves (particles oscillating parallel to the direction of wave propagation) and transverse waves (particles oscillating perpendicular to the direction of wave propagation). Fluids (gases and liquids) only support longitudinal wave propagation. In addition, some ultrasonic waves propagate along the surface of a solid (Rayleigh waves) or in thin rods and sections of the material (Lamb waves).

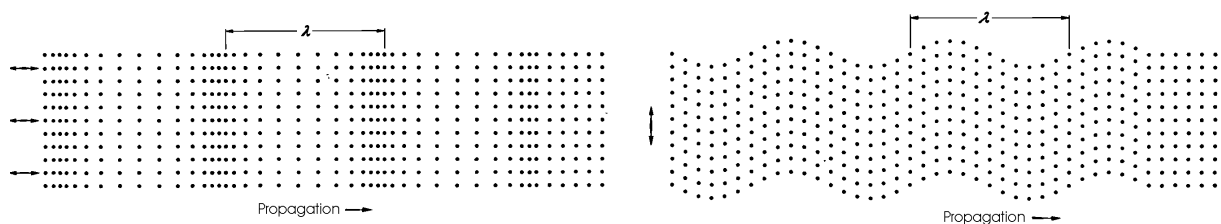


*Figure 2-1: Propagation of sound. Longitudinal waves (left) and transverse waves (right). [14]*

Longitudinal waves are also known as pressure waves, because they advance by alternate compression and rarefaction of a medium, causing particles in their path to move forward and backward along the direction of the wave's advance. For the application of ultrasound in experimental hydraulics, it is sufficient to concentrate only on this type of wave.

Sound waves are incapable of traveling through a vacuum, in contrast to electromagnetic waves, for example light waves.

Propagating waves obey the standard relation

$$c = \lambda f \tag{2.1}$$

where

|           |                                       |
|-----------|---------------------------------------|
| $c$       | acoustic velocity in the medium [m/s] |
| $f$       | frequency of the wave [Hz]            |
| $\lambda$ | acoustic wavelength [m]               |

The acoustic velocity changes with frequency, which is referred to as *dispersion*.

For the purpose of ultrasonic velocity profile measurements, the transmitting frequency usually ranges from 0.5 to 8 megahertz. Table 2-1 illustrates the corresponding wavelength in air, water and steel (longitudinal waves only).

| Frequency [MHz] | Wavelength $\lambda$ [mm]   |                             |                         |
|-----------------|-----------------------------|-----------------------------|-------------------------|
|                 | Steel<br>( $c = 5,900$ m/s) | Water<br>( $c = 1,480$ m/s) | Air<br>( $c = 330$ m/s) |
| 0.5             | 11.8                        | 2.96                        | 0.66                    |
| 1               | 5.90                        | 1.48                        | 0.33                    |
| 2               | 2.95                        | 0.74                        | 0.17                    |
| 4               | 1.48                        | 0.37                        | 0.08                    |
| 8               | 0.74                        | 0.19                        | 0.04                    |

Table 2-1: Values for the wavelength of ultrasound in steel, water and air, depending on frequency.

---

## 2.2 Acoustic Velocity

---

The velocity of sound in different media depends on a variety of factors such as density, temperature and other properties of the medium. In solids, the velocity also depends on the type of wave. In general, the speed of sound is given by:

$$c = \sqrt{\frac{E}{\rho}} \tag{2.2}$$

where

|        |  |
|--------|--|
| $c$    | sound velocity [m/s]                   |
| $E$    | elasticity modulus [N/m <sup>2</sup> ] |
| $\rho$ | density [kg/m <sup>3</sup> ]           |



Of particular interest for ultrasonic velocity profile measurements is the speed of sound in water. For liquids, the above equation becomes

$$c = \sqrt{\frac{B}{\rho_0}} \quad (2.3)$$

where  $B$                       adiabatic bulk modulus [N/m<sup>2</sup>]  
 $\rho_0$                       equilibrium density [kg/m<sup>3</sup>]

Usually, the speed of sound is given for a specific temperature, because the bulk modulus and equilibrium density vary with temperature.

The adiabatic bulk modulus  $B$  measures the resistance of fluids to a change in their volume at a constant temperature. Hence, the bulk modulus characterizes the stiffness of the medium. It is defined as the ratio of the pressure change to the volume strain:

$$B = -\frac{dP}{dV/V} \quad (2.4)$$

where  $P$                       pressure [N/m<sup>2</sup>]  
 $V$                       volume [m<sup>3</sup>]

The negative sign indicates that the volume decreases with increasing pressure. In solids, longitudinal waves travel faster than transverse waves because the bulk modulus for solids is generally greater than the shear modulus. Like the bulk modulus, the shear modulus measures the stiffness of a material not in response to compressions but rather in response to shearing.

In almost all liquids the acoustic velocity decreases with rising temperature. Water behaves in a different manner with increasing velocity as the temperature is lowered. Lubbers and Graaff published a simple formula for the calculation of sound velocity in pure water [17]:

$$c = 1405.03 + 4.624 T - 0.0383 T^2 \quad (2.5)$$

where  $c$                       speed of sound in pure water [m/s]  
 $T$                       temperature [°C]

The equation is valid only for temperatures from 10°C to 40°C at atmospheric pressure. Within the quoted temperature ranges the authors claim that the maximum error is approximately 0.18 m/s in comparison with experimental data and equations that are more detailed.

Values calculated with Lubbers and Graaff's equation can be found in Figure 2-2 below.

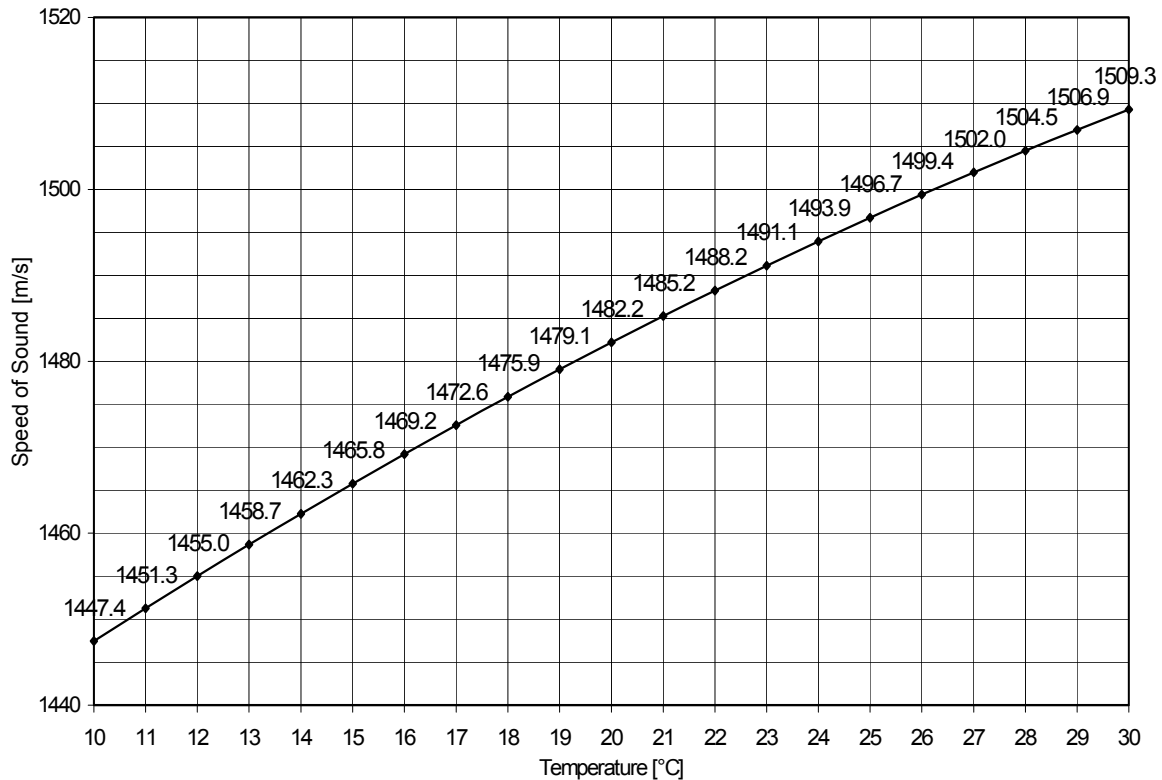


Figure 2-2: Speed of sound versus temperature in pure water.

The sound velocity in other substances is given in Table 2-2.

---

## 2.3 Acoustic Impedance

---

The acoustic impedance  $Z$  of a material is defined as the product of the density and acoustic velocity of that material. :

$$Z = \rho c \quad (2.6)$$

|       |        |   |
|-------|--------|---|
| where | $Z$    | acoustic impedance [kg/(m <sup>2</sup> s)] = [Ray]  |
|       | $\rho$ | density of transmitting medium [kg/m <sup>3</sup> ] |
|       | $c$    | sound velocity [m/s]                                |

The unit of acoustic impedance is called the *Rayleigh*, or *Ray*, named after John William Strutt, third Baron Rayleigh, 1842-1919, English physicist. A more practical unit is the *MRay*, which equals 1,000,000 Ray.

Values for the sound velocity and acoustic impedance of selected materials are given in Table 2-2. The numbers should be used with some caution. Many materials can differ in sound speed due to different production processes or ageing.

| <b>Medium</b>                                | <b>Density<br/>[10<sup>3</sup> kg/m<sup>3</sup>]</b> | <b>Sound<br/>Velocity<br/>[10<sup>3</sup> m/s]</b> | <b>Acoustic<br/>Impedance<br/>[MRay]</b> |
|--|--|--|--|
| <b>Liquids</b>                               |  |  |  |
| Water (20°C)                                 | 0.998  | 1.482  | 1.48                                     |
| Glycerine                                    | 1.26   | 1.92   | 2.42                                     |
| Mercury                                      | 13.6   | 1.45   | 19.7                                     |
| Diesel oil                                   | 0.80   | 1.25   | 1.00                                     |
| Mineral oil (SAE 30)                         | 0.87   | 1.74   | 1.51                                     |
| <b>Metals</b>                                |  |  |  |
| Aluminum                                     | 2.7  | 6.32   | 17                                       |
| Brass  | 8.4  | 4.40   | 37                                       |
| Copper                                       | 8.9  | 4.70   | 42                                       |
| Gold   | 19.3   | 3.24   | 63                                       |
| Iron (Cast)                                  | 6.9 - 7.3  | 3.5 - 5.8  | 24 - 42                                  |
| Iron (Steel)                                 | 7.7  | 5.90   | 45                                       |
| Lead   | 11.4   | 2.16   | 25                                       |
| Platinum                                     | 21.4   | 3.96   | 85                                       |
| Silver                                       | 10.5   | 3.60   | 38                                       |
| Tin  | 7.3  | 3.32   | 24                                       |
| Tungsten                                     | 19.1   | 5.46   | 104                                      |
| Zinc   | 7.1  | 4.17   | 30                                       |
| <b>Plastics</b>                              |  |  |  |
| Plexiglas™                                   | 1.19   | 2.73   | 3.25                                     |
| Teflon™                                      | 2.20   | 1.35   | 3.00                                     |
| Epoxy resins                                 | 1.10 - 1.25  | 2.4 - 2.9  | 2.6 - 3.6                                |
| Polyamide                                    | 1.1 - 1.2  | 2.2 - 2.6  | 2.4 - 3.1                                |
| Polycarbonate                                | 1.18 - 1.22  | 2.26 - 2.30  | 2.69 - 2.77                              |
| Polyethylene                                 | 0.90 - 0.96  | 1.95 - 2.43  | 1.73 - 2.33                              |
| Polypropylene                                | 0.88 - 0.90  | 2.66 - 2.74  | 2.36 - 2.40                              |
| Polystyrene                                  | 1.02 - 1.06  | 2.32 - 2.45  | 2.42 - 2.52                              |
| Polyvinylchloride                            | 1.16 - 1.47  | 2.38 - 2.40  | 3.27 - 3.35                              |
| <b>Other</b>                                 |  |  |  |
| Air (20°C)                                   | 0.0012   | 0.343  | 0.0004                                   |
| Coupling gel, Dahlhausen<br>(water-based)    | 1.004  | 1.48   | 1.48                                     |
| Coupling gel, Sonotrack<br>(glycerine-based) | 1.04   | 1.62   | 1.68                                     |
| Glass (Quartz)                               | 2.6  | 5.57   | 14.5                                     |
| Glass (Crown)                                | 2.4  | 5.10   | 12.2                                     |
| Ice  | 0.92   | 3.20   | 2.94                                     |

Table 2-2: Sound velocity and acoustic impedance of selected materials. [14][16][19][22][23]

Acoustic impedance is important in i) the determination of acoustic transmission and reflection at the boundary of two materials having different acoustic impedances, ii) the design of ultrasonic transducers, and iii) the assessment of sound absorption in a medium.

---

## 2.4 Scattering

---

Ultrasonic waves propagate through uniform media undisturbed. Scattering and reflection can occur, however, if there are any variations in the medium. Although the two phenomena are closely related, scattering refers to the interaction between sound waves and particles that are much smaller than the sound's wavelength, while reflection refers to interaction with particles or objects larger than the wavelength.

In general, ultrasound waves scatter at regions with different compressibility and/or density, i.e. gas bubbles or dirt particles in water. These point reflectors produce low-amplitude, omnidirectional scattering, also known as *diffuse scattering*, while large flat boundaries produce high-amplitude, directionally dependent echoes, known as *specular reflection*. Interfaces that have a rough surface produce a diffuse component of scattering along with specular reflection, as Figure 2-3 illustrates. This diffuse scattering component plays an important role for surface level measurements, which will be described in Chapter 5.

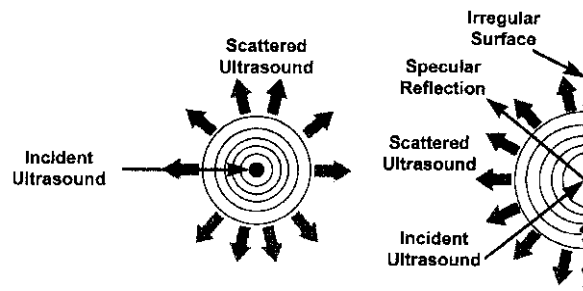


Figure 2-3: Scattering. Point reflector (left) and rough interface (right). [7]

Pulse-echo applications like velocity profile measurements completely rely on the fact that the test medium scatters or reflects incident ultrasound waves. In water, the natural particle contamination usually generates enough significant echo signals. If not, particles have to be added in a process called *seeding*. It is important to keep in mind that ultrasonic velocity profile measurements do not measure the velocity of the fluid itself, but the velocity of particles traveling in the fluid. Particles with the same density as the fluid will travel with a velocity close to that of the fluid itself and are, thus, the most accurate seeding particles. Unfortunately, ultrasound does not scatter at regions with the same density. Most important, however, is the size of the scatterer, because the amount of energy reflected by the scatterer and its angular distribution primarily depend on the ratio of particle size to ultrasonic wavelength.

Particles, whose dimensions are very small compared to ultrasonic wavelength (less than about one-tenth), undergo *Rayleigh* scattering. If this particle is of the same density as the medium but its compressibility is different, it will react to the surrounding pressure variation by radially expanding and contracting, thus emitting monopole radiation, as shown in Figure 2-4a. If these conditions are reversed, i.e. the particle's compressibility is the same as the surrounding medium but its density is different, the particle's motion in response to the incident wave will not equal that of the medium, and it will move back and forth in relation to the medium. This type of scatterer emits dipole radiation, as shown in Figure 2-4b. Most real sub-wavelength scatterers emit a combination of monopole and dipole radiation, as illustrated in Figure 2-4c. With the source of ultrasound at zero degrees, the illustration shows that Rayleigh scatterers reflect more energy back towards the source than away from the source.

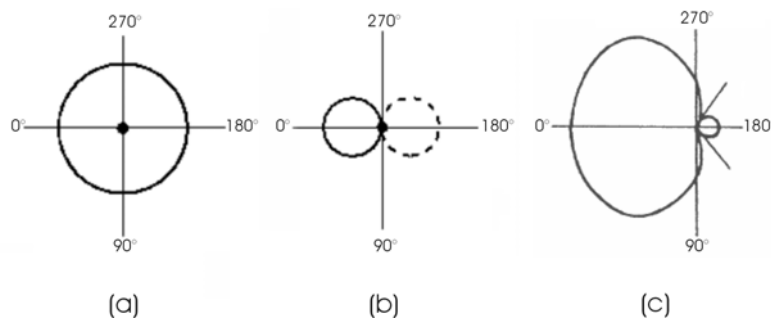


Figure 2-4: Monopole (a) and dipole (b) radiation together compose Rayleigh scattering (c). [2][25]

When the particle size approaches the wavelength of the incident ultrasound, the scattering varies in a more complex fashion described by the *Mie* theory (Gustav Mie, 1868-1957, German physicist). In the case of scattering by a spherical object, the scattering intensity and its angular distribution can be calculated precisely [5]. Again, the radiation pattern depends on the density and compressibility of the scatterer. The boundary of an elastic sphere may start to vibrate at a certain frequency, known as resonance scattering, while the surface of a rigid sphere stays at rest and no waves can propagate inside. Thus, the scattering pattern of gas bubbles (elastic) can be distinguished from dirt particles (rigid).

Figure 2-5 illustrates the radiation pattern of an elastic (dashed line) and a rigid particle (solid line) as a function of  $k \cdot a$ , the product of wavenumber  $k$  ( $k = 2\pi/\lambda = 2\pi f/c$ ) and the sphere's radius  $a$ . The source of ultrasound lies at  $180^\circ$ . Small spheres ( $k \cdot a \leq 1$ ) still undergo Rayleigh scattering. As the size of the sphere increases, the radiation pattern changes, and ultrasonic waves get scattered predominantly in the forward direction.

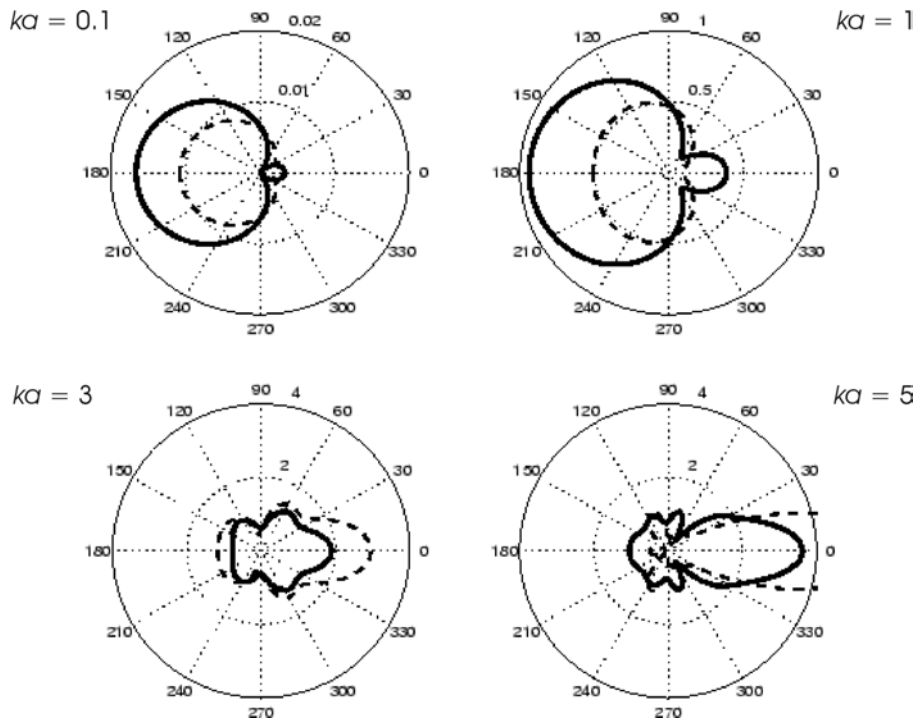


Figure 2-5: Mie scattering of a rigid (solid line) and an elastic (dashed) spherical scatterer. [2]

In Figure 2-6, we consider the backscatter amplitude of the spherical particle as a function of  $ka$ . Figure 2-6a shows that the echo amplitude of very small particles (solid line) is roughly identical to  $(ka)^2$  (dashed line). Hence we can expect the backscatter amplitude of Rayleigh scatterers to have a quadratic frequency dependence ( $k \propto f$ ). Figure 2-6b compares the echo amplitude of an elastic (dashed line) with a rigid (solid line) particle, showing how reverberation of sound within an elastic scatterer can create peaks and nulls in the scattering spectrum.

Theories of scattering by spherical objects suggest a minimum size for seeding particles. While the backscatter amplitude increases with particle size in the Rayleigh regime, the backscatter amplitude of larger scatterers oscillates about the theoretical maximum. Thus seeding particles that undergo Mie scattering are the best choice (The company Met-Flow suggests a diameter of  $d \geq \lambda/4$ ).

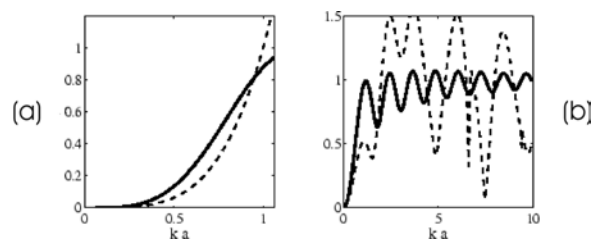


Figure 2-6: Backscatter amplitude of Rayleigh scatterers (a) and particles in the Mie regime (b). [2]

---

## 2.5 Attenuation

---

It is well known that sound energy decreases with distance traveled. In idealized materials, sound pressure (signal amplitude) is only reduced by the spreading of the wave. Natural materials, however, all produce an effect that further weakens the sound. This further weakening, or *attenuation*, results from two basic causes, scattering and absorption.

The motion of an acoustic wave is the result of two fundamental energy forms, the regainable potential energy of the volume compression and the kinetic energy, given by the particle velocity. The wave propagation is perpetuated by an exchange between these two forms of energy. Absorption is the conversion to other energy forms, like heat or chemical energy, meaning a loss of energy from the acoustic wave.

Ultrasonic attenuation is the decay rate of mechanical radiation at ultrasonic frequencies as it propagates through a material. Along the line of propagation, the attenuation is expressed by Beer's Law (Augustus Beer, 1825-1863, German physicist) as

$$p = p_0 e^{-\alpha d} \quad (2.7)$$

where  $p, p_0$  sound pressures at the start and end of a length  $d$  [ $\text{N/m}^2$ ]  
 $d$  distance along the line of propagation [m]  
 $\alpha$  coefficient of attenuation [Neper/m]

In the equation above, the unit of attenuation is Neper/length. Neper is a dimensionless unit like the radian for angles (John Napier, Latin *Neper*, 1550-1617, Scottish mathematician). However, the attenuation is more frequently expressed in the unit dB/length as

$$p = p_0 10^{\frac{-\alpha d}{20}} \quad (2.8)$$

where  $\alpha$  coefficient of attenuation [dB/m]

The attenuation coefficient is composed of two parts: absorption, which is proportional to the square of ultrasound frequency, and scattering, which depends on the ratio of particle size to ultrasound wavelength. In general, a single attenuation coefficient only applies to a single frequency. A quadratic frequency dependence applies to water and air because the effect of scattering is negligible [7].

Some typical values for ultrasonic attenuation coefficients are given in Table 2-3. Again, the numbers should be used with caution. A quadratic frequency dependence is indicated by ( $f^2$ ).

| Medium       | Attenuation [dB/m at 2 MHz] | Drop to 50% [m] |
|--------------|-----------------------------|-----------------|
| Water        | 0.8 ( $f^2$ )               | 7.53            |
| Metals       | < 10                        | > 0.60          |
| Plastics     | < 100                       | 0.60 - 0.06     |
| Rubber, Wood | > 100                       | < 0.06          |
| Air          | 4,800 ( $f^2$ )             | 0.001           |

Table 2-3: Typical values for ultrasonic attenuation coefficients. [1][14]

Of particular interest is the frequency dependence of ultrasonic attenuation in water, which is illustrated in Figure 2-7. For instance, after traveling less than 50 cm, 8-MHz ultrasonic waves will be attenuated 6 dB, which equals a reduction of acoustic pressure by 50 %. In contrast, 1-MHz ultrasonic waves only lose less than 2 % of acoustic pressure over the same distance. This mandates for applications in the field of experimental hydraulics, that the operating frequency has to be selected carefully according to the dimensions of the physical model. High-frequency ultrasound offers excellent spatial resolution because of its short wavelength and thus should be preferred over low frequencies when investigating small scale models.

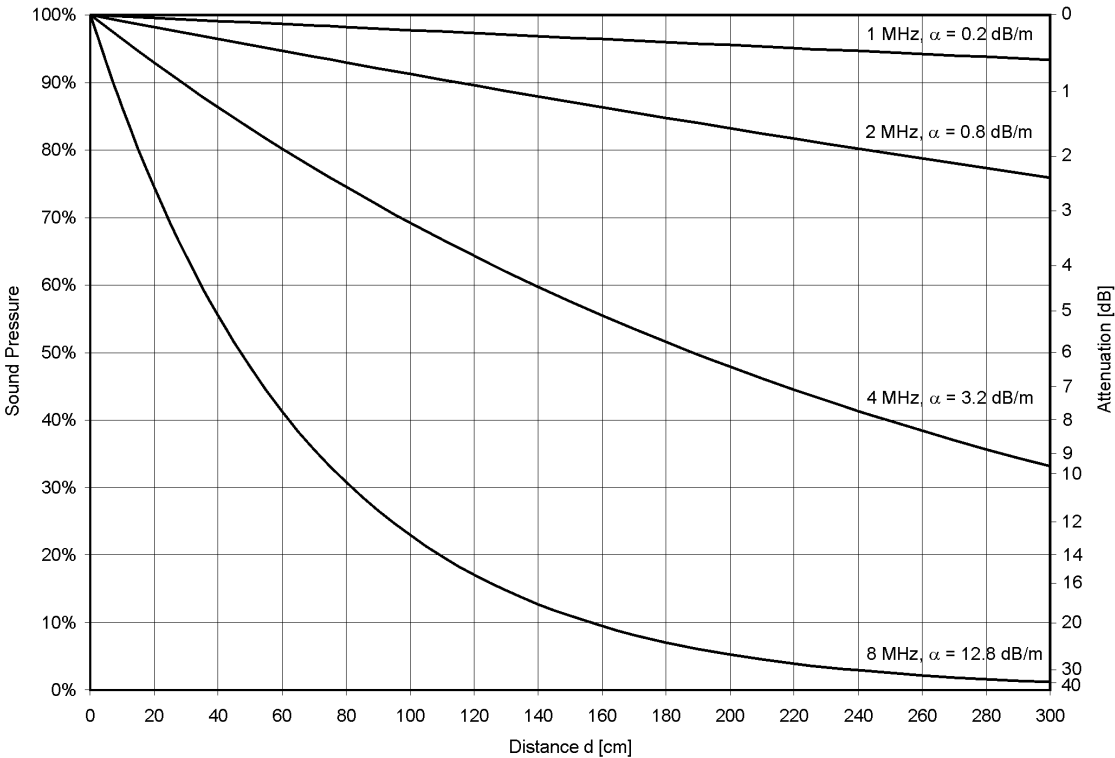


Figure 2-7: Attenuation of ultrasound for four different frequencies in water as a function of distance.



Another important material frequently used for scale models is Plexiglas. Plexiglas attenuation has an almost linear dependence to frequency, as illustrated in Figure 2-8. Over the frequency range of 0.5 to 5.5 MHz, the attenuation function is fitted by a straight line.

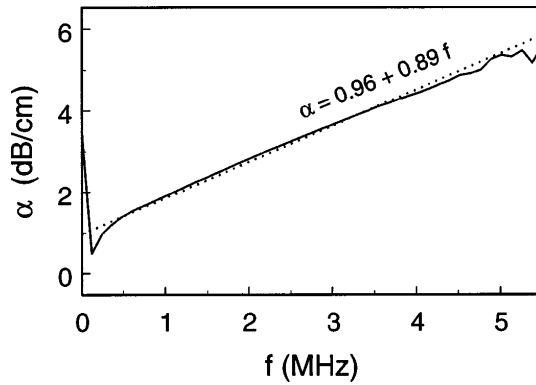


Figure 2-8: Attenuation function of Plexiglas. [9]

The frequency dependence of attenuation does affect short ultrasonic pulses, which have a large frequency bandwidth. As the pulse propagates through the medium, the higher frequencies in its bandwidth are attenuated more severely than the lower frequencies. Dispersion causes additional change in the waveform of the propagating pulse because wave components with different frequencies travel with different speed. This means that echoes from far reflectors have longer pulse lengths and lower center frequencies than do echoes from near structures. Figure 2-9 illustrates how the waveform of a sample pulse changed after traveling through an 8-cm thick Plexiglas block.

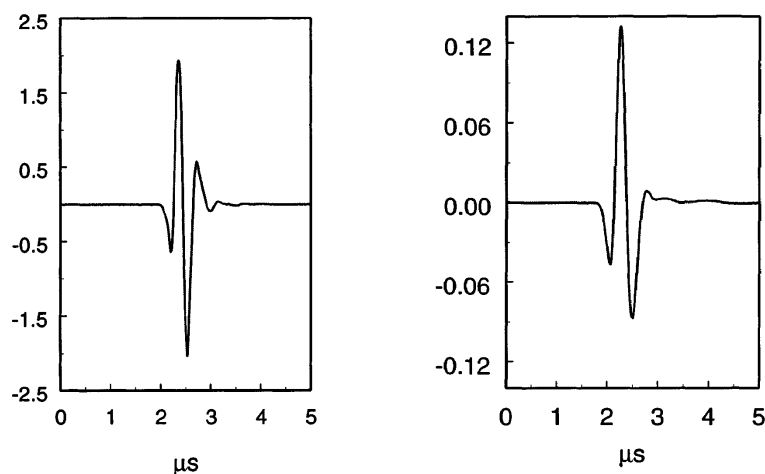


Figure 2-9: Change of pulse waveform due to attenuation and dispersion; transmitted pulse (left), received pulse (right). [9]

---

## 2.6 Reflection and Refraction

---

When an ultrasonic wave strikes an interface between two media having different acoustic impedances, some of the wave reflects while some is transmitted to the second medium, as Figure 2-10 depicts. The behavior of a wave at that boundary depends on the angle of incidence and the ratio of the speeds of sound in the two media.

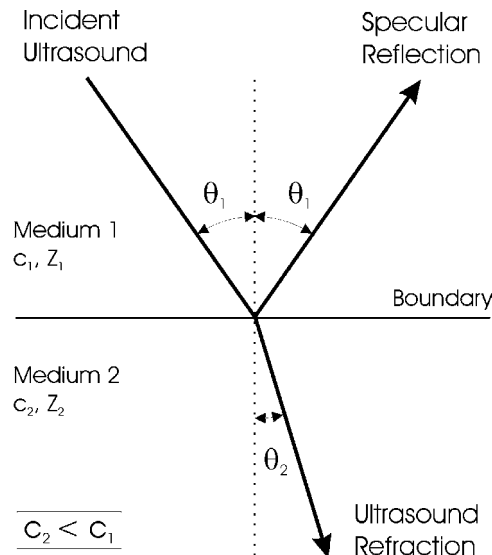


Figure 2-10: Reflection and refraction of ultrasound on interface.

The law of reflection requires that the angle of reflection be equal to the angle of incidence. If measurement is performed with a single transducer, specular reflections are only received by the transducer if the ultrasound beam is normal to the interface (or close to normal).

Refraction of ultrasound waves obey Snell's Law, which relates the angles of incidence and transmission to the acoustic velocities in the two media (Willebrord van Roijen Snell, 1580-1626, Dutch astronomer and mathematician):

$$\frac{c_1}{c_2} = \frac{\sin \theta_1}{\sin \theta_2} \quad (2.9)$$

where  $c_1, c_2$  speed of sound in medium 1 and medium 2  
 $\theta_1, \theta_2$  incident and refraction angle to normal

When the ultrasonic wave crosses an interface from a medium with higher speed of sound to a medium with lower speed of sound, the wave bends towards the normal, as shown in Figure

2-10. When the wave travels from a medium with higher speed of sound to a medium with lower speed of sound, the wave bends away from the normal. This has an interesting implication: at some angle, known as the *critical angle*, sound waves will be refracted at a right angle; in other words, refracted along the interface, as depicted in Figure 2-11.

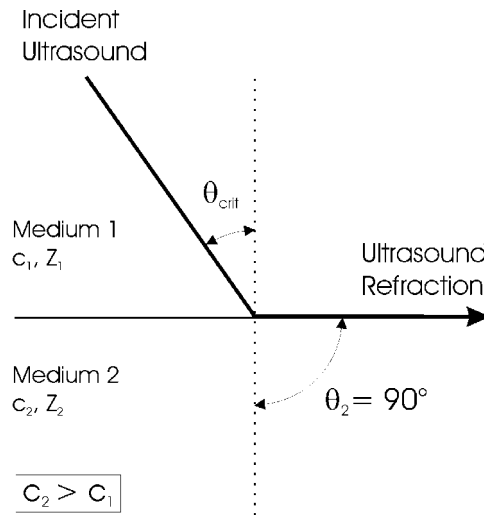


Figure 2-11: Critical angle of incidence.

In contrast to optical waves, when an ultrasonic wave encounters a boundary, one type of wave can be transformed into another, for example, longitudinal waves into transverse waves and vice versa. At the critical angle of incidence, much of the acoustic energy is mode converted to a Rayleigh wave. Mode conversion is important for certain ultrasonic testing (UT) methods, wherein an angle beam transducer introduces refracted transverse waves into a solid test material to detect flaws in and around welded areas.

The critical angle of incidence can be found from Snell's Law by putting in an angle of  $90^\circ$  for the angle of the refracted ray.

$$\theta_{crit} = \sin^{-1}\left(\frac{c_1}{c_2}\right) \quad (2.10)$$

If the incident wave hits the interface at any angle larger than the critical angle, it will not pass through to the second medium at all. This effect has major consequences for non-invasive velocity profile measurements, which are limited to angles below the critical angle. If the critical angle is very small, e.g., for a combination of water-based coupling gel and aluminum, it can be more helpful to bring the transducer into direct contact with the fluid.

Table 2-4 illustrates the critical angles for common material combinations.

| Material 1                                     | Material 2     | $c_1$<br>[m/s] | $c_2$<br>[m/s] | $\theta_{crit}$<br>[deg] |
|--|----------------|----------------|----------------|--------------------------|
| Water (20°C),<br>Coupling gel<br>(water-based) | Plexiglas™     | 1,482          | 2,730          | 33                       |
|  | Other plastics |                | 1,950 - 2,900  | 50 - 31                  |
|  | Lead           |                | 2,160          | 43                       |
|  | Tin            |                | 3,320          | 27                       |
|  | Glass (Quartz) |                | 5,570          | 15                       |
|  | Iron (Steel)   |                | 5,900          | 15                       |

Table 2-4: Critical angles of incidence for common pairs of materials.

The acoustic pressure of the reflected and transmitted wave can be derived because the particle velocity and local particle pressures are required to be continuous across the boundary:

$$p_i + p_r = p_t \quad (2.11)$$

$p_i, p_r$  sound pressure of incident and reflected wave [N/m<sup>2</sup>]  
 $p_t$  sound pressure of transmitted wave [N/m<sup>2</sup>]

The reflection coefficient R is defined as the ratio of the reflected sound pressure to the incident sound pressure:

$$R = \frac{p_r}{p_i} = \frac{Z_2 \cos \theta_1 - Z_1 \cos \theta_2}{Z_2 \cos \theta_1 + Z_1 \cos \theta_2} \quad (2.12)$$

where  $Z_1, Z_2$  acoustic impedance of media [Ray]  
 $\theta_1, \theta_2$  incident and reflection angle to normal

Similarly, we define the transmission coefficient T as the ratio of the transmitted sound pressure to the incident sound pressure:

$$T = \frac{p_t}{p_i} = 1 + R = \frac{2Z_2 \cos \theta_1}{Z_2 \cos \theta_1 + Z_1 \cos \theta_2} \quad (2.13)$$

If  $Z_1$  equals  $Z_2$ , the reflection coefficient is zero and only transmission occurs at the interface; this condition is called *impedance matching*. The larger the difference between  $Z_1$  and  $Z_2$ , the larger the reflection coefficient; this condition is called *impedance mismatching*. If  $Z_1 < Z_2$ , the reflected wave has no phase change upon reflection but if  $Z_1 > Z_2$ , the reflected wave undergoes a 180° phase change. Both cases are depicted in Figure 2-12.

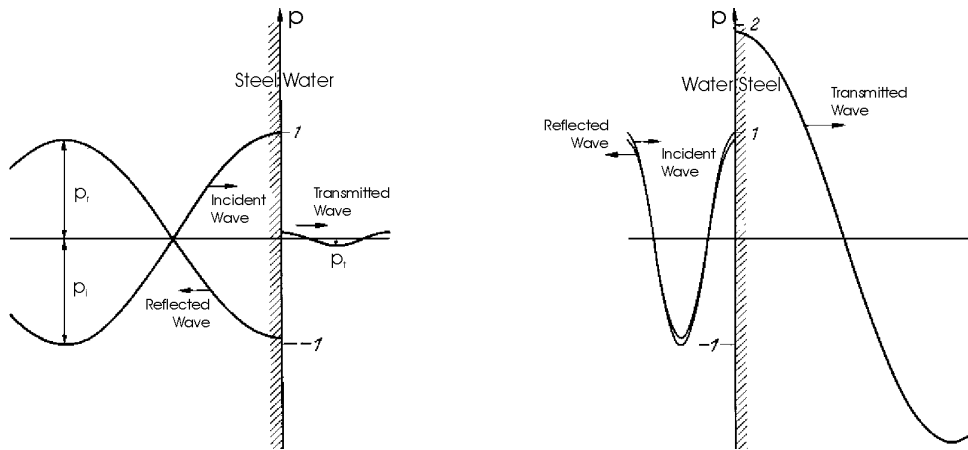


Figure 2-12: Acoustic pressure at the boundary of steel and water for normal incidence. [14]

Whenever an ultrasonic wave encounters an interface, part of the acoustic energy is lost due to reflection. The pressure loss increases with the angle of incidence and the mismatch of acoustic impedances. Hence, some wall materials are less suitable for non-invasive measurements because of their low transmission coefficient. Figure 2-13 illustrates the reduction of sound pressure for several wall materials as a function of incident angle. Values are given for through-the-wall measurement at 20°C and the use of water base coupling gel. The additional loss of sound pressure due to ultrasonic attenuation in the wall layer is not included.

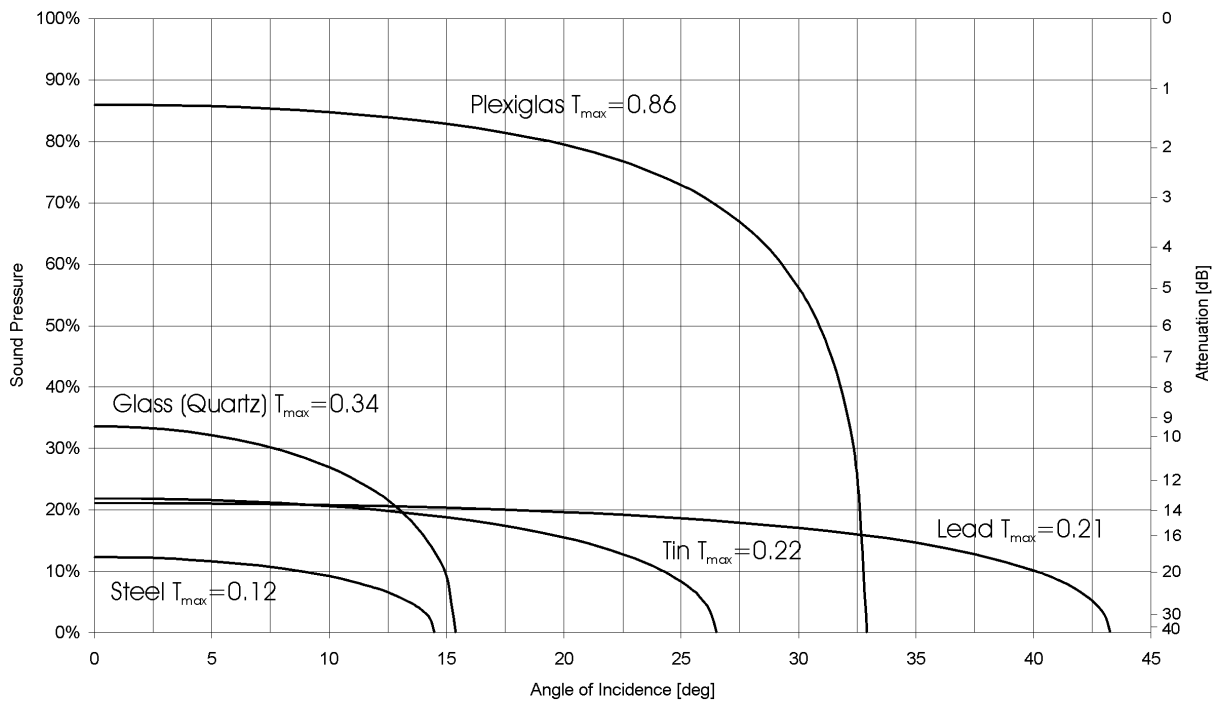


Figure 2-13: Transmission coefficients for several wall materials as a function of the angle of incidence.

---

## 2.7 Generation of Ultrasound

---

The generation and reception of ultrasonic waves is usually accomplished using the piezoelectric effect. Piezoelectricity was discovered by Pierre and Jacques Curie in 1880 and literally stands for “pressure electricity”. It is the phenomenon in which certain crystalline substances develop an electric field when subjected to pressure/forces, or conversely, exhibit a mechanical deformation when subjected to an electric field. This reciprocal coupling between mechanical and electrical energy makes piezoelectric materials useful in many applications.

The crystalline piezoelectric materials with the widest technical applications today are quartz ( $\text{SiO}_2$ ), as electromechanical oscillators to stabilize frequency in RF oscillators, and lithium niobate ( $\text{LiNbO}_3$ ) for SAW-devices (Surface Acoustic Waves). However, these materials are not efficient for the transmission of acoustic energy into water and biological materials. Medical applications of ultrasound first started after the ferroelectric material barium titanate ( $\text{BaTiO}_3$ ) was discovered in 1942-43. Ferroelectric materials are composed of a multitude of randomly orientated crystals that form local domains of polarization. The polarization of these domains can be permanently aligned to provide the material with piezoelectric properties. The piezoelectric effect increases, as more of the domains are aligned.

Ferroelectricity is found only in crystals that have no center of symmetry. Rochelle salt and lithium niobate have ferroelectric properties, but especially strong ferro- and piezoelectric properties are found in a few ceramics, such as certain titanates and zirconates. These materials have made it possible to generate ultrasound waves in the megahertz range, and have thus opened up the field of modern ultrasonics. Today, the ferroelectric ceramic composites of lead, zirconates, and titanates (PZT) have taken over from barium titanate.

The electroacoustical properties of different piezoelectric materials are given in Table 2-5.

| Material        | Density<br>[ $10^3 \text{ kg/m}^3$ ] | Sound<br>Velocity<br>[ $10^3 \text{ m/s}$ ] | Acoustic<br>Impedance<br>[MRay] | Coupling<br>Coefficient<br>[-] |
|-----------------|--------------------------------------|---|---------------------------------|--------------------------------|
| Barium Titanate | 5.30                                 | 5.20  | 27.6                            | 0.33                           |
| Lithium Niobate | 4.64                                 | 7.32  | 34.0                            | 0.47                           |
| Quartz          | 2.65                                 | 5.74  | 15.2                            | 0.10                           |
| PZT             | 7.7 - 7.8                            | 4.2 - 3.8                                   | 30 - 32                         | 0.45 - 0.50                    |
| 1-3 Composite   | 3.5 - 4.0                            | 2.2 - 3.0                                   | 8 - 12                          | 0.5 - 0.7                      |

Table 2-5: Electroacoustical properties of assorted piezoelectric materials. [8][14][15]

The coupling coefficient indicates to what extent a piezo-element converts electrical energy into mechanical energy, in other words, it represents its efficiency at generating ultrasound. The coupling coefficient of piezo-ceramics is basically high. However, if ultrasound is to be radiated into liquids or plastics, most part of the acoustic energy is reflected at the boundary because of the impedance mismatch and a high coupling coefficient becomes less important.

In the manufacture of piezoceramics, a suitable ferroelectric material is first fabricated into the desired shape and electrodes are applied. Next, the element is heated above its Curie temperature, above which a ferromagnetic material becomes paramagnetic and loses its permanent magnetism. The ceramic is then cooled slowly with a strong electric field applied between the electrode surfaces in a process called *poling*. This aligns the molecular dipoles of the ceramic in the direction of the applied field and provides the piezoelectric properties.

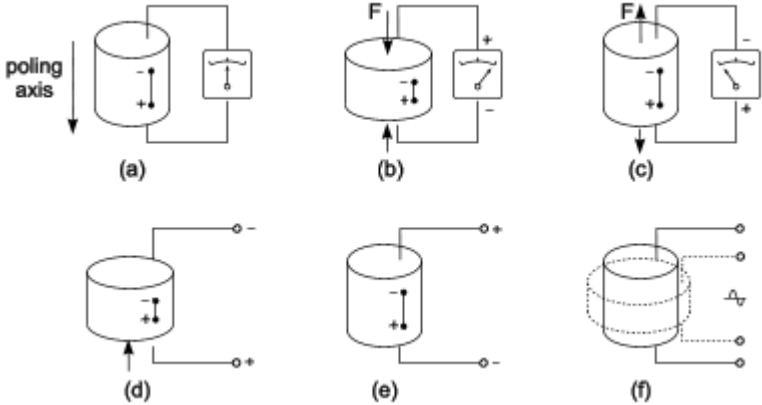


Figure 2-14: Direct (above) and converse (below) piezoelectric effect.

The figure above illustrates the piezoelectric effect. A cylinder has been polarized in the direction of the arrow. Figure 2-14a shows the cylinder under no-load conditions. If an external force produces compressive or tensile strain in the material, the resulting change in dipole moment causes a voltage to appear between the electrodes. If the cylinder is compressed, the voltage will have the same polarity as the poling voltage (Figure 2-14b). If it is stretched, the voltage between the electrodes will have polarity opposite to the poling voltage (Figure 2-14c). The conversion of mechanical energy into electrical energy is called the *direct piezoelectric effect*. The cylinder will shorten if a voltage of opposite polarity to the poling voltage is applied to the electrodes (Figure 2-14d). If the applied voltage has the same polarity as the poling voltage, the cylinder will lengthen (Figure 2-14e). Finally, if an alternating voltage is applied to the electrodes, the cylinder will alternate in size (Figure 2-14f).

The AC voltage generates two longitudinal ultrasonic waves that propagate from each electrode into the element. The two waves may reinforce each other as they reflect back and forth from the electrode surfaces, causing resonant thickness oscillations within the active element. These resonant oscillations occur at a frequency where the cylinder thickness equals half an acoustic wavelength or odd multiples of the frequency. At this particular frequency, the conversion from electric to acoustic energy (*converse piezoelectric effect*) is very efficient. In practice, the thickness of a piezoelectric element is adjusted to half of the wavelength of the transducer's default operating frequency ( $\lambda/2$  resonant mode or thickness mode).

To generate a narrow ultrasonic beam, a uniform and well-defined vibration of the piezoelectric element is necessary. In ultrasound-pulse-Doppler applications like velocity profile measurements, the transducer is usually driven by an electrical pulse with a wide frequency range so that resonant modes outside the  $\lambda/2$  mode can be excited and damage the ultrasound beam emitted by the transducer. Such modes are usually avoided by the *composite* piezoelectric material, where the piezoelectric plate is cut into small bars of less than  $\lambda/2$  in width, and the space between the bars is filled with epoxy so that a plate is obtained as illustrated in Figure 2-15. Such thin bars will have a single length mode of vibration at the operating frequency.

An additional advantage of the composite material is that the plate behaves as a single piezoelectric material with lower mechanical impedance. This helps in transmitting the energy into the test medium and reduces reflection of the returning echoes. Because the ceramic rods present a mechanical continuity following one dimension in space and the epoxy matrix presents a continuity in three dimensions, this material is also known as *1-3 piezo-composite*.

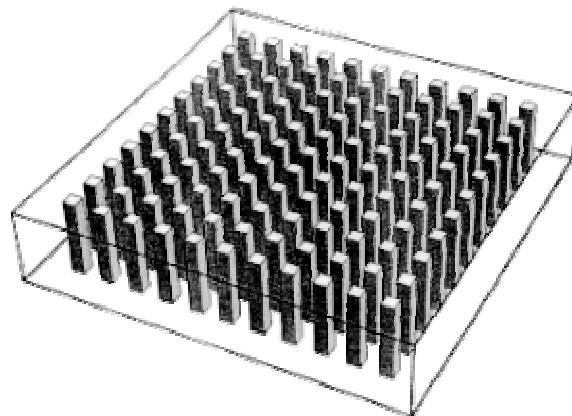


Figure 2-15: Schematic representation of a 1-3 piezo-composite plate. [8]



---

## 2.8 Transducer Design

---

The transducer is one of the most critical components of any ultrasonic system. The best choice for applications in the field of experimental hydraulics is the *immersion* transducer. It is specially designed to operate in liquids like water or coupling materials. The technique provides a means of uniform coupling and reduces sensitivity variations. Additionally, immersion transducers are more flexible to use due to their small size. *Contact* transducers, the other transducer type, are used mainly in the field of non-destructive testing (NDT). The contact technique provides a higher coupling efficiency since the acoustic impedance of the transducer and the test materials (usually metals) is almost the same.



Figure 2-16: Sample pictures of immersion transducers (left) and contact transducers (right). [21]

Figure 2-17 shows the elemental components of an ultrasonic transducer. The thin piezoelectric element is bonded to a backing material in the rear and a plastic wear surface in the front, which is then all fit into a housing. This general design applies to both types of transducers.

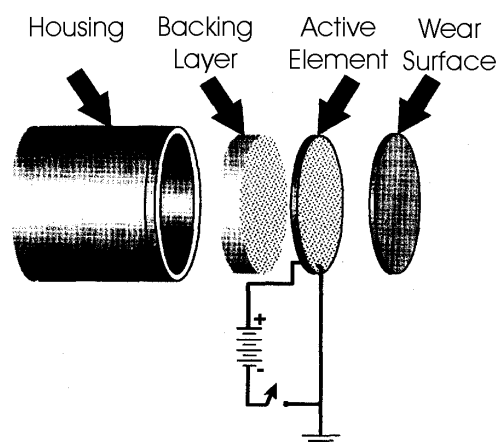


Figure 2-17: Main components of an ultrasonic transducer. [7]

Since the active element is operated in resonant mode, it will ring for quite a few oscillations after the voltage source is removed. This is called the *ring-down*. Figure 2-18a shows the acoustic pressure on the piezoelectric element when the transducer is driven with a very short electric pulse (impulse response), and illustrates the minimum length  $T_p$  of the ultrasound pulse that can typically be transmitted without additional damping. This is undesirably long for pulse-echo applications like velocity profile measurements where we want a short pulse for high spatial resolution. Both the backing and the wear surface can help to reduce the ringing of the active element. Their effect is illustrated in Figure 2-18b.

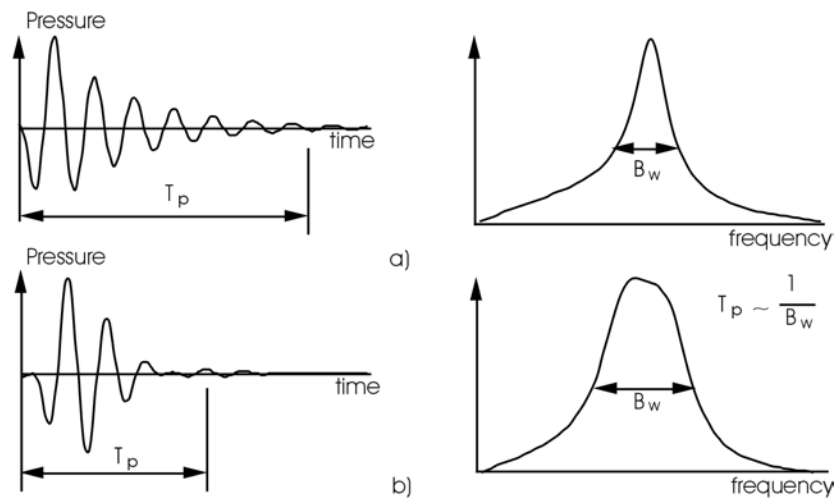


Figure 2-18: Shortest possible pulses obtained from a transducer a) without and b) with backing layer (left) and the Fourier transform of the pulses (right). [3]

The purpose of the backing layer is to absorb ultrasonic energy, causing the pulse length to be as short as possible. When the active element is mounted on a heavy, stiff and absorbing backing, the ringing is additionally dampened because energy is transmitted into the backing. Unfortunately, the impedance matching between active element (high impedance) and backing (high impedance) reduces the amplitude of the pulse transmitted into the test medium as well as the sensitivity of the transducer as a receiver.

Beyond its basic purpose of protecting the active element from mechanical damage, the wear surface serves as an acoustic impedance transformer. The wear plate (medium impedance) connects the active element (high impedance) with the propagation medium, in case of immersion transducers usually water or coupling gel (low impedance). When the wear plate is set in between, the energy transfer between the active element and the medium is more efficient, and the ringing of the active element dies out more quickly.

The wear plate's thickness is adjusted to a quarter of the acoustic wavelength, thus it is often referred to as a *quarter wave impedance transformer*. Quarter-wave matching allows waves generated by the active element to be in phase with the wave reverberating in the wear plate. When signals are in phase, their amplitudes are additive and consequently a greater amplitude wave enters the test medium. Figure 2-19 shows the active element and the wear plate when the waves are in phase.

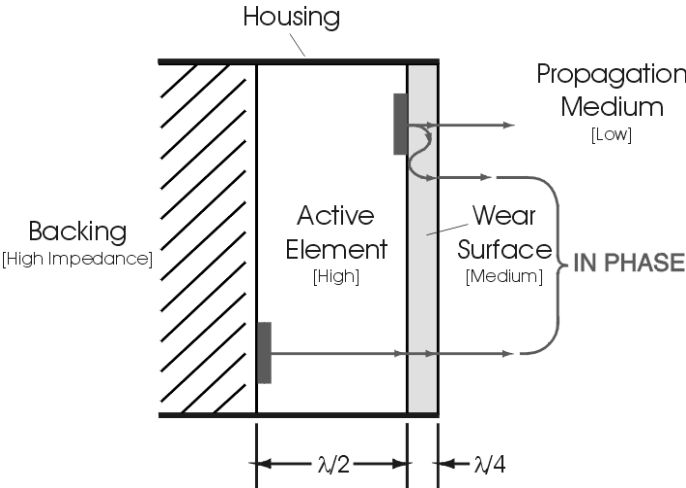


Figure 2-19: Layer structure of an immersion transducer. [21]

The Fourier transforms of the pulses (Figure 2-18, right) illustrate the distribution of frequencies in each pulse (Jean Baptiste Joseph Fourier, 1768-1830, French mathematician). The relationship between the pulse length and the bandwidth of frequencies is related to the Heisenberg uncertainty principle (Werner Heisenberg, 1901-1976, German physicist), which can be mathematically expressed as

$$\Delta t \cdot \Delta f \cong 1 \tag{2.14}$$

where  $\Delta t$  uncertainty in pulse arrival time, expressed by the pulse length  $T_p$   
 $\Delta f$  uncertainty of the pulse frequency, expressed by the bandwidth  $B_w$

Figure 2-18 displays how the bandwidth  $B_w$  is inversely proportional to the pulse length  $T_p$ : shorter ultrasonic pulses will have a larger frequency bandwidth. When a broadband pulse is traveling in the propagation medium, the waveform of the pulse changes because of attenuation and dispersion within the medium, as depicted earlier in Figure 2-9. A narrowband pulse is less affected by this interaction with the propagation medium, and the nearly unpredictable influence on the frequency spectrum is reduced.

The Heisenberg principle leads to an additional trade off for any pulsed Doppler system. These systems are based on the Doppler frequency shift and calculate the velocity of a traveling particle by detecting the change between the emitted pulse frequency and the reflected pulse frequency. The problem is that to localize the sample volume accurately in space, a short pulse is required. This corresponds to a wider transmitted bandwidth. Then, as Heisenberg predicts, the ability to measure the velocity accurately decreases. However, the accuracy of ultrasonic velocity measurement depends on many other parameters, and from a practical point of view, all of them have a lot more influence than the Heisenberg relationships.

---

## 2.9 Ultrasonic Sound Field

---

To analyze the sound field emitted by a transducer, we can use Huygens' principle where each point on the transducer surface acts as a source of a spherical wave (Christian Huygens, 1629-1695, Dutch mathematician and physicist). These partial waves will interfere and generate a resulting beam. Figure 2-20 shows a simplified illustration of an ultrasonic beam emitted by an unfocused, circular, single-element transducer operating in continuous mode.

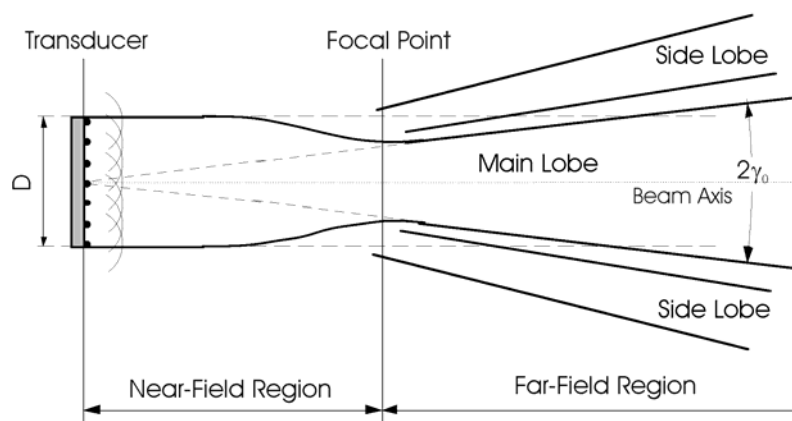


Figure 2-20: Schematic illustration of the formation of an ultrasonic beam. [3]

There are two regions: a cylindrical near-field region and a conical far-field region. In the far-field region, the beam expands with a fixed opening angle due to diffraction. The beam is composed of a central main lobe surrounded by smaller side lobes. In the near-field region, interference effects caused by rays emanating from different portions of the front surface cause spatial variations of sound pressure both axially and laterally. At the juncture of the two zones, the sound pressure has its last axial maximum, which represents its natural focal point.

The length of the near-field region is defined as the distance between the transducer surface and the natural focal point and can be estimated by:

$$N = \frac{D^2}{4\lambda} \quad (2.15)$$

where

|           |   |
|-----------|---|
| $N$       | length of near-field region [mm]                    |
| $D$       | diameter of active element, or <i>aperture</i> [mm] |
| $\lambda$ | ultrasonic wavelength in test medium [mm]           |

The beam amplitude in the in the near-field region depends on the operating mode of the ultrasonic transducer. For continuous wave (CW) excitation, the sound pressure along the axis goes through a series of maxima and minima as illustrated in Figure 2-21a, while with a short-pulse wave (PW) excitation, the pressure oscillations disappear as shown in Figure 2-21d.

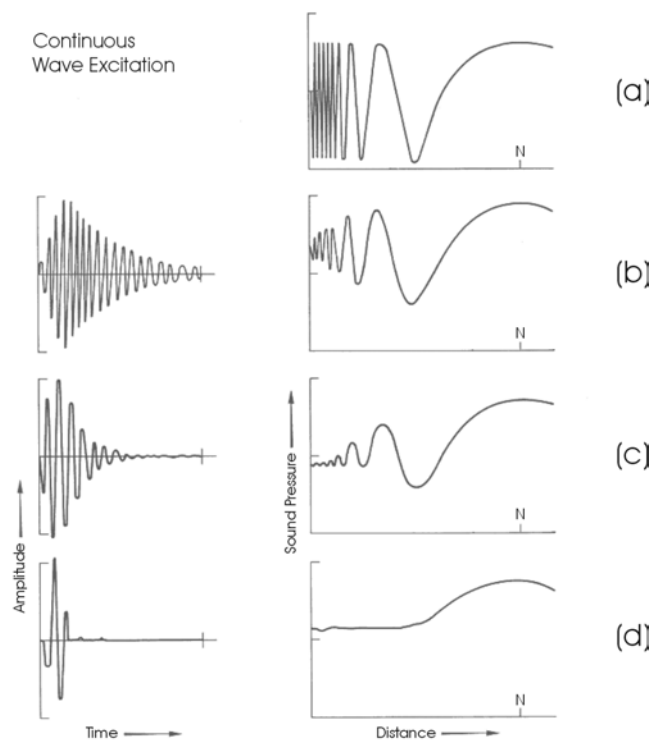


Figure 2-21: Influence of excitation mode on the axial sound pressure in the near-field region. [14]

Even though the homogeneity of the near-field beam amplitude is improved by pulse-echo applications, the short distance between transducer and near reflectors leads to difficulties for accurate signal processing. Consequently, velocity measurements inside the near-field region should be avoided.

In general, the sound pressure along the axis of the transducer is given by

$$p = 2p_0 \cdot \sin \left[ \left( \frac{\pi}{\lambda} \sqrt{\left( \frac{D}{2} \right)^2 + z^2} \right) - z \right] \quad (2.16)$$

where

|           |   |
|-----------|---|
| $p$       | acoustic pressure along transducer axis [N/m <sup>2</sup> ] |
| $p_0$     | initial pressure on transducer surface [N/m <sup>2</sup> ]  |
| $\lambda$ | ultrasonic wavelength in test medium [mm]                   |
| $D$       | diameter of active element [m]                              |
| $z$       | axial distance from transducer [m]                          |

The equation is commonly used to describe the near-field in front of a CW mode transducer, for example in Figure 2-21a, but it is also valid in the far-field region. For large axial distances, the equation above can be approximated by the inverse-square law for point sources:

$$p \approx 2p_0 \cdot \sin \left( \frac{\pi \cdot D^2}{8 \cdot \lambda \cdot z} \right) \approx p_0 \frac{\pi \cdot D^2}{4 \cdot \lambda \cdot z} = p_0 \frac{\pi \cdot N}{z} \quad (2.17)$$

where

|     |   |
|-----|---|
| $p$ | acoustic pressure in the far-field region [N/m <sup>2</sup> ] |
| $N$ | length of near-field region [m]                               |

The solid line in Figure 2-22 illustrates the sound pressure in the far-field region according to Equation 2.16. The maximum of  $2p_0$  is reached at the natural focal point  $N$ , from which the sound pressure falls off with distance. After the initial value  $p_0$  is reached at a distance of  $3N$ , the pressure decrease can be approximated by Equation 2.17 (dashed line).

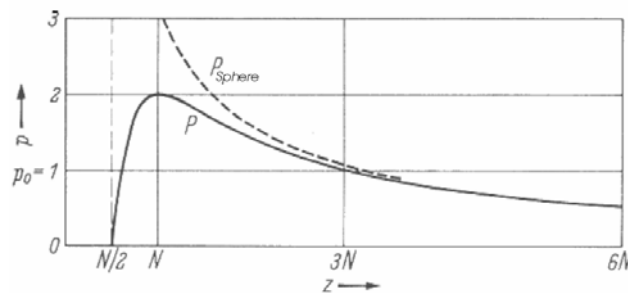


Figure 2-22: Axial sound pressure in the far-field region and its approximation. [14]

In contrast to the near-field sound pressure, the sound pressure in the far-field region is not influenced along the beam axis by the mode of excitation.

Yet the shape of the far-field side lobes depends upon the length of the transmitted pulse. CW excitation produces a field of radially alternating lobes and minima with an amplitude variation as illustrated in Figure 2-23a, while in a short PW excitation the minima disappear and we get an angular variation of the field amplitude as illustrated in Figure 2-23b.

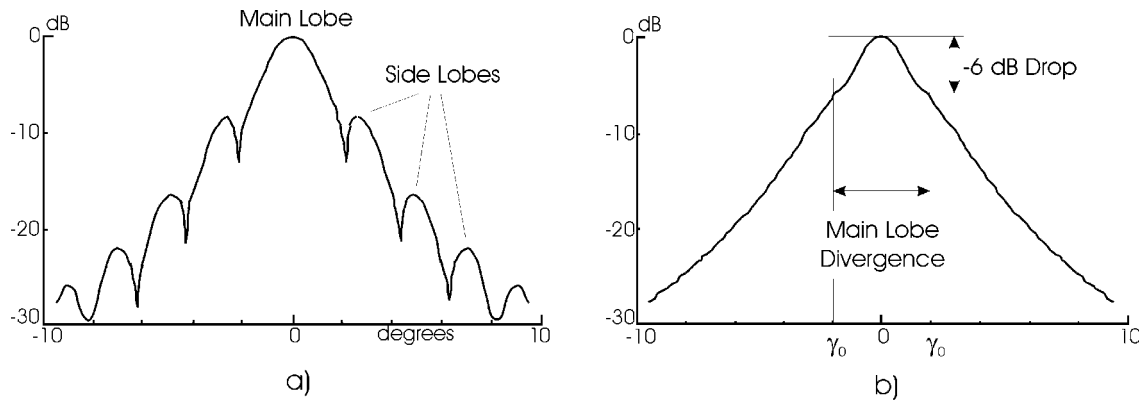


Figure 2-23: Angular variation of the beam amplitude in the far-field region; CW (a) and PW (b) excitation. [3]

The width of the main lobe is defined as where the amplitude has fallen 6 dB from the axial value, which is equal to a 50 percent reduction of sound pressure. This pressure drop of 50 percent diverges with the sound beam at a constant angle. In the sound field emitted by a plane circular transducer this so called *half-angle of divergence* is given by

$$\gamma_0 = \sin^{-1}\left(0.514 \frac{\lambda}{D}\right) \quad (2.18)$$

where

|            |  |
|------------|--|
| $\gamma_0$ | half-angle of divergence [deg]           |
| $\lambda$  | ultrasonic wavelength in test medium [m] |
| $D$        | diameter of active element [m]           |

We see that the length of the near-field region and the half-angle of divergence in the far-field region both depend on the transducer frequency ( $\lambda$  in the propagation medium) and the aperture size. With a constant aperture, increasing the frequency increases the length of the near-field region and decreases the angle  $\gamma_0$ , producing a directional beam pattern suitable for ultrasonic velocity profile measurements. Decreasing the aperture size at a constant frequency causes a shorter near-field region and a larger divergence, producing the desired beam pattern for an omnidirectional hydrophone, used primarily for detecting sound waves from an underwater source such as a submarine.

Some values for near-field region length and main lobe divergence of plane circular transducers in 20° water are given in Table 2-6. The proper combination for velocity profile measurements is chosen such that the active diameter of the transducer is at least ten times longer than the corresponding wavelength ( $D \geq 10\lambda$ ). The combinations of transducer diameter and frequency that were used within the experimental phase of this thesis are highlighted.

| Transducer Diameter D [mm] | Length of Near-Field Region N [mm]        |                                  |                                  |                                  |                                  |
|----------------------------|---|----------------------------------|----------------------------------|----------------------------------|----------------------------------|
|                            | Half-Angle of Divergence $\gamma_0$ [deg] |                                  |                                  |                                  |                                  |
|                            | f = 0.5 MHz<br>$\lambda = 2.96$ mm        | f = 1 MHz<br>$\lambda = 1.48$ mm | f = 2 MHz<br>$\lambda = 0.74$ mm | f = 4 MHz<br>$\lambda = 0.37$ mm | f = 8 MHz<br>$\lambda = 0.19$ mm |
| 1                          | 0.08<br>-                                 | 0.17<br>50                       | 0.34<br>22                       | 0.68<br>11                       | 1.3<br>5.6                       |
| 2                          | 0.34<br>50                                | 0.68<br>22                       | 1.4<br>11                        | 2.7<br>5.5                       | 5.3<br>2.8                       |
| 2.5                        | 0.53<br>37                                | 1.1<br>18                        | 2.1<br>8.8                       | 4.2<br>4.4                       | 8.2<br>2.2                       |
| 3                          | 0.76<br>30                                | 1.5<br>15                        | 3.0<br>7.3                       | 6.1<br>3.6                       | 11.8<br>1.9                      |
| 4                          | 1.4<br>22                                 | 2.7<br>11                        | 5.4<br>5.5                       | 10.8<br>2.7                      | 21.1<br>1.4                      |
| 5                          | 2.1<br>18                                 | 4.2<br>8.8                       | 8.4<br>4.4                       | <b>16.9</b><br><b>2.2</b>        | 32.9<br>1.1                      |
| 8                          | 5.4<br>11                                 | 10.8<br>5.5                      | 21.6<br>2.7                      | 43.2<br>1.4                      | 84.2<br>0.70                     |
| 10                         | 8.4<br>8.8                                | 16.9<br>4.4                      | <b>33.8</b><br><b>2.2</b>        | 67.6<br>1.1                      | 132<br>0.56                      |
| 20                         | 33.8<br>4.4                               | 67.6<br>2.2                      | 135<br>1.1                       | 270<br>0.54                      | 526<br>0.28                      |

Table 2-6: Sound field properties in 20°C water as a function of transducer diameter and operating frequency.

In reality, the sound pressure in the far-field region decreases not only because of the beam spread but also due to attenuation. According to Equations 2.8 and 2.17, the axial sound pressure is then given by

$$p = p_0 \cdot \frac{\pi \cdot N}{z} \cdot 10^{-\frac{\alpha \cdot z}{20}} \quad (2.19)$$

where

- $p$  axial sound pressure in the far-field region [N/m<sup>2</sup>]
- $p_0$  initial pressure on transducer surface [N/m<sup>2</sup>]
- $N$  length of near-field region [m]
- $z$  axial distance from transducer [m]
- $\alpha$  coefficient of attenuation [dB/m]



---

### 3 Ultrasonic Velocity Profile Measurements

---

In the third chapter, we will take a closer look at one specific application of ultrasound in the field of fluid engineering: the ultrasound-pulse-Doppler method for velocity profile measurements. It exemplifies a non-intrusive technique to measure complete velocity profiles of fluid flow. In contrast to conventional Laser-Doppler-Anemometry (LDA), where one has to move the measuring apparatus to detect a complete velocity profile, the pulse Doppler method provides instantaneous results due to its measurement of velocity at a multitude of points along the axis of the ultrasound beam.

As indicated by its name, the ultrasound-pulse-Doppler technique uses the Doppler effect in which a sound wave, scattered by a moving particle, is subjected to a frequency shift, which is proportional to the velocity of the particle. When we assume that the reflecting particle is small enough to represent the fluid flow adequately, its velocity equals the velocity of the fluid. The position of the particle can be determined from the length of time between the emission of the ultrasound wave to the reception of its echo, if the speed of sound in the medium is known. If the echoes are received continuously within definite time windows, a complete velocity profile can be obtained, as shown in Figure 3-1.

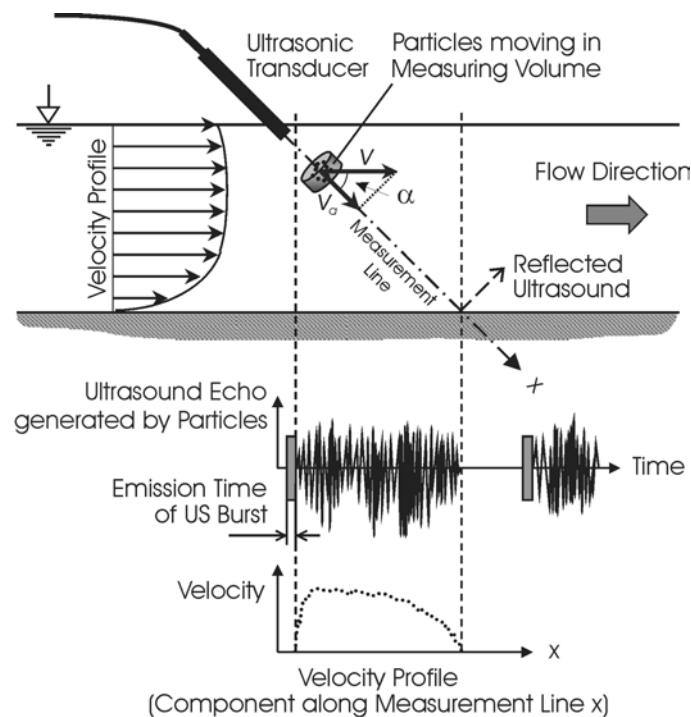


Figure 3-1: Ultrasonic velocity profile measurements of open channel flow. [19]

---

### 3.1 Doppler Effect

---

The Doppler effect describes the apparent shift in the observed frequency of a wave due to relative motion between the source and the observer. The frequency increases when the source and observer approach each other and decreases when they move apart. The effect was first explained in 1842 by the Austrian scientist Christian Doppler (1803-1853). Although first discovered in sound waves, the Doppler effect holds true for all types of waves.

The Doppler shift for sound waves depends not only on the relative motion of observer and source but also on which one is in motion. This situation is fundamentally different from other waves in the case of light waves. The difference stems from Einstein's theory of relativity, which states that the speed of light remains constant in all reference frames (Albert Einstein, 1879-1955, American-German physicist). Since light needs no medium to support its propagation, its speed relative to the source or observer is always the same. Therefore, it is only the relative motion between the observer and the source that determines the Doppler shift frequency. The Doppler effect for light waves is usually described in terms of colors rather than frequency. A red shift occurs when the source and observer move away from each other, while a blue shift occurs when the two travel toward each other. A well-known example is the red-shifted light of distant galaxies that is considered proof for the expansion of our universe.

In Figure 3-2, we examine the Doppler shift for ultrasonic waves. First, we consider a stationary source (S) and a moving observer (O), as shown in Figure 3-2a. The circles denote successive wave fronts (regions of identical high pressure) of the emitted sound waves. If the observer moves toward the source, the wave fronts reach the observer more frequently than if it were stationary. The distance between wave fronts ( $\lambda$ ) does not change, but the number of wave fronts passed through per unit time (the detected frequency) increases.

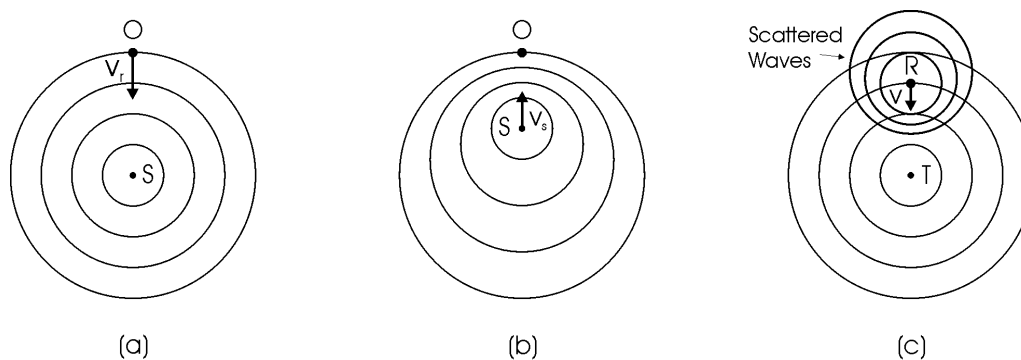


Figure 3-2: Doppler effect for sound waves; moving receiver (a), moving source (b), and moving reflector (c).

The frequency perceived by the moving observer is

$$f' = f_0 \left( 1 \pm \frac{v_r}{c} \right) \quad (3.1)$$

where

|       |   |
|-------|---|
| $f'$  | frequency received by observer [Hz]       |
| $f_0$ | actual frequency of source [Hz]           |
| $c$   | speed of wave propagation in medium [m/s] |
| $v_r$ | speed of observer [m/s]                   |

The minus (-) sign is used when the observer moves away from the source.

If, instead, the source is moving and the observer is stationary, as depicted in Figure 3-2b, the wavelength of the emitted sound waves changes. In the case of the source traveling toward the receiver, the wavelength in front of the approaching source shortens and the frequency perceived by the observer increases. The received frequency is

$$f' = f_0 \left( 1 \mp \frac{v_s}{c} \right)^{-1} \quad (3.2)$$

where

|       |                       |
|-------|-----------------------|
| $v_s$ | speed of source [m/s] |
|-------|-----------------------|

The minus (-) sign corresponds to a source moving toward the transducer, while the plus (+) sign is used for a receding source. Thus the received frequency increases when the source approaches the observer, while it decreases when the source moves away. Most of us have experienced this phenomenon, probably in a situation where a car or a motorcycle passed by at high speed. The frequency of the engine sound rises as the vehicle approaches and falls as the vehicle moves away.

In Figure 3-2c, we consider an ultrasonic transducer (T) that remains stationary while emitting waves that are, subsequently, scattered by a reflector (R). Immediately after emitting a short pulse of ultrasound, the transducer is switched into receive mode to detect the frequency of the reflected waves. The moving reflector acts as a combination of both a moving receiver and source. The frequency perceived by the reflector is shifted according to Equation 3.1, and the echo that leaves the reflector is shifted again according to Equation 3.2. Thus, the reflected waves get Doppler shifted twice.

The frequency detected by the stationary transducer is obtained by combining the previous two equations:

$$f' = f_0 \left( \frac{c \pm v}{c \mp v} \right) \quad (3.3)$$

where  $v$  speed of reflector [m/s]

The upper set of signs applies if the reflector is approaching the transducer, and the lower set of signs is used if it is receding.

Regular flow speeds in experimental hydraulics are no more than a few percent of the speed of sound in water ( $v \ll c$ ). When the speed of the reflector is small compared to the wave propagation speed, the denominator in Equation 3.3 may be simplified.

Using the binomial expansion theorem, given by

$$(1 \pm x)^{-1} = 1 \mp x + x^2 \mp x^3 \dots \quad \text{for } |x| < 1 \quad (3.4)$$

the received frequency becomes

$$f' = f_0 \left( \frac{1 \pm \frac{v}{c}}{1 \mp \frac{v}{c}} \right) = f_0 \left( 1 \pm \frac{v}{c} \right)^2 = f_0 \left( 1 \pm \frac{2v}{c} \right) \quad (3.5)$$

The difference between the frequencies of the emitted and received signals, called the Doppler shift frequency, is

$$f_d = f_0 - f' = f_0 \frac{2v}{c} \quad (3.6)$$

A positive Doppler shift occurs when the reflector moves toward the transducer, while a negative frequency shift is caused by a receding reflector. The factor of two results from the two Doppler shifts occurring on reflection of the emitted ultrasound pulse.

The equation indicates that the Doppler shift is proportional to the speed of the moving object, more specifically, to the ratio of the speed of the moving object to the speed of the wave propagation. This is why the Doppler effect is experienced firsthand with sound ( $c = 330$  m/s in air), but not with light ( $c \approx 300,000$  km/s). Only astronomical motions provide speeds great enough to produce a readily observable Doppler effect.

It is the Doppler shift frequency that the instruments detect. However, it is the speed of motion in which we are normally interested. Thus, Equation 3.6 can be rearranged, resulting in

$$v = \frac{c \cdot f_d}{2 \cdot f_0} \tag{3.7}$$

|       |       |  |
|-------|-------|--|
| where | $v$   | speed of particle [m/s]                    |
|       | $f_d$ | detected Doppler shift frequency [Hz]      |
|       | $c$   | speed of sound in propagation medium [m/s] |
|       | $f_0$ | frequency emitted by transducer [Hz]       |

---

### 3.2 Principle of Ultrasound-Pulse-Doppler

---

In Figure 3-3, we consider an ultrasonic transducer that emits short pulses of frequency  $f_0$  and remains fixed in a medium where the speed of sound is given by  $c$ . A particle moving with velocity  $v$  will partially reflect the waves back to the transducer if its acoustic impedance is different from that of the surrounding medium.

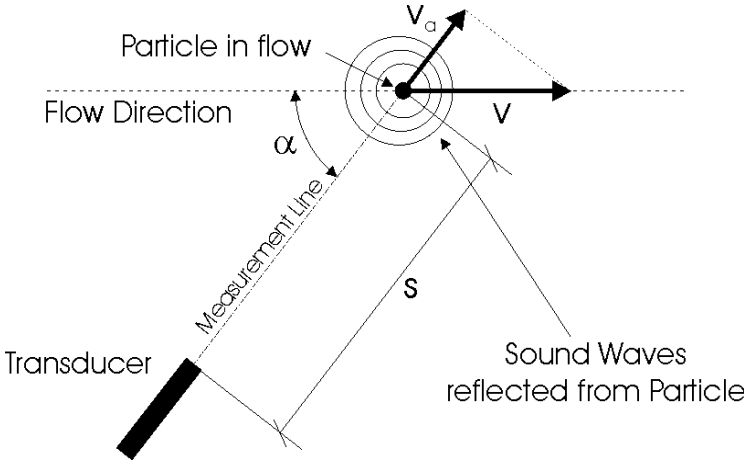


Figure 3-3: Functional principle of ultrasound-pulse-Doppler. [29]

The trajectory of the particle forms an angle  $\alpha$ , called the *Doppler angle*, with respect to the propagation direction of the ultrasonic waves along the transducer axis. Since only the velocity component  $v_a$  along the line of measurement contributes to the Doppler shift, one must calculate the frequency shift in the flow direction using the cosine of the angle  $\alpha$  between the flow velocity vector and the transducer axis.

According to Equation 3.7, the velocity of the particle can then be expressed as

$$v = \frac{v_a}{\cos \alpha} = \frac{f_d \cdot c}{2 \cdot f_0 \cdot \cos \alpha} \quad (3.8)$$

|       |          |  |
|-------|----------|--|
| where | $v$      | speed of particle [m/s]                    |
|       | $v_a$    | velocity component along probe axis [m/s]  |
|       | $\alpha$ | Doppler angle                              |
|       | $f_d$    | detected Doppler shift frequency [Hz]      |
|       | $c$      | speed of sound in propagation medium [m/s] |
|       | $f_0$    | frequency emitted by transducer [Hz]       |

Information about the position of the particle is given by the echography relationship, which relates the distance of the reflector to the time delay between the emission of the wave and the echo reception. From the time interval and the speed of sound in the propagation medium, the position of the particle can be calculated.

$$s = \frac{c \cdot \Delta t}{2} \quad (3.9)$$

|       |            |   |
|-------|------------|---|
| where | $s$        | distance of the particle from the transducer [m]    |
|       | $\Delta t$ | time delay between pulse emission and reception [s] |

The factor of one half results from the fact that the ultrasonic pulse covers the distance between transducer and particle twice, thus only half of the time delay  $\Delta t$  equals this distance.

If the measurement instrument succeeds in detecting the Doppler shift frequency  $f_d$  and the time delay  $\Delta t$ , the position and the velocity of the traveling particle can be calculated. To obtain a complete velocity profile, one has to separate the Doppler signal generated by different particles along the transmitted ultrasound beam. Instead of measuring the time delay between emission and reception, the returning echo signal is sampled at specific time intervals, respectively at a multitude of depths. Each measurement then contains the composite Doppler signal from a sample volume at a particular range. The signals from neighboring depths arrive at a different time and can be sorted into separate channels, thereby allowing measurement of velocity at a multitude of points along the axis of the ultrasound beam. If this procedure is repeated many times, accurate and complete velocity profiles are obtained.

### 3.3 Doppler Angle

The Doppler angle plays an important role in the calculation of the particle velocity. As seen from Equation 3.8, the dependence on the Doppler angle is in the form of a cosine. The cosine of the Doppler angle provides the component of the true flow velocity vector projected onto the line of measurement. For a given main flow direction, changing the Doppler angle changes the size of the detected velocity component  $v_a$ , as Figure 3-4 demonstrates on an example of free-surface flow.

If the propagation direction of the ultrasonic waves and the flow direction are the same, as illustrated in Figure 3-4a, the maximum measurable Doppler shift is obtained. If the angle between these two directions is non-zero, a less significant frequency shift will occur, as shown in Figure 3-4b. This setup is recommended for the measurement of cross-sectional velocity profiles. The velocity in the direction of the main flow is then calculated by multiplying the detected velocity component  $v_a$  with the factor  $1/\cos\alpha$ . The fact that the detectable velocity is limited due to the sampling theorem, which is discussed later in section 3.4, can be compensated by selecting a specific Doppler angle at which the measured velocity component  $v_a$  fits inside the measurable velocity range.

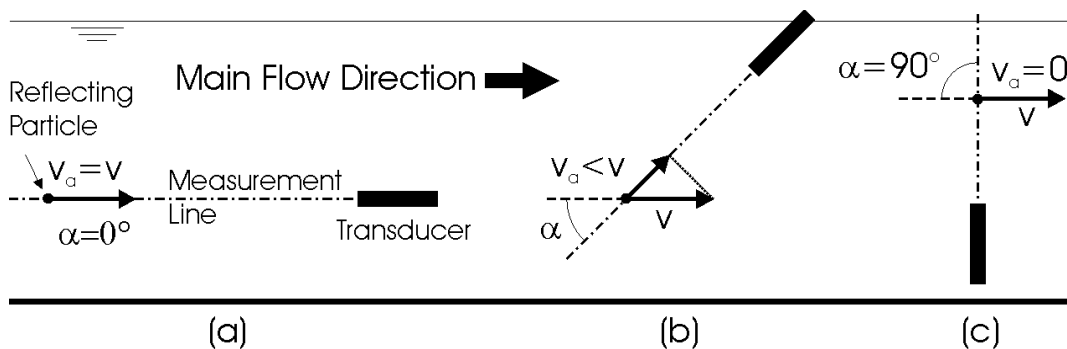


Figure 3-4: Doppler angle variation for a given flow direction and its effect on the detected velocity component.

If the reflecting particles travel perpendicular to the measurement line, as shown in Figure 3-4c, no flow velocity will be detected since its component  $v_a$  along the line of measurement equals zero. However, the latter setup turned out to be the best choice for surface level measurements, in which the position of the water table is recorded over time. Because no echo from horizontal movement in the liquid is detected, the up and down movement of the water surface becomes visible (see Chapter 5).

Speed calculations based on Doppler shift measurements can only be done with knowledge of the Doppler angle involved. A central problem is that real flows are usually three-dimensional and thus the true direction of the velocity vector remains unknown. If the flow direction is known, as in laminar pipe flows, the Doppler angle can be predicted exactly. In addition, one must pay attention to avoid wrong calculations when the ultrasonic transducer is fixed outside the tube wall. As the waves are refracted at the tube wall, the propagation direction of the ultrasonic waves (line of measurement) may deviate from the transducer axis. In such a case, the transmission angle can be calculated using Snell's Law if the speed of sound inside the wall material is known precisely.

Error in the estimation of the Doppler angle is more critical at large angles than it is at small ones, because the frequency shift becomes very small at large angles and the system sensitivity is reduced. Figure 3-5 demonstrates the importance of using the smallest possible Doppler angle in performing flow measurements. For example, an uncertainty of  $\pm 1^\circ$  at a Doppler angle of  $80^\circ$  will lead to an error of about 10 % in the calculation of velocity. Thus it is very important to accurately determine the transducer angle when obtaining cross-sectional velocity profiles as in Figure 3-4b. As a rule, the closer the measurement line is to the flow direction, the more accurate the velocity measurement will be.

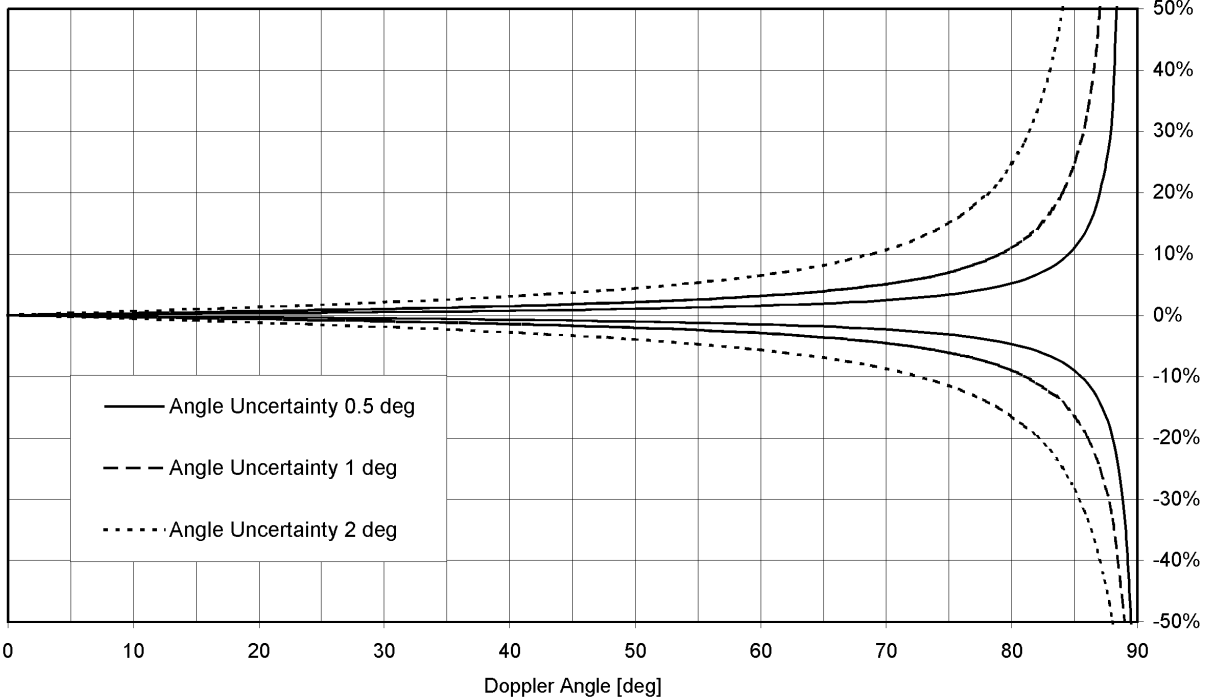


Figure 3-5: Effect of Doppler angle error on velocity measurement. [7]



---

### 3.4 Signal Sampling

---

In the ultrasound-pulse-Doppler system, the emitted ultrasonic waves are pulsed continuously. Immediately after emitting a pulse, the transducer is switched into the receive mode to detect the returning echo signal. According to the direct piezoelectric effect, the mechanical energy of the returning wave is transferred into an electrical voltage. In the subsequent process of analog to digital conversion, the analog signal is converted into a digital signal which is then stored for further signal processing. After a certain time, which depends on the pulse repetition frequency and is given by the selected measurement depth, the system switches back to the emission mode and the next pulse is emitted by the transducer.

The object of A/D conversion is to convert the analog signal into a digital representation. This is done by sampling the signal at discrete points. These points are usually evenly spaced in time, where the time between is referred to as the *sampling interval*. In pulse Doppler systems, the sampling interval is given by the time interval between two successive pulse emissions. Hence the sampling rate, given by the inverse of the sampling interval, is equal to the *pulse repetition frequency*. By sampling the echo signal at this specific frequency, the Doppler shift frequency can be reconstructed when enough samples have been taken.

The choice of the sampling frequency is an important decision. Generally speaking, higher frequency content in the analog signal will require a higher sampling rate to reproduce it faithfully. In fact, it can be proven mathematically that the sampling rate must be twice the highest frequency contained in the analog signal. The highest frequency that can be accurately sampled is known as the *Nyquist frequency* (Harry Nyquist, 1889-1976, Swedish-American physicist) and is given by

$$f_{\max} \leq \frac{f_s}{2} = f_N \quad (3.10)$$

where  $f_{\max}$  highest frequency content in analog signal [Hz]  
 $f_s$  sampling frequency [Hz]

The above equation, often referred to as the *Nyquist sampling theorem*, has a lot of practical relevance. For instance, the sampling rate of 44.1 kHz for CD Audio was not chosen randomly. It is somewhat higher than twice the range of human hearing (20 kHz) to guarantee excellent music reproduction.

The sampling of a sine wave using two different sampling rates is illustrated in Figure 3-6. The time steps at which A/D conversion is made are given by the vertical lines beneath the signal, while the asterisks on the waveform show the voltages that are sampled. Note that the sampling rate in Figure 3-6a is about ten times higher than the highest frequency present in the signal and so is about five times the Nyquist rate. The sampled signal is thus a reasonable approximation of the analog signal.

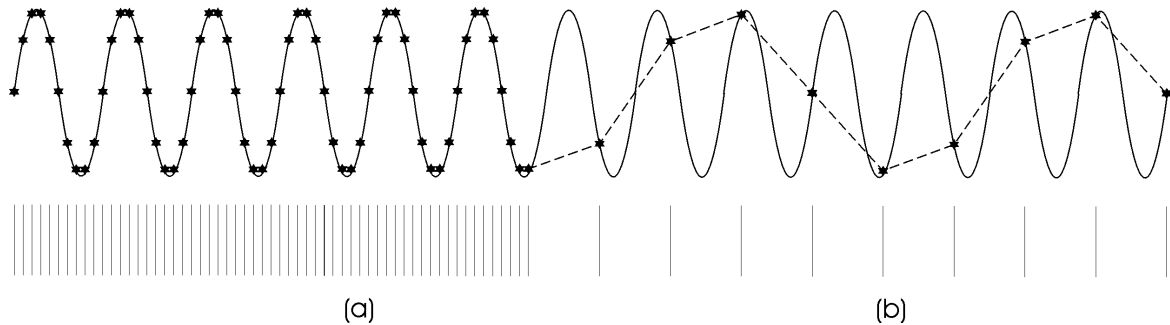


Figure 3-6: Sampling of a sine wave using a frequency (a) above and (b) below twice the Nyquist frequency ( $2f_N$ )

Figure 3-6b shows the situation that results when the sampling rate is reduced to about 1.2 times the highest frequency contained in the analog signal. The sampling rate is thus lower than the Nyquist frequency, and the sampled signal (dashed line) bears little resemblance to the analog signal. The frequency of the sampled signal is much smaller than that of the analog signal. This error, known as *aliasing*, is the result of an improper choice of the sampling rate.

For a signal frequency that increases linearly we will detect a frequency, which behaves as shown in Figure 3-7. The frequency starts from zero, but when it increases above  $f_N$ , it will be sampled to a negative frequency at  $-f_N$ . Each time the frequency of the sampled signal passes the Nyquist frequency, it is folded back in the low frequency region. The consequence for pulse Doppler applications is obvious: the maximum detectable Doppler shift frequency is limited.

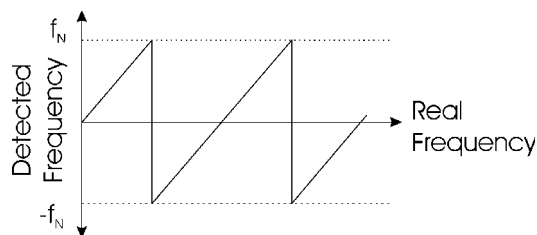


Figure 3-7: Backfold of detected frequency due to aliasing. [25]

---

### 3.5 Measurable Depth and Measurable Velocity

---

With velocity profile measurements, the pulse repetition frequency, equal to the sampling rate, is regulated by the position of the measurement window. To be more precise, it depends on the measurement depth, which is selected by the operator. To avoid range ambiguities, the echo signal from the most distant particle must be received before the next pulse is emitted. Thus the time interval between two successive pulse emissions is governed by the time that is required to cover the measurement depth twice, as given by the echography relationship. The maximum value of the pulse repetition frequency is then

$$f_{prf} \leq \frac{c}{2 \cdot s_{max}} \quad (3.11)$$

where

|           |  |
|-----------|--|
| $f_{prf}$ | pulse repetition frequency [Hz]            |
| $c$       | speed of sound in propagation medium [m/s] |
| $s_{max}$ | measurement depth [m]                      |

The pulse repetition frequency is set automatically when the position of the measurement window is changed by the operator. The Nyquist sampling theorem now mandates that the pulse repetition frequency must be twice the highest frequency to be measured. In the case of pulse Doppler systems, it is the Doppler shift frequency that is detected to calculate the target velocity. According to Equation 3.10, the detectable Doppler shift frequency becomes

$$f_d \leq \frac{f_{prf}}{2} \quad (3.12)$$

where

|       |   |
|-------|---|
| $f_d$ | detectable Doppler shift frequency [Hz] |
|-------|---|

If the measurable Doppler frequency is limited, the maximum velocity that is calculated from the Doppler shift is limited too. With the previous two equations and Equation 3.7, the maximum measurable velocity becomes

$$v_{max} = \frac{c \cdot f_d}{2 \cdot f_0} = \frac{c \cdot f_{prf}}{4 \cdot f_0} = \frac{c^2}{8 \cdot f_0 \cdot s_{max}} \quad (3.13)$$

where

|           |                                      |
|-----------|--------------------------------------|
| $v_{max}$ | maximum measurable velocity [m/s]    |
| $f_0$     | frequency emitted by transducer [Hz] |

For a given frequency we have to make a compromise between measurable depth and measurable velocity. By reducing the transducer frequency, faster velocities can be perceived at the same measurement depth. However, due to the fact that the size of a single measurement volume depends on the ultrasonic wavelength, spatial resolution will be reduced. Figure 3-8 demonstrates the relationship between measurement depth and measurable velocity for common operating frequencies. The numbers were calculated for water ( $c = 1480 \text{ m/s}$ ) and a Doppler angle of zero degrees, thus applying to an experimental setup as shown in Figure 3-4a.

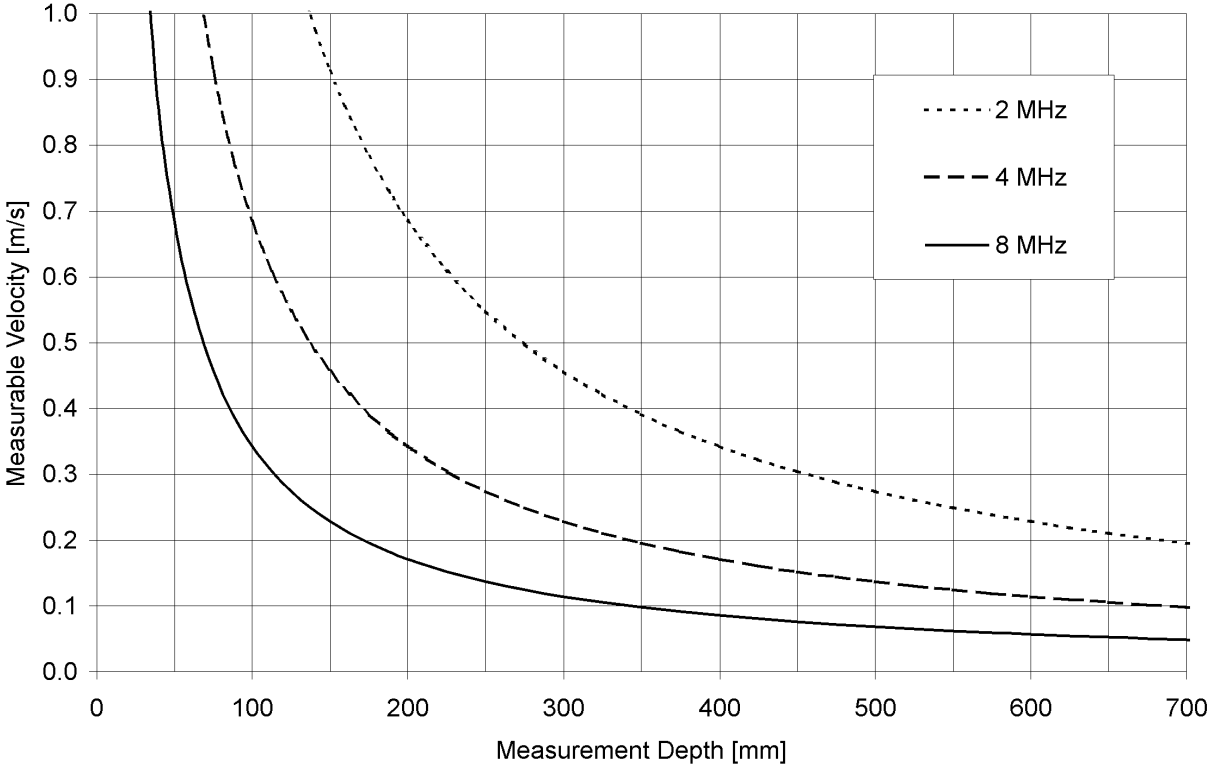


Figure 3-8: Relationship between measurement depth and measurable velocity for common working frequencies.

The problem of limited velocity range is the main drawback of ultrasound-pulse-Doppler. Unfortunately, velocities encountered in experimental hydraulics are often faster than the measurable velocities in Figure 3-8 and thus produce aliasing. When aliasing occurs, velocities beyond the measurable value appear to wrap around to opposite the flow direction. To avoid this phenomenon, the operator must extend the velocity range by choosing a measurement setup with non-zero Doppler angle, as displayed in Figure 3-4b. The measurable velocity is then scaled with the factor  $1/\cos\alpha$ . Figure 3-9 and Figure 3-10 illustrate how the velocity range can be extended with increasing Doppler angle. For best possible velocity resolution, one should choose a Doppler angle that closely fits to the expected velocity.

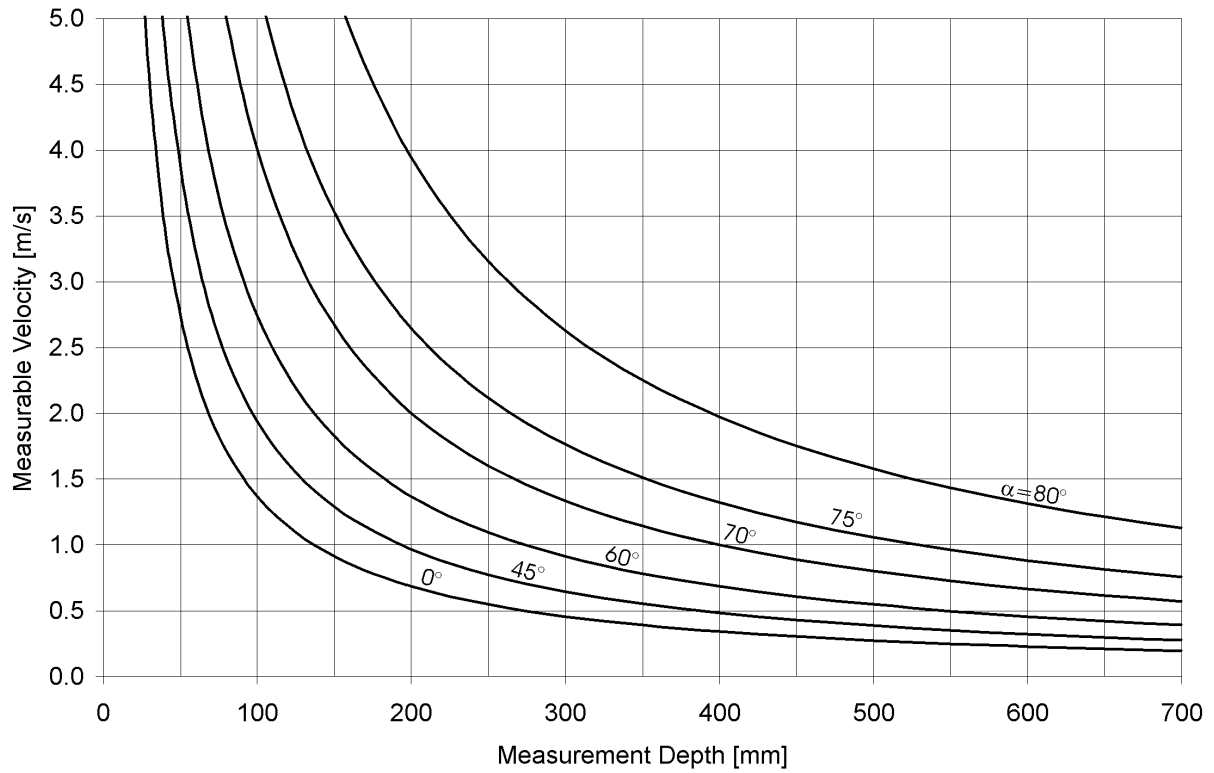


Figure 3-9: Measurable velocity for an operating frequency of 2 MHz as a function of the Doppler angle  $\alpha$ .

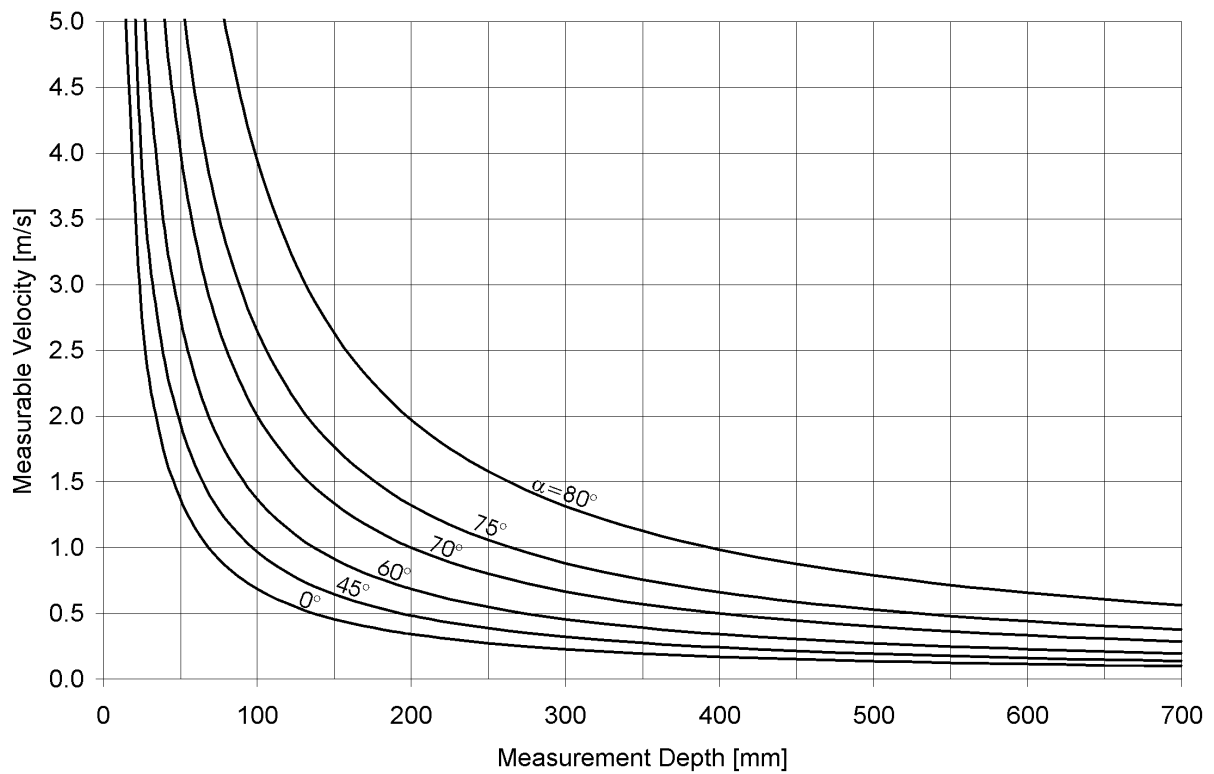


Figure 3-10: Measurable velocity for an operating frequency of 4 MHz as a function of the Doppler angle  $\alpha$ .

The second method of extending the velocity range is to ignore the direction of flow. Usually, the flow direction is detected with the Doppler shift: a positive frequency shift occurs when the traveling particles move toward the transducer, while a negative frequency shift is caused by receding particles. The detected frequency is then converted into an 8-digit binary number for data processing. To indicate whether the frequency shift is positive or negative, one bit is required for sign detection. The velocity range is identical for positive and negative velocities, with the maximum measurable value given by Equation 3.13.

If the sign detection is ignored, more data bits are available to stand for either a positive or a negative frequency shift. The aliasing phenomenon can be corrected during data processing, because the backfolded frequencies can be identified. The maximum measurable velocity is thereby doubled and given by

$$v_{\max} = \frac{c^2}{4 \cdot f_0 \cdot s_{\max}} \tag{3.14}$$

where  $v_{\max}$  maximum measurable velocity without sign detection [m/s]

Particularly when the flow direction is known to be unidirectional along the line of measurement, it is very useful to ignore the sign detection and thus double the measurable velocity. Some instruments (Signal Processing) allow for selection different ranges for positive and negative values without losing information about the flow direction.

### 3.6 Measurement Window

The ability to establish the velocity at many separate points along the line of measurement represents the key feature of the pulse Doppler technique. The positions of these measurement volumes, their size and their distance from each other can be selected by the operator within certain limits. The implications of this are clear: flow at different depths or at different points within the test medium can be selectively monitored. Figure 3-11 presents a graphic illustration of the measurement window and its position inside the main lobe of the ultrasonic beam. Because the echo signals from different sample volumes are stored in separate signal channels, the term *channel* is frequently used to describe a single measurement volume. The width of the measurement window is then defined as the distance between channel 0 (start channel) and channel 127 (end channel).

Obviously, the position of the measurement window is limited by the minimum and maximum depth. The minimum measurable depth is ruled by the time the system needs to switch from transmission mode to receive mode and cannot be set by the operator. Typically, the minimum measurable depth is less than 5 mm. However, due to the oscillating sound pressure amplitude in the near-field of the ultrasonic beam, the Doppler shift may not be obtained correctly if the measurement window starts at the minimum depth. In this case it is recommended to move the window a few millimeters away from the transducer.

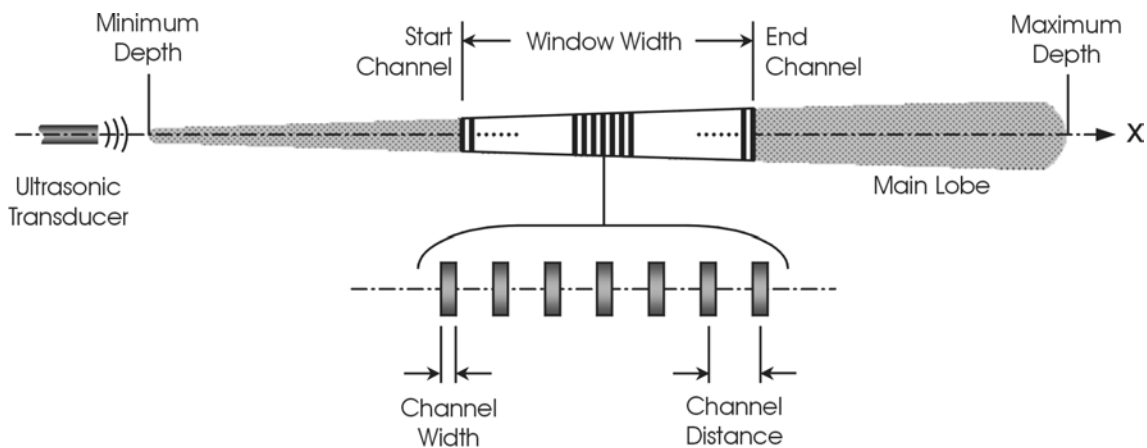


Figure 3-11: Terms related to the measurement window and their position inside the ultrasonic beam. [19]

The maximum depth is set by the operator according to the region of interest. Considering the relationship between measurement depth and measurable velocity, given by Equation 3.13, one should choose the smallest possible depth. The maximum depth determines the pulse repetition frequency, given by Equation 3.11, and therefore influences the temporal resolution, defined as the time between two measured velocity profiles.

The basic concept of how pulse Doppler systems can detect the position of reflecting particles inside the measurement window is related to the process of range gating. In looking for the return echo signals, the Doppler system samples only those signals occurring in a narrow time window after each transmitted pulse, called a *range gate*. At an operator-selected time (depth) after pulse transmission, the range gate opens and the echo signals are recorded in the subsequent sampling process. An instant later, the range gate closes, and the next pulse is emitted after the current pulse has passed the maximum depth. The duration of the range gate determines the range of depths interrogated in the Doppler measurement and thus defines the width of the measurement window.

To obtain a complete velocity profile, one must sample the gated echo signal at specific times separated by the time interval  $\Delta t_s$ , as Figure 3-12 depicts. Due to the echography relationship, the delay time  $\Delta t_i$  between pulse emission and time of sampling is proportional to the location of the observed region. If this delay time remains fixed over all pulse emissions, the Doppler frequency can be reconstructed for a specific volume in space.

To separate the echo signals generated by different particles, the samples are stored in individual signal channels, each one representing a sample volume at a particular range. The time interval  $\Delta t_s$  between two channels determines the distance of adjacent sample volumes (channel distance), while the size of a sample volume (channel width) is governed by the length of the ultrasonic pulse  $t_p$ .

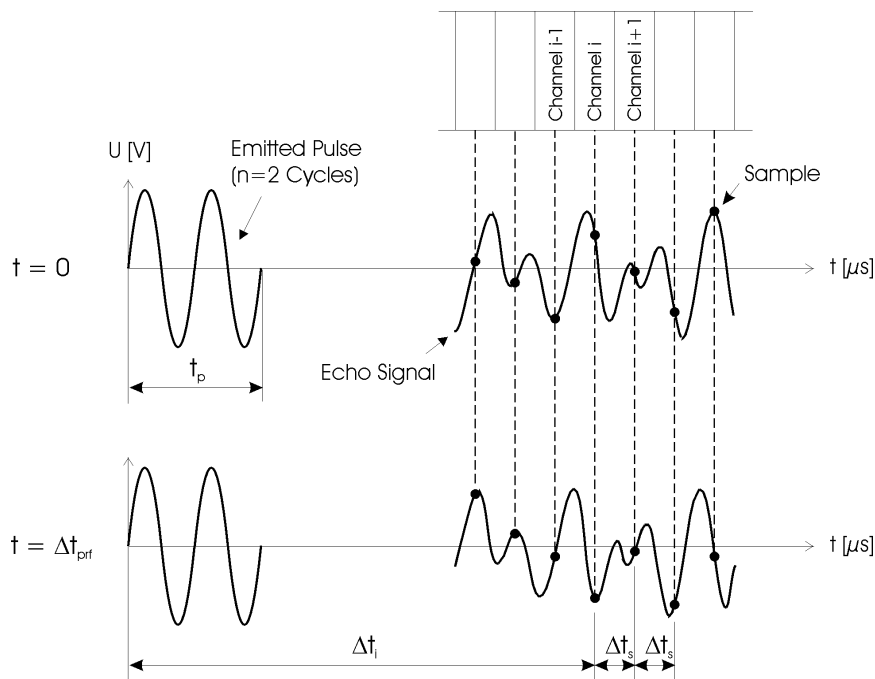


Figure 3-12: Sampling of the gated echo signal at specific times separated by the time interval  $\Delta t_s$ . [5]

To reconstruct the Doppler frequency correctly, more than one sample is required. Since the returning echo is sampled at each pulse transmission, velocity profile measurements can only be obtained after multiple pulse transmissions, the minimum being eight pulse repetitions. The sampling interval is then given by the time interval  $\Delta t_{prf}$  between two successive pulse emissions. The time interval  $\Delta t_{prf}$ , which is the inverse of the pulse repetition frequency, and the number of pulse repetitions used in the Doppler shift calculation determine the temporal resolution of the velocity profile measurements.



---

### 3.7 Spatial Resolution

---

Spatial resolution is defined as the ability to distinguish between two closely spaced objects. In pulse Doppler systems, it is given by the size of a single measurement volume. The smaller the volume size, the better the spatial resolution. A high spatial resolution is important when, for example, flows in small pipes are investigated. A disadvantage of high spatial resolution is that with small sample volumes only a few particles move through the volume and contribute to the frequency shift associated with that volume. If the particle concentration in the test medium is not sufficient to generate significant echo, it can help to increase the size of the sample volumes at the cost of decreased spatial resolution.

The shape of a sample volume (channel) is depicted in Figure 3-11. Because of the beam divergence, the sample volume bears a resemblance to a diverging truncated cone. However, within its height, the variation in cross-sectional area is so small that the measurement volume can be approximated by a cylindrical slab. The diameter of the measurement slab is proportional to the width of the main lobe, which is a function of both transducer diameter and operating frequency. The height of the sample volume (channel width) is proportional to the length of the transmitted ultrasonic pulse, due to the echography relationship.

$$w = \frac{\lambda_0 \cdot n_{cyc}}{2} \quad (3.15)$$

|       |             |                                |
|-------|-------------|--------------------------------|
| where | $w$         | channel width [m]              |
|       | $\lambda_0$ | acoustic wavelength [m]        |
|       | $n_{cyc}$   | number of cycles per pulse [-] |

Echoes received from particles that lie within the measurement volume are associated with the center of that volume. The channel distance is then defined as the distance between these midpoints. Channel distance can be chosen from pre-selected multiples of the ultrasonic wavelength, while the channel width is set by selecting the number of cycles per pulse.

It is important to keep in mind that the size of the measurement volume does not depend on the channel distance, but on the number of cycles per pulse. Hence the spatial resolution increases with decreasing the number of cycles per pulse. However, the company Met-Flow suggests using a minimum of 4 cycles per pulse, because with shorter pulses, the shape of the ultrasonic beam deteriorates and echo generation becomes difficult.

By increasing the number of cycles per pulse, the channel width increases but not the channel distance. Consequently, two adjacent measurement volumes might start to overlap, as displayed in Figure 3-13b. In that case, the obtained velocity profile is smoothed, because particles in the overlapping region are associated with both neighboring channels. Overlapping can be critical for flows with strong variations in the velocity gradient.

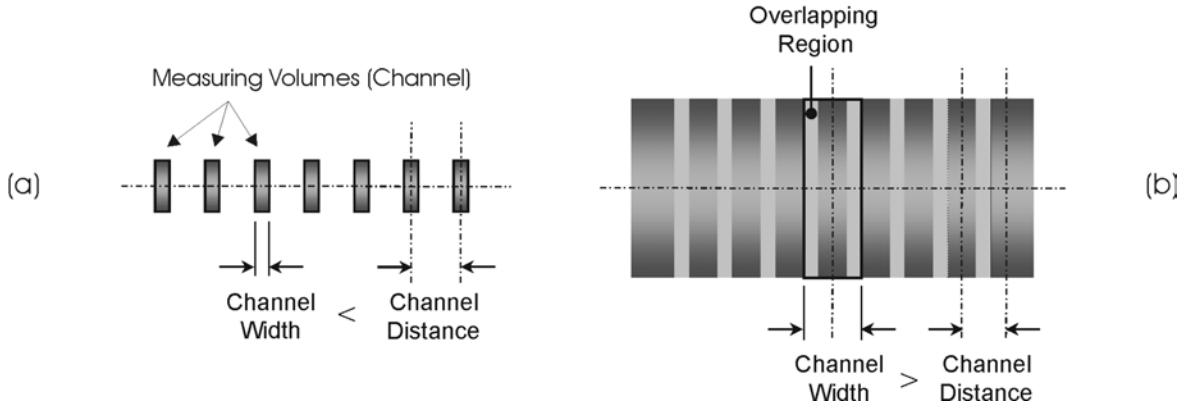


Figure 3-13: Relationship between channel width and distance. Regular (a) and overlapping (b) volumes. [19]

To avoid overlapping situations, the channel width must be set smaller than the channel distance, as shown in Figure 3-13a. When both parameters are equal, the sample volumes are adjacent to each other without overlapping. In this case all particles which enter the observed region contribute to the detected echo signal, and the obtained velocity profile covers the measurement window entirely. The latter situation should be favored.

Typical values for measurement in water ( $c = 1480$  m/s) are given in Table 3-1. Met-Flow instruments allow a selection from an even number of cycles from 2 to 32. The channel distance can be chosen from multiples of the ultrasonic wavelength.

| Cycles/Pulse [-] | Channel Width [mm]                 |                                  |                                  |                                  |                                  |
|------------------|------------------------------------|----------------------------------|----------------------------------|----------------------------------|----------------------------------|
|                  | f = 0.5 MHz<br>$\lambda = 2.96$ mm | f = 1 MHz<br>$\lambda = 1.48$ mm | f = 2 MHz<br>$\lambda = 0.74$ mm | f = 4 MHz<br>$\lambda = 0.37$ mm | f = 8 MHz<br>$\lambda = 0.19$ mm |
| 2                | 2.96                               | 1.48                             | 0.74                             | 0.37                             | 0.19                             |
| 4                | 5.92                               | 2.96                             | 1.48                             | 0.74                             | 0.38                             |
| 6                | 8.88                               | 4.44                             | 2.22                             | 1.11                             | 0.57                             |
| 8                | 11.8                               | 5.92                             | 2.96                             | 1.48                             | 0.76                             |
| 16               | 23.7                               | 11.8                             | 5.92                             | 2.96                             | 1.52                             |
| 24               | 35.5                               | 17.8                             | 8.88                             | 4.44                             | 2.28                             |
| 32               | 47.4                               | 23.7                             | 11.8                             | 5.92                             | 3.04                             |

Table 3-1: Spatial resolution, i.e., channel width, as a function of cycles per pulse and operating frequency.

---

### 3.8 Velocity Resolution

---

The velocity resolution is defined as the smallest change in velocity that can be detected by the pulse Doppler system. The velocity resolution is determined by the number of bits that are used when the detected frequency is stored for data processing and by the maximum detectable velocity. Doppler systems currently in use convert the detected frequency into an 8-digit binary number. Since each digit of a binary number can take a value of either 0 or 1, an 8-bit number can stand for one of  $2^8 = 256$  values, representing the integers from 0 to 255.

Generally, the Doppler shift detects the flow direction: a positive Doppler shift occurs when the traveling particles move toward the transducer, while a negative frequency shift occurs when the particles are receding. To indicate whether the frequency shift is positive or negative, one bit is required for sign detection. Consequently, only 7 bits are left for the velocity value. With the maximum measurable velocity given in Equation 3.13, the velocity resolution for bidirectional flow is

$$\Delta v = \frac{v_{\max}}{127} \quad (3.16)$$

where

|            |                                   |
|------------|-----------------------------------|
| $\Delta v$ | velocity resolution [m/s]         |
| $v_{\max}$ | maximum measurable velocity [m/s] |

The number 127 originates from  $2^7 = 128$  values, with 127 intervals in between. Given this, we can derive that the velocity resolution is 1/127 of the maximum measurable velocity, or 0.8 %. For practical measurement, this number holds true under the condition that the maximum velocity actually detected is equal to the maximum measurable velocity. If the detected velocity is much smaller than the measurable value, for instance, because the Doppler angle was chosen without careful consideration, the actual resolution will clearly be reduced.

With sign detection ignored, all 8 data bits are available to represent the detected frequency shift. The velocity resolution is then given by

$$\Delta v = \frac{v_{\max}}{255} \quad (3.17)$$

In truth, the velocity resolution remains unchanged, because the maximum measurable velocity  $v_{\max}$  doubles without sign detection, as indicated in Equation 3.14.

Figure 3-14 displays the difference between high and low velocity resolution. Figure 3-14a represents a sample profile obtained under the condition that the detected maximum velocity is equal to the maximum measurable value. The profile is then composed of 128 different data points. In contrast, Figure 3-14b shows a profile where the measurable velocity is ten times higher than the detected velocity maximum. The profile is composed of only 12 different data points, resulting in a poor representation of the investigated flow.

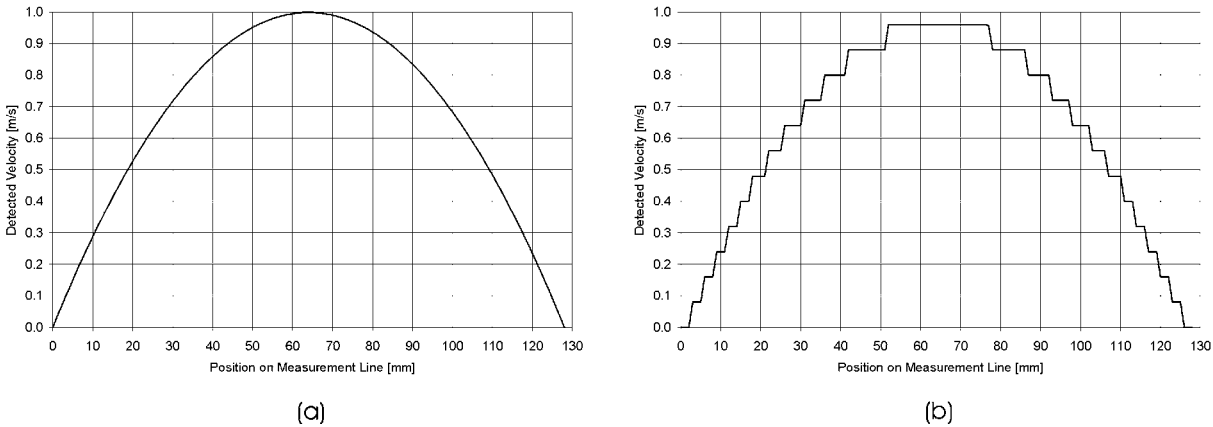


Figure 3-14: Effect of high (a) and low (b) velocity resolution.

In the latter case, the velocity resolution can be improved by altering the Doppler angle. Since the maximum measurable velocity depends on this angle, as shown in Figure 3-9 and Figure 3-10, the velocity range can be adapted to correspond to the expected maximum velocity.

### 3.9 Temporal Resolution

The temporal resolution is given by the minimum time between two measured velocity profiles. It depends on the time the system needs for data acquisition and frequency shift computation, as displayed in Figure 3-15. The temporal resolution is not influenced by the time requested for data storage and profile display, since this process can be done simultaneously.

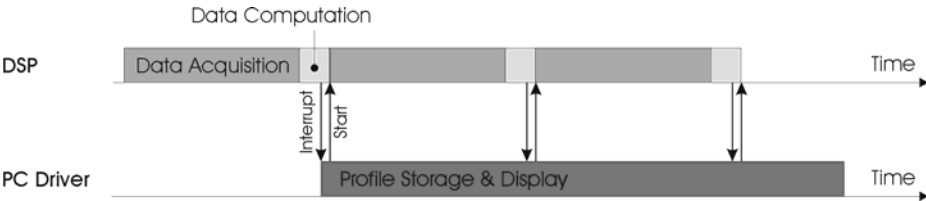


Figure 3-15: Timing of velocity profile measurements with multitasking operating system (Windows NT). [19]

Figure 3-15 shows the timing of velocity profile measurements with the UVP-Monitor model XW (Met-Flow), operating under Windows NT. Due to the multitasking capability of Windows NT, digital signal processing (DSP) remains uninfluenced by the process of profile storage and display. However, velocity profile measurements cannot be displayed in real-time. The refreshing frequency of the screen is usually lower than the frequency at which the profiles are obtained, thus some profiles are regularly skipped. Nevertheless, the profile data is not lost because the calculated values are stored in an internal buffer before the data is saved into a file.

The temporal resolution is influenced by the data acquisition time. Since the Doppler shift frequencies can be calculated from several samples only, more than one pulse transmission is necessary to obtain a velocity profile. The required time to measure a velocity profile is then controlled by the number of pulse emissions per profile. Hence the data acquisition time of one profile depends on the pulse repetition frequency and on the number of pulse repetitions used for the Doppler shift calculation.

The data processing time is very short (only a few milliseconds), and thus usually negligible compared to the time for data acquisition. Thus the temporal resolution can be approximated by the data acquisition time and is given by

$$\Delta t_{theor} \approx \frac{n_{rep}}{f_{prf}} = \frac{2 \cdot n_{rep} \cdot s_{max}}{c} \quad (3.18)$$

|       |                    |   |
|-------|--------------------|---|
| where | $\Delta t_{theor}$ | theoretical temporal resolution [s]         |
|       | $n_{rep}$          | number of pulse repetitions per profile [-] |
|       | $f_{prf}$          | pulse repetition frequency [Hz]             |
|       | $c$                | speed of sound in propagation medium [m/s]  |
|       | $s_{max}$          | measurement depth [m]                       |

The pulse repetition frequency is governed by the measurement depth, while the number of pulse repetitions is directly chosen by the operator. Consequently, high temporal resolution is obtained with short measurement depth and low numbers of repetitions per pulse.

During measurement, Met-Flow software is able to predict an average value for the temporal resolution, with a claimed accuracy of  $\pm 1$  ms. Additionally, each profile is stored with a time stamp, which helps to identify the actual time interval between two measured profiles.

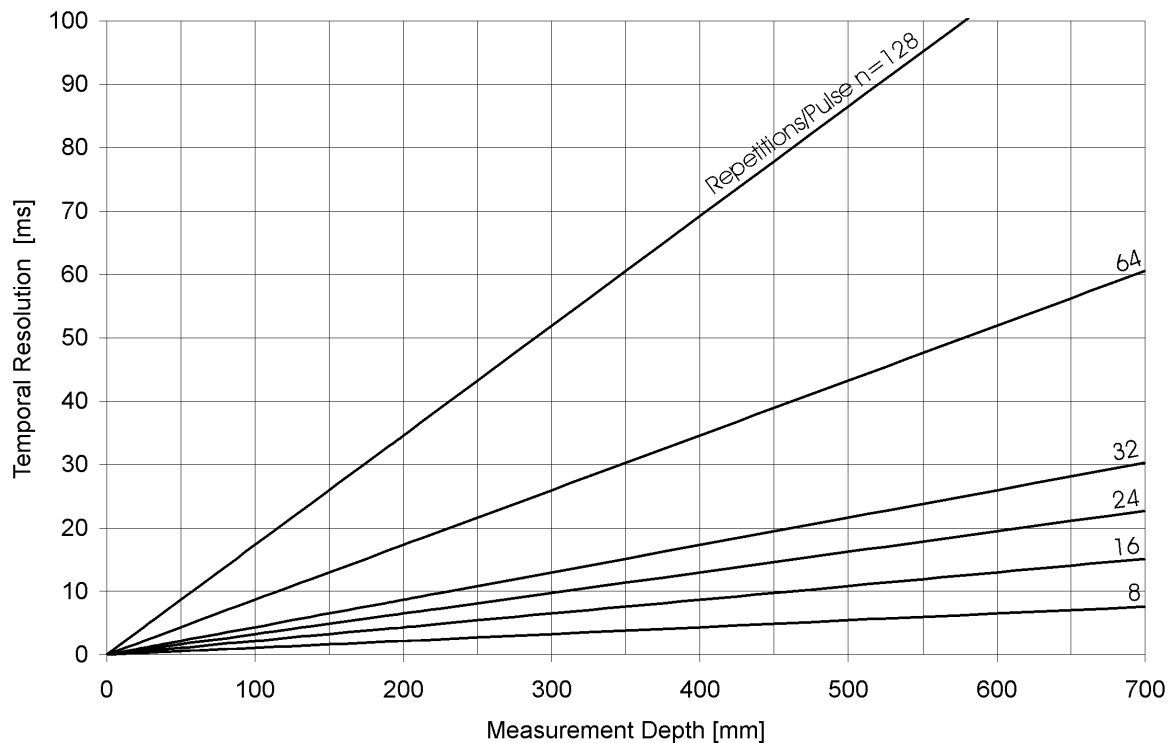


Figure 3-16: Temporal resolution as a function of measurement depth and pulse repetitions per profile.

The relationship between temporal resolution, measurement depth, and number of pulse repetitions used for Doppler shift calculation is shown in Figure 3-16. The numbers were calculated for water ( $c = 1480$  m/s). Met-Flow instruments allow a selection of the number of pulse repetitions anywhere from 8 to 128. However, with few pulse transmissions, some points of a profile may be missing when the particle concentration inside the test medium is low. Consequently, the company Met-Flow suggests 32 repetitions per pulse to obtain complete profiles during measurements.

---

### 3.10 Measurement Equipment

---

Two companies located in Lausanne, Switzerland, provide the instrumentation for ultrasonic velocity profile measurements: *Met-Flow* manufactures the UVP-Monitor series, while *Signal-Processing* fabricates the DOP velocimeter. Both companies also distribute ultrasonic transducers made by third-party manufacturers to offer a complete measurement system. From an objective point of view, the two systems differ insignificantly, and the author would like to emphasize that his considerations apply to the measurement technique in general and not to a specific device.

However, the measurement equipment that was used for this thesis came from Met-Flow, and many terms used here are related to this specific device. Figure 3-17 shows the UVP-Monitor model XW-3-PSi, which is currently in use at the Hermann-Grengg Laboratories Graz. The system consists of the main unit with integrated keyboard and display, and the ultrasonic transducers with cables. The main unit has a compact form and can easily be transported. Since all measurement parameters are set via software, the main unit does not have any controlling elements.



*Figure 3-17: UVP Monitor model XW-3-PSi. Main unit (left) and 4-MHz transducer (right). [19]*

The transducers are connected to the main unit via an integrated multiplexer at the back. Instruments with a multiplexer allow operation of up to 20 different transducers quasi-simultaneously, under the condition that all transducers work with the same frequency. Using the supplied software, the arrangement of transducer operation, the timing sequence, and many more parameter can be selected. With multiplexer mode, flow fields can be monitored in three dimensions, for example, to validate computer simulations [4]. An external multiplexer box is also available to upgrade existing systems without an integrated multiplexer.

The main unit is able to work with a set of three different operating frequencies (2/4/8 MHz). This allows greater flexibility considering the scale of the investigated models. Low frequencies are best used for large-scale applications due to the good propagation characteristics. These applications include large tanks, river models, or flumes. High operating frequencies are best used for small scale models, because they offer excellent spatial resolution. These applications include flow through pipes with small diameter or in narrow channels. Other configurations of working frequencies (1/2/4 MHz or 0.5/1/2 MHz) are available as well.

The UVP-Monitor is basically a conventional PC that operates under Windows NT. Thus it can be integrated into an existing network using a built-in Ethernet card with BNC connector. By installing software via network, the UVP-Monitor turns into a customized device. For example, an external ZIP-drive can be installed to store the obtained profile data on a separate medium. Of course, the built-in 3.5" floppy disk drive can be used as well. However, the most comfortable and quickest way to exchange measurement data is to operate the main unit in a computer network.

The actual measurement process is controlled by the supplied software. The user may modify the emitting frequency, the position of the measurement window, the size and distribution of the sample volumes, and many other parameters. These additional software parameters are explained in the User's Guide, which is provided with the UVP-Monitor. Once the measurement has finished, the obtained data can be reviewed and analyzed with separate software. For example, the flow rate can be computed for either a parallel or a circular geometry. The obtained profile data can also be imported into other applications, such as Microsoft Excel.

A sample screenshot from the online software is shown in Figure 3-18. The window is dominated by the online display of the measured data. The parameters that control the measurement can be found at the bottom and to the right of the program window.

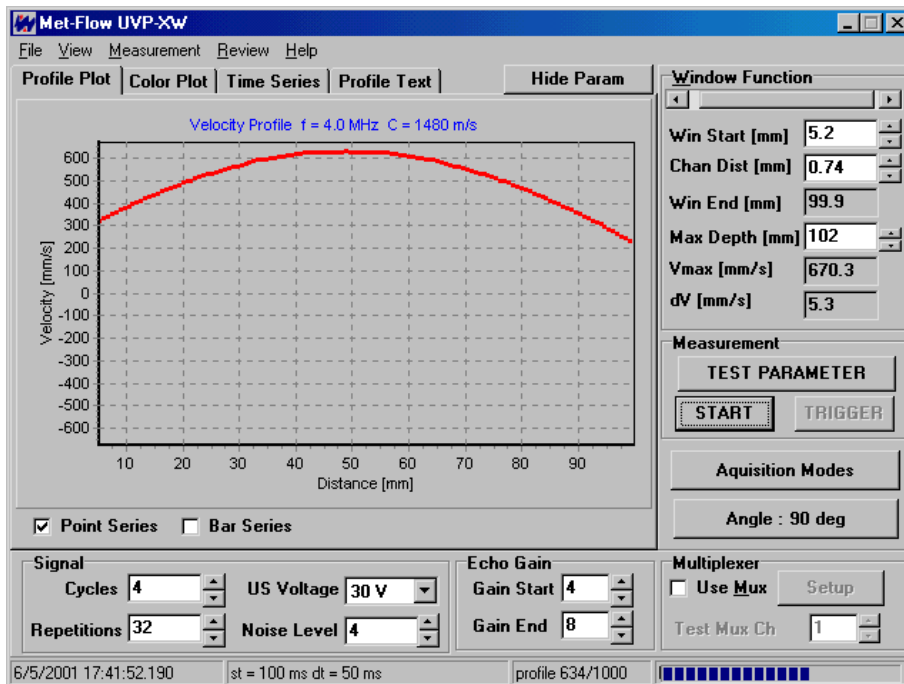


Figure 3-18: Sample screenshot of UVP-XW online software (version 2.1).



---

## 4 Investigation of Pipe Flow

---

One remarkable advantage of the ultrasound-pulse-Doppler method is the option of measuring velocity profiles non-intrusively. To test this feature and to attain practical experience in dealing with the method of ultrasonic velocity profile measurements in general, the author was given the opportunity to investigate a hydraulic scale model of an inverted siphon.

The main purpose of the experiments was to find out how pipe flow could be studied by means of velocity profile measurements. In addition, the author was expected to become familiar with the UVP-Monitor software and other computer programs in order to analyze the obtained data. This chapter presents the results of the experiments conducted, with special emphasis on providing information for future design of pipe flow studies.

The investigation of pipe flow was performed on the test model “Düker Oitenbach”. This inverted siphon model had previously been used for a hydraulic test of the flood discharge capacity of the prototype, which was designed to convey the river Oitenbach under a depressed highway. In addition, sediment transport behavior was simulated to examine if the velocity of flow in the pipes was fast enough to prevent particle deposition. The model included the inlet and outlet structures, the three pressure conduits of various diameters, and adjacent headwater and tailwater areas, as shown in Figure 4-1.

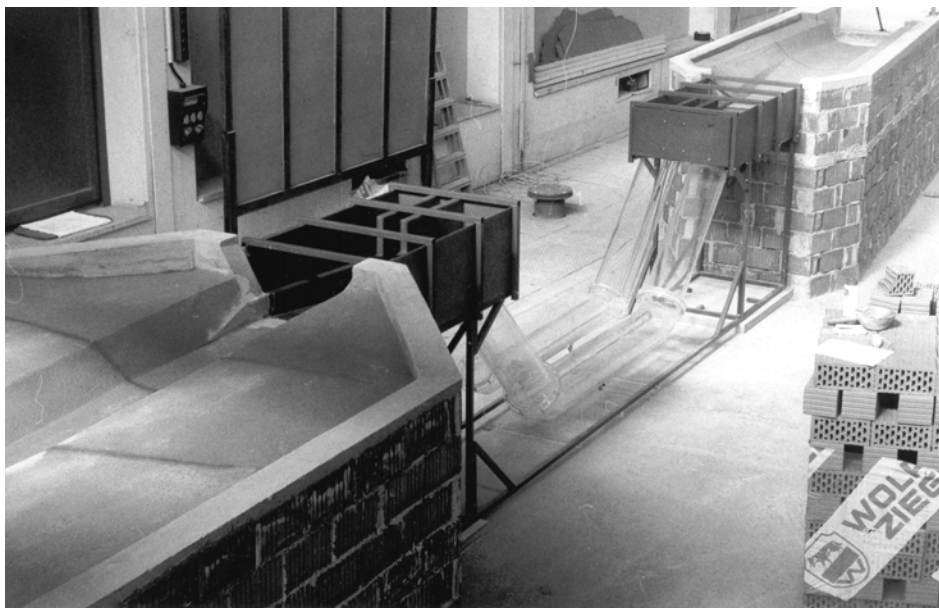


*Figure 4-1: Inverted siphon model "Düker Oitenbach" as viewed in flow direction. [10]*

---

## 4.1 General Test Setup

---

The pipes were assigned with numbers from one to three according to size, starting with the smallest pipe. The numbers are displayed in the right photograph of Figure 4-2 and are used to refer to the intended pipe. The photographs reveal that each of the three pipes has a different diameter. This special design ensures that the velocity of flow will exceed the critical velocity of sedimentation even in the case of regular discharge. In a single-pipe inverted siphon, the velocity inside the pipe would only be fast enough for high flood discharges. With a multi-pipe inverted siphon, the discharge is separated at the inlet structure according to the headwater level.

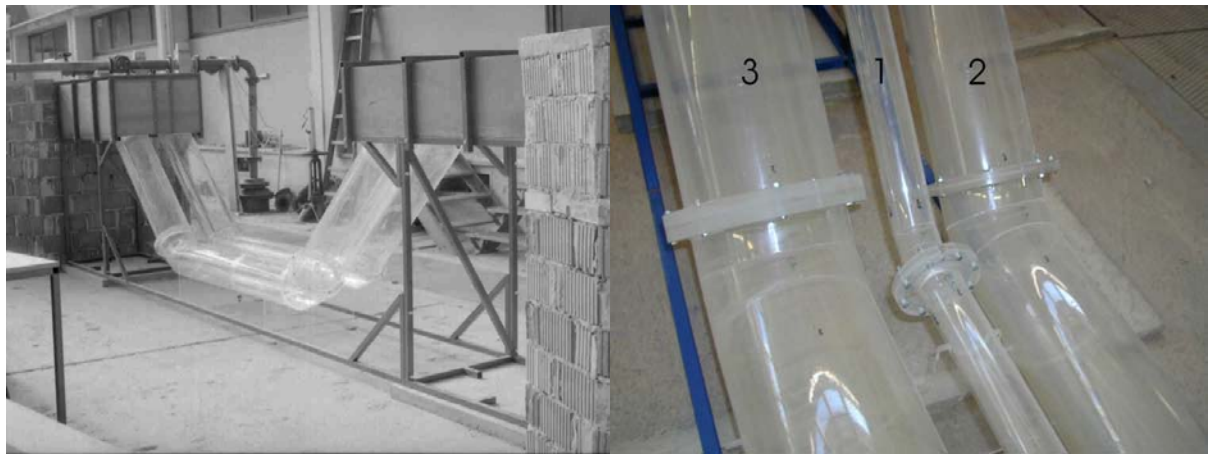


Figure 4-2: Test pipes, numbered 1 to 3 (according to size). Overview (left) and close-up of elbows (right). [10]

The pipes were manufactured from Plexiglas. Because of a practical choice of model scale (1:8.13), two of the three Plexiglas pipes were available off the rack. Only pipe 3 and the remaining elbows had to be manufactured at the laboratory workshop. Table 4-1 contains the cross-sectional dimensions of the Plexiglas test pipes. The workshop-manufactured pipe can be recognized by its larger wall thickness and by a lateral seam resulting from the manufacturing process.

| Pipe Number | Diameter [mm] |          |          | Wall Thickness [mm] |
|-------------|---------------|----------|----------|---------------------|
|             | Prototype     | Internal | External |                     |
| 1           | 500           | 62       | 70       | 4                   |
| 2           | 1400          | 172      | 180      | 4                   |
| 3           | 2000          | 246      | 256      | 5                   |

Table 4-1: Cross-sectional dimensions of the Plexiglas test pipes.

The flow conditions were investigated at various discharges to measure velocity profiles at different flows. Table 4-2 lists the expected flow rates and average velocities for the discharges that were tested. The numbers in the table below are based on the assumed flow distribution among the three pipes. This distribution was estimated in advance by the designer of the inverted siphon [12]. We see that the expected average velocities range from 0.11 m/s to 0.72 m/s. The fact that zero flow occurs in pipe 2 and 3 for small loads is explained below.

| Load Case | Total Discharge [l/s] | Pipe 1     |                | Pipe 2     |                | Pipe 3     |                |
|-----------|-----------------------|------------|----------------|------------|----------------|------------|----------------|
|           |                       | Flow [l/s] | Velocity [m/s] | Flow [l/s] | Velocity [m/s] | Flow [l/s] | Velocity [m/s] |
| MQ        | 1.06                  | 1.06       | 0.35           | -          | -              | -          | -              |
| HQ 1      | 4.24                  | 1.27       | 0.42           | 2.97       | 0.13           | -          | -              |
| HQ 10     | 15.9                  | 1.01       | 0.33           | 9.55       | 0.41           | 5.36       | 0.11           |
| HQ 30     | 26.5                  | 1.06       | 0.35           | 9.92       | 0.43           | 15.6       | 0.33           |
| HQ 100    | 50.9                  | 1.54       | 0.51           | 15.4       | 0.66           | 34.0       | 0.72           |

Table 4-2: Expected flow rates and average velocities in the inverted siphon pipes for tested discharges. [12]

Due to the special design of the intake structure of the inverted siphon (sideweir with a converging U-shaped geometry and two lateral outlets), the river discharge is separated according to the headwater level, as shown in Figure 4-3. At low discharge, water passes only through the small pipe between the two lateral sideweir outlets (left photograph). With increasing flow rate, the headwater level exceeds the lower crest of the sideweir and the water starts to flow through pipe 2 on the left bank side (right photograph). At high discharges pipe 3 on the right bank side is activated after the headwater level has exceeded the highest sideweir crest and all three pipes are active.

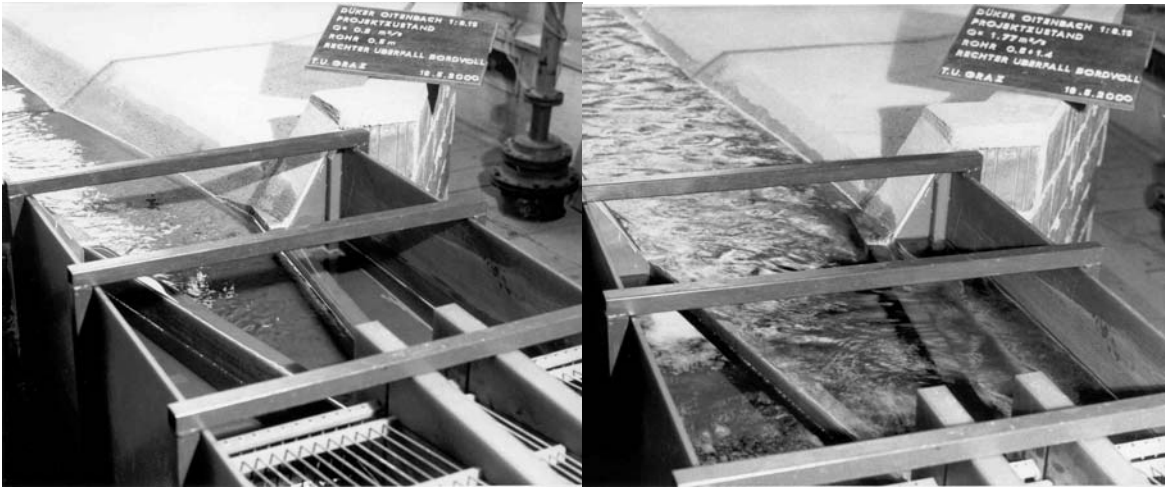


Figure 4-3: Inlet structure of the inverted siphon at low (left) and medium (right) discharge conditions. [10]

---

## 4.2 Measurement Planes

---

The desire to measure cross-sectional velocity profiles is in general hindered by the fact that the velocity of the axial flow component cannot be detected with zero angle of incidence. However, by selecting a small angle of incidence, the axial velocity can be estimated from the data obtained. In addition, with non-intrusive measurement, the loss of sound pressure to reflection has to be considered when selecting the measurement angle. As the angle of incidence increases, more sound pressure is lost at the pipe wall.

As a compromise, the flow inside the pipes was investigated by placing the ultrasonic transducer on the pipe wall at an incident angle of  $10^\circ$  from the normal, as shown in Figure 4-4a. Each of the test sections was then divided into four measurement planes, which were evenly distributed over the circumference of the pipe wall, as displayed in Figure 4-4b. This setup was inspired by the thesis of Peter Imitzer, who investigated the flow fields in a triple-distribution pipe (trifurcator) using a Laser-Doppler Anemometer (LDA) [11].

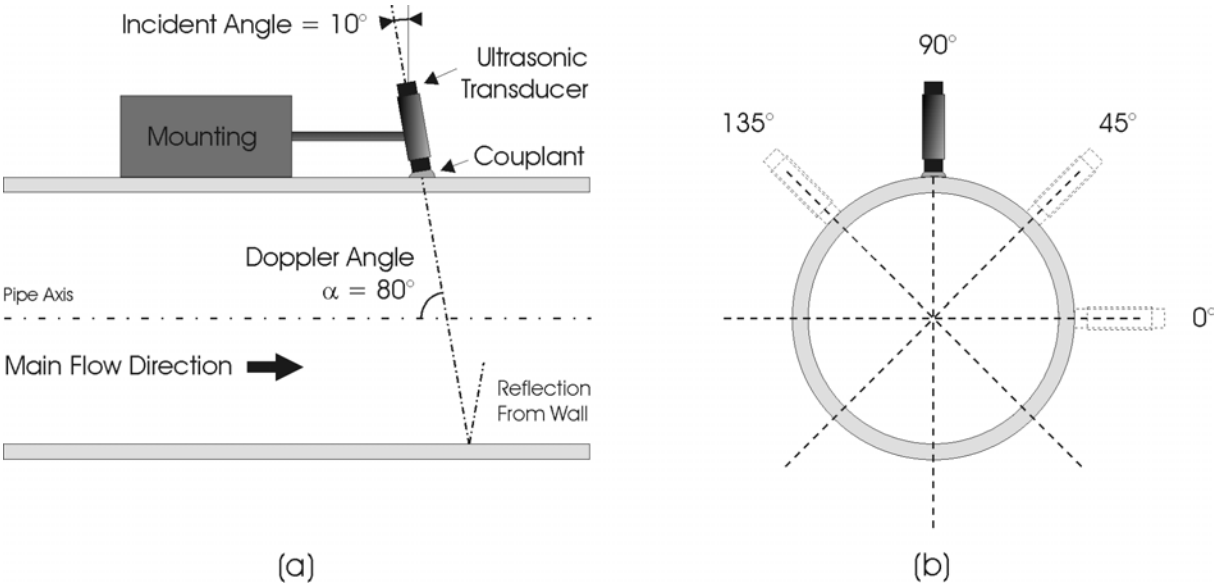


Figure 4-4: Positioning of the transducer (a) and measurement planes as viewed in the direction of flow (b).

Four measurement planes were used so that the true direction of the velocity vector at one spatial point could be reconstructed. Since we construct a three-dimensional velocity field, profile data from a minimum of three different positions is required to calculate the velocity vector at the intersection of the three profiles.

At small angles of incidence, the effect of angle uncertainty increases rapidly, as shown in Figure 3-5. Thus the accurate determination of the measurement angle is of major importance when conducting through-the-wall measurements. In our experiments, the transducer angle was precisely determined by a special mounting, which was manufactured at the laboratory workshops. As shown in Figure 4-5, the support was fixed in place with springs that were wrapped around the pipe. Because of the springs, the mounting could easily be attached and removed..



Figure 4-5: Support for fixing the transducer on the pipes.

To obtain a suitable amount of profile data, seven test sections on each pipe were investigated. The positions of the test sections along the pipes are shown in Figure 4-6. Normally the transducer was attached to the pipes facing in the direction of the flow. An exception had to be made downstream from the two elbows, where the transducer faced toward the flow because of lack space for the support.

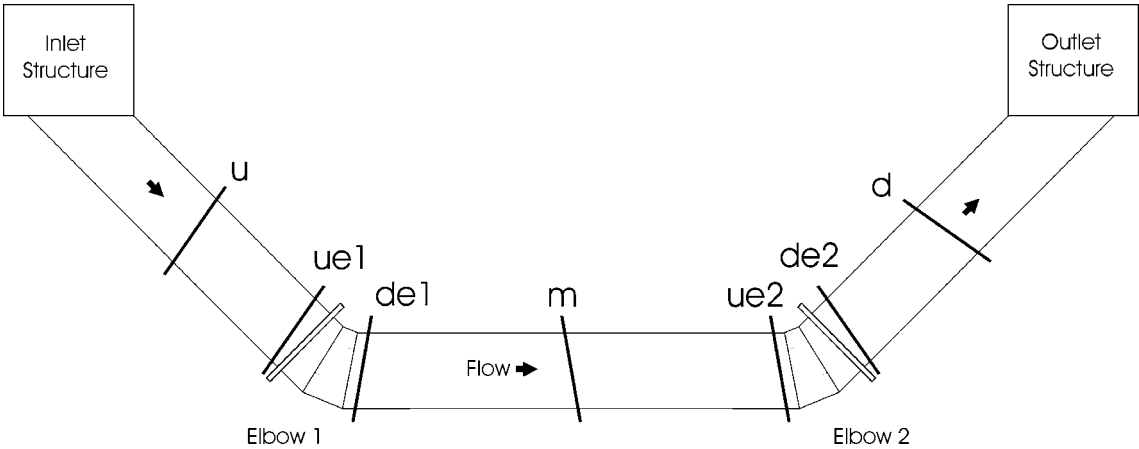


Figure 4-6: Position of test sections along the pressure pipes of the inverted siphon.

---

### 4.3 Particle Seeding

---

One constraint of the ultrasound-pulse-Doppler method is that it completely relies on echo signals from reflecting particles suspended in the test medium. The obtained measurement results are generally not satisfying if the particle concentration in the test medium is insufficient or if the particle size is too small compared to the ultrasonic wavelength. Most of the test liquids fulfill the above requirements, but sometimes it is desirable to increase the signal-to-noise ratio by adding reflecting particles to the test medium. Another possibility would be to increase the size of the measurement volume by selecting a higher number of cycles per pulse or to reduce the operating frequency of the measurement system.

In pipe flow measurement, the intensity of the ultrasonic waves is additionally reduced at the boundaries between coupling gel, pipe wall, and test medium. This property of the system makes it even more difficult to obtain complete velocity profiles at each instant. The test phase of our experiments revealed that water from the circulating system of the laboratory was not sufficiently contaminated with particles. Therefore, we decided to improve the measurement situation by seeding with heterogeneous sediment. The grain size in the sediment ranged from 0.006 mm to 1.0 mm in order to match the suggestion made by the company Met-Flow (diameter  $d \geq \lambda/4 = 0.09$  mm). The sediment was added at the inlet structure of the inverted siphon model by a sediment feeder, shown in Figure 4-7.



*Figure 4-7: Sediment feeder used for flow seeding.*

The disadvantage of the seeding process was the effect of particle sedimentation in the pipes. To avoid any disturbance on the measured velocity profiles, the stoplog gates at the inlet structure were closed during measurement breaks. After the gates were opened again, the flow velocity increased rapidly and the surge removed the deposited particles.

---

#### 4.4 Software Parameter

---

The instrumentation that was used for the pipe flow experiments was supplied by Met-Flow. The main unit UVP-Monitor XW-3-PSi was operated with a 4-MHz transducer (type TN4-5-8). The measurement process was controlled by the UVP-XW 1.0 program provided with the UVP-Monitor. After the experiments had been finished, the software was updated, and the obtained profiles were reviewed and analyzed with the program UVP-MFX 2.0. The screenshots in this thesis were taken from the latest software version (version 2.1).

Since all parameters for velocity profile measurements are manipulated via software, knowledge about the parameter settings is important to assess the obtained results. After a test phase, in which the software parameters were entered in a multitude of possible combinations, the following settings were believed to yield the best results. One fundamental parameter not listed in Table 4-3 is the speed of sound, which depends primarily on the temperature of the test medium. The water temperature was measured several times a day, and was found to remain almost constant at 20° C ( $c = 1480$  m/s).

| Test Pipe | Window Parameters |              |             |              | Signal Parameters |        |              | RF Gain   |         |
|-----------|-------------------|--------------|-------------|--------------|-------------------|--------|--------------|-----------|---------|
|           | First Ch [mm]     | Ch Dist [mm] | End Ch [mm] | Max Dep [mm] | Cyc/Pulse [-]     | NL [-] | Rep/Prof [-] | Start [-] | End [-] |
| 1         | 4.4               | 0.74         | 99.2        | 104          | 4                 | 0      | 128          | 3         | 6       |
| 2         | 4.4               | 1.48         | 193.9       | 200          | 4                 | 4      | 128          | 4         | 7       |
| 3         | 4.4               | 2.22         | 288.6       | 296          | 4                 | 2      | 128          | 5         | 7       |

*Table 4-3: Software parameters as applied to the pipe flow experiments with UVP-XW 1.0 program.*

The size of the measurement window was adjusted so as to investigate a complete velocity profile by altering the channel distance (Ch Dist). The maximum depth (Max Dep) was set to the smallest possible value. The pulse length was set to the recommended minimum of four cycles per pulse (Cyc/Pulse) to achieve high spatial resolution. Because of the excellent signal-to-noise ratio due to particle seeding, the noise level (NL) filter was set very low. The number of profile repetitions (Rep/Prof) was increased to improve the estimates of the measured velocity. The corresponding reduction of temporal resolution lead to no disadvantages, because the examined flow was sufficiently steady. The best possible settings for the time-dependent amplification of the echo signal (RF Gain) were found through trial and error.

The software parameters determined the spatial and temporal resolution of the attained profile data as well as the velocity resolution. These important parameters are summarized in Table 4-4. The numbers were calculated with the well-known formula from the third chapter, except for the temporal resolution  $\Delta t_{meas}$ , which was computed by the UVP-MFX 2.1 review program from the profile time stamps.

| Test Pipe | Measurable Velocity<br>$v_{max}$<br>[m/s] | Resolution                       |                        |  |                                       |
|-----------|---|----------------------------------|------------------------|--|---------------------------------------|
|           |   | Velocity<br>$\Delta v$<br>[mm/s] | Spatial<br>$w$<br>[mm] | Temporal<br>$\Delta t_{theor}$<br>[ms] | Temporal<br>$\Delta t_{meas}$<br>[ms] |
| 1         | 3.81                                      | 30                               | 0.74                   | 18                                     | 55                                    |
| 2         | 1.97                                      | 16                               | 0.74                   | 35                                     | 36                                    |
| 3         | 1.33                                      | 10                               | 0.74                   | 50                                     | 52                                    |

Table 4-4: Measurable velocity and resolution (temporal, spatial, velocity) for the pipe flow experiments.

The difference between theoretical and actual temporal resolution is usually caused by additional data processing time, which is required by the noise level filter algorithm. However, the measured time interval between two velocity profiles does not correspond to the settings of the noise level filter, as Table 4-4 illustrates. The most additional time was required by a noise level of zero (pipe 1), while the smallest difference between theoretical and measured resolution resulted from noise level set to four (pipe 2). An explanation for this discrepancy cannot be given. We suggest to make sample measurements in order to find out the actual temporal resolution. If the software parameters remain unaltered, a once computed resolution will apply to the subsequent measurements as well.

Another important parameter displayed in Table 4-4 is the measurable flow velocity in axial direction. At first glance, the measurable velocity is far above the expected velocity maximum of 0.72 m/s (Table 4-2), but one must consider that the expected velocity is only an averaged value based on the equation of continuity. Peak velocities in pipe 3 were expected to be much faster, and so the velocity range was almost doubled to 1.33 m/s by selecting the corresponding angle of incidence according to Figure 3-10.

An incident angle of 10° was used on all three pipes because we decided not to modify the transducer mounting during measurement. Retrospectively, it would have been better to adapt the incident angle for each pipe. The velocity range for pipe 1 and pipe 2 did not correspond appropriately to the expected flow velocities, thus the velocity resolution decreased notably.



## 4.5 Validation of Transmission Angle

The key feature of the ultrasound-pulse-Doppler method is the ability to establish a complete velocity profile along the line of measurement. Knowledge about the exact position of this measurement line is fundamental for the correct interpretation of the obtained profiles. Usually, the measurement line coincides with the transducer axis, but if the ultrasound beam is refracted at an interface, the propagation direction changes. With pipe flow measurement, the ultrasonic waves are refracted twice while passing through the pipe wall, as shown in Figure 4-8. The transmission angle  $\theta_3$  then defines the position of the measurement line inside the pipe.

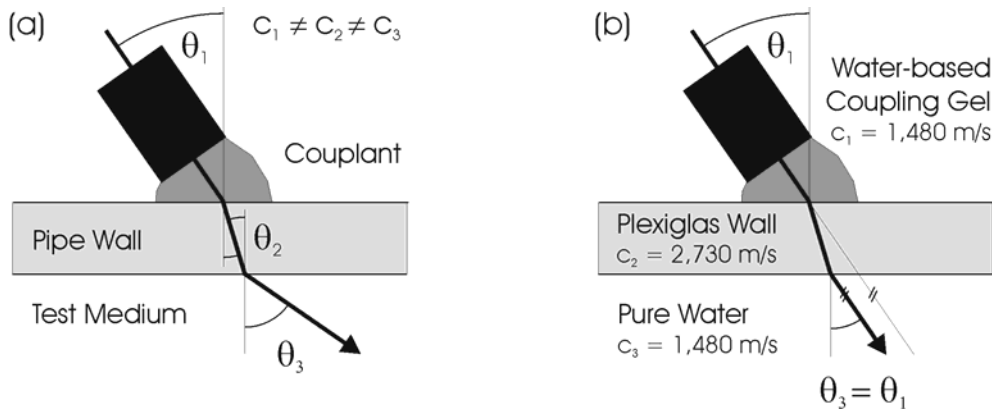


Figure 4-8: Refraction of ultrasound at the pipe wall. General case (a) and test situation (b).

With Snell's Law, the angle of transmission can be derived from the angle of incidence and the acoustic velocities in the couplant and the test medium. The transmission angle is given by

$$\theta_3 = \sin^{-1}\left(\frac{c_3}{c_1} \cdot \sin \theta_1\right) \quad (4.1)$$

where  $\theta_1, \theta_3$  angle of incidence and transmission angle  
 $c_1, c_3$  speed of sound in respective media [m/s]

Clearly, the angle of transmission becomes equal to the angle of incidence if the sound speeds in the two media are identical ( $c_1 = c_3$ ). In our experiments we used water-based coupling gel by the company Dahlhausen (Catalogue No. 93.050.00.444). Consequently, the angle of transmission was equal to the angle of incidence, and the line of measurement remained parallel to the transducer axis, as shown in Figure 4-8b.

The position of the line of measurement can usually be estimated by moving a wire across the ultrasonic beam, while monitoring the echo signals on an oscilloscope. In pipes, this method is difficult to execute. However, there is a relationship between transmission angle, line of measurement and pipe diameter, as shown in Figure 4-9a.

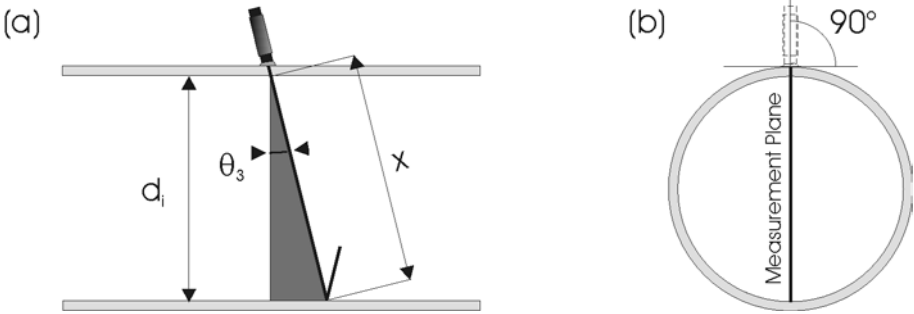


Figure 4-9: Relationship between transmission angle, measurement line and pipe diameter.

Under the condition that the distance  $x$  along the measurement line can be estimated, the transmission angle can be computed by the formula

$$\theta_3 = \cos^{-1}\left(\frac{d_i}{x}\right) \tag{4.2}$$

- where  $\theta_3$  transmission angle
- $d_i$  internal diameter of pipe [mm]
- $x$  distance between pipe walls [mm]

The above equation holds true for a lateral incident angle of  $90^\circ$ , as shown in Figure 4-9b.

In practice, the method lacks accuracy due to the limited spatial resolution of ultrasonic velocity profile measurements. Error in determining the distance between the pipe walls then leads to large alterations in transmission angle, as shown in Table 4-5. Consequently, this method is not suitable to validate the actual position of the measurement line.

| Internal Diameter $d_i$ [mm] | Number of Channels [-] | Spatial Resolution [mm] | Resulting Distance $x$ [mm] | Transmission Angle $\theta_3$ [°] |
|------------------------------|------------------------|-------------------------|-----------------------------|-----------------------------------|
| 62                           | 84                     | 0.74                    | 62.16                       | 4.1                               |
|                              | 85                     |                         | 62.90                       | 9.7                               |
|                              | 86                     |                         | 63.64                       | 13.0                              |

Table 4-5: Effect of limited spatial resolution on the determination of the transmission angle for pipe 1.

---

## 4.6 Turbulent Flow and Velocity Average

---

The method of ultrasound-pulse-Doppler is able to measure velocity profiles in a very short amount of time. However, it is recommended to investigate flow over a longer period to obtain more information about flow patterns. In turbulent flow, for instance, the detected velocity changes with time as a consequence of flow fluctuations. These fluctuations are caused by the random movement of fluid particles shown in Figure 4-10a.

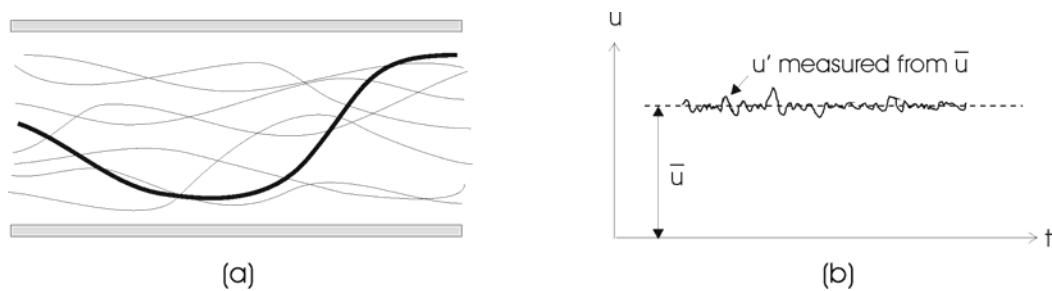


Figure 4-10: Random particle movement (a) in turbulent flow causes velocity fluctuation over time (b). [18] [24]

Turbulent flow is characterized by the fact that countless, irregular secondary components are superimposed on the principal motion of the fluid. When such flow takes place in a pipe, only the average motion of the fluid is parallel to the axis of the tube. A graph of velocity versus time at a given position in the pipe would appear as in Figure 4-10b. The measured velocity is denoted  $u = u' + \bar{u}$ , where  $\bar{u}$  indicates the mean time-averaged velocity. We observe that the instantaneous velocity is in continual fluctuation, but if the flow is steady, an average of the velocity, taken over a sufficient time interval, is constant in magnitude and direction. These mean time-averaged velocities are characteristic of the given pattern of flow.

For simplicity, we call the mean time-averaged velocity the *mean time* velocity, in contrast to the *average* velocity, computed from the equation of continuity.

The velocity profiles presented in this chapter are in fact mean time velocities, which were computed from a multitude of single velocity measurements ( $n = 1024$ ). The mean time average was calculated with the UVP-MFX review program, which offers several methods to compute average velocities. The operator can choose whether all data are included in the computation (**All**), or zero velocity remains excluded (**Zero**). He or she can include only positive (**Positive**) or only negative (**Negative**) velocities. Finally, a phase average can be calculated by selecting a specific number of cycles (**Phase**).

The decision about which kind of average is to be used should not be made thoughtlessly. A general recommendation is to exclude zero velocity by opting for the **ZERO** average. Zero velocity at a given point usually indicates that the measurement instrument was unable to establish the velocity, perhaps because of insufficient particle concentration in the measurement volume. These echo dropouts would distort the mean time average if they were included in the profile computation, as shown in Figure 4-11 and Figure 4-12. The discrepancy between **ZERO** average and **All** average diminishes for excellent echo conditions, because the instrument is then able to establish the velocity in every single point of the profile at each instant.

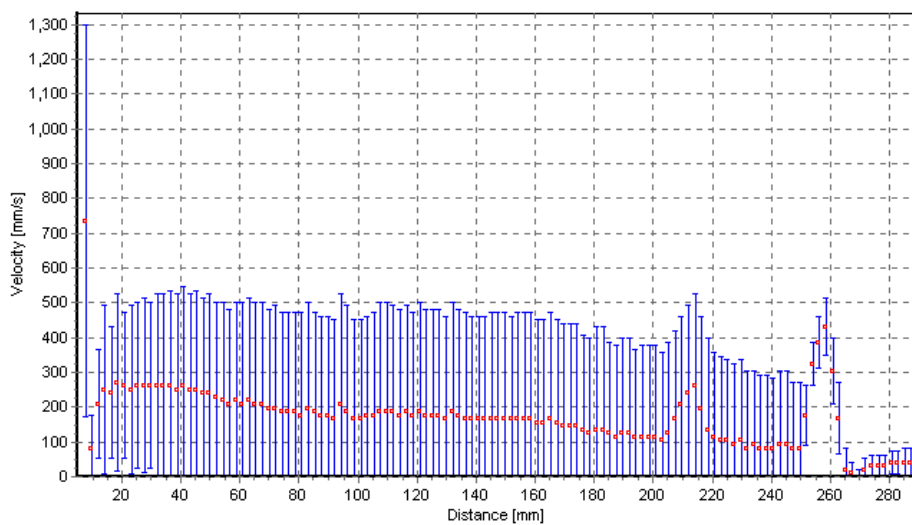


Figure 4-11: Mean time average profile computed with all velocities included (**All**).

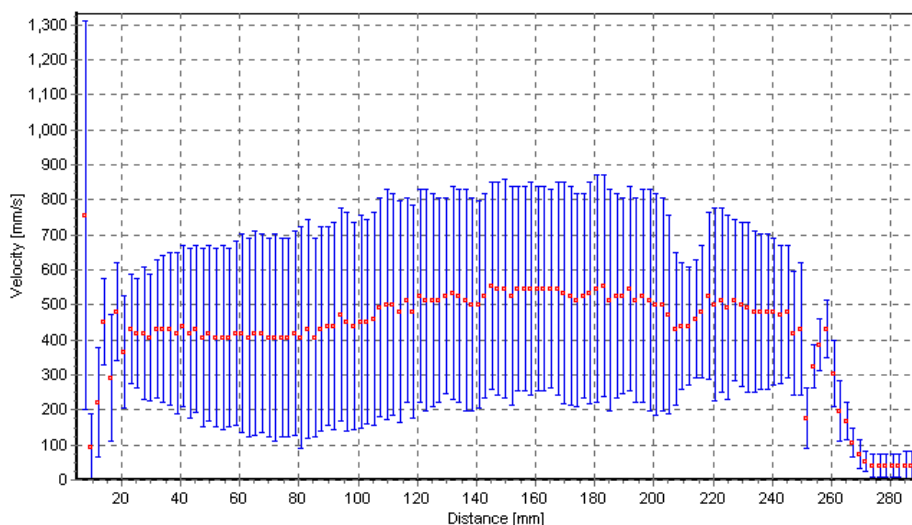


Figure 4-12: Same data, but average profile computed without zero velocities (**Zero**).

## 4.7 Analysis of Sample Profiles

It was mentioned before that each of the three test pipes was investigated at seven measurement sections, which were again divided into four measurement planes. Considering the fact that the flow inside the pipes was examined for a number of load cases, one can easily see that many measurements were conducted (in fact, more than 500). To give a representation of the obtained results, two measurement sections will be analyzed in more detail. While the first sample deals with measurement at a straight pipe, the second sample in this thesis covers the measurement that was conducted downstream from a pipe elbow.

The first section to be examined is section **m** on pipe 1, which is right in the middle of the two elbows. Although the pipe diameter is quite small (62 mm), decent velocity profiles were obtained because of the excellent spatial resolution of the 4-MHz transducer. Figure 4-13 displays a typical velocity profile measured at this section. The mean time velocities (red dots) and the standard deviation (vertical blue lines) are shown. This plot and the following plots were computed by the review software UVP-MFX 2.1 and display the velocity component along the line of measurement. In the profile below, the highest mean time velocity is approximately 110 mm/s, which is far below the maximum measurable velocity of 660 mm/s.

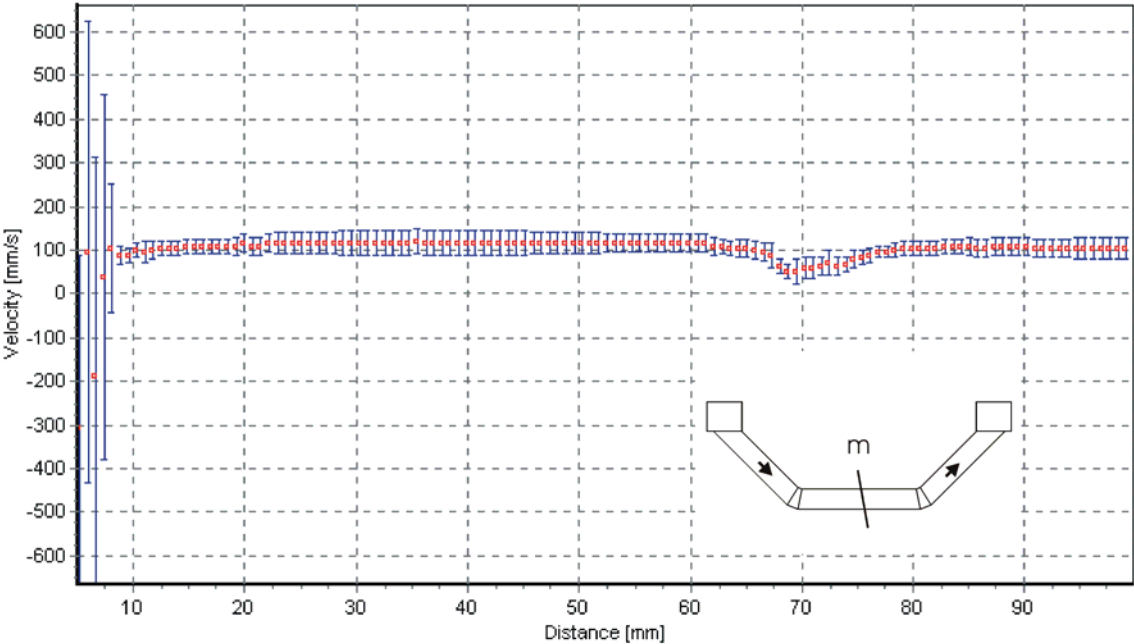


Figure 4-13: Sample velocity profile obtained at section *m* on pipe 1 showing undistorted turbulent flow.

The profile in Figure 4-13 indicates the characteristic velocity distribution for turbulent flow. The region where the velocity rises rapidly from zero to the full value found in the main stream is known as the boundary layer. Outside the boundary layer the fluid moves with the full velocity and may be considered to be practically unaffected by the reduction of velocity close to the pipe walls. The velocity gradient is highest at the pipe wall and becomes progressively smaller with increasing distance from the wall.

The decrease of flow velocity in the range of about 70 mm indicates the position of the back wall of the pipe. Beyond this distance, a mirror image of the velocity profile appears. This imaginary profile is caused by ultrasound reflection at the back wall. Since the reflected waves still propagate within the test medium, the flow velocity is detected a second time, but the depth associated to the path TRP (Figure 4-14) is then located outside the pipe.

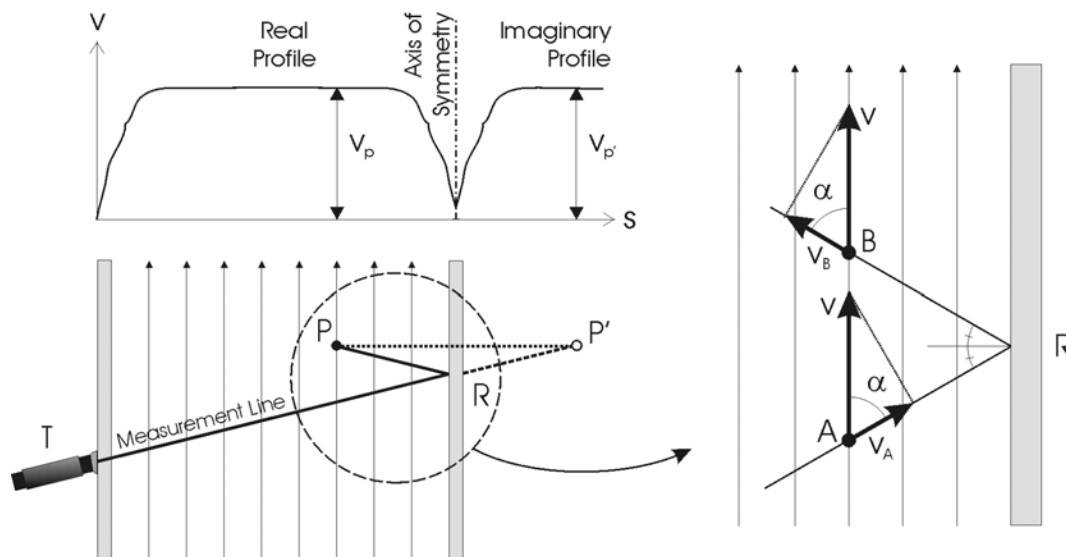


Figure 4-14: Reflection at the back wall of a straight pipe causes axial symmetry of the velocity profile.

Another interesting issue is the axial symmetry between the real part and the imaginary part of the velocity profile. This symmetry is best explained by the concept of streamlines that are usually used to depict flows graphically. Velocity vectors are drawn so as to be always tangent to the streamlines of the fluid particles in the flow. For a steady flow, the orientation of the streamlines will be fixed. Fluid particles, in this case, will proceed along paths coincident with the streamlines. Therefore we can assume that the angle between the streamlines and the measurement line is equal to the Doppler angle  $\alpha$ .

In case of flow through a straight pipe, all streamlines point in the same direction parallel to the pipe wall, as illustrated in Figure 4-14. As a result, the Doppler angle remains constant along the measurement line. Moreover, we observe that the angle  $\alpha$  does not change after the reflection at the back wall. Thus the velocity component  $v_A$  measured at A is identical to the velocity component  $v_B$  measured at B, which explains the symmetric appearance of the imaginary velocity profile. When the streamlines fail to remain parallel to the pipe wall, the symmetry between real and imaginary part of the velocity profile disappears.

The latter case is expected to happen downstream from the elbows, because the flow becomes separated from the inward bend of the pipe. Hence the second test section to be analyzed is section **de2** on pipe 3. Figure 4-15 shows a sample profile that was obtained in the vertical measurement plane of this section. Again, the mean time velocities and the standard deviation are shown. In contrast to the previous sample, the flow can neither be considered axially symmetric with respect to the pipe centerline, nor is the highest velocity found in the middle of the stream. Even the standard deviation bears little resemblance to the previous profile: the vertical blue lines have lengthened and indicate that the intensity of turbulence has increased.

Yet, the distortion of the velocity profile is explained by the distinctive shape of the flow field at the pipe elbow, which is shown in Figure 4-16.

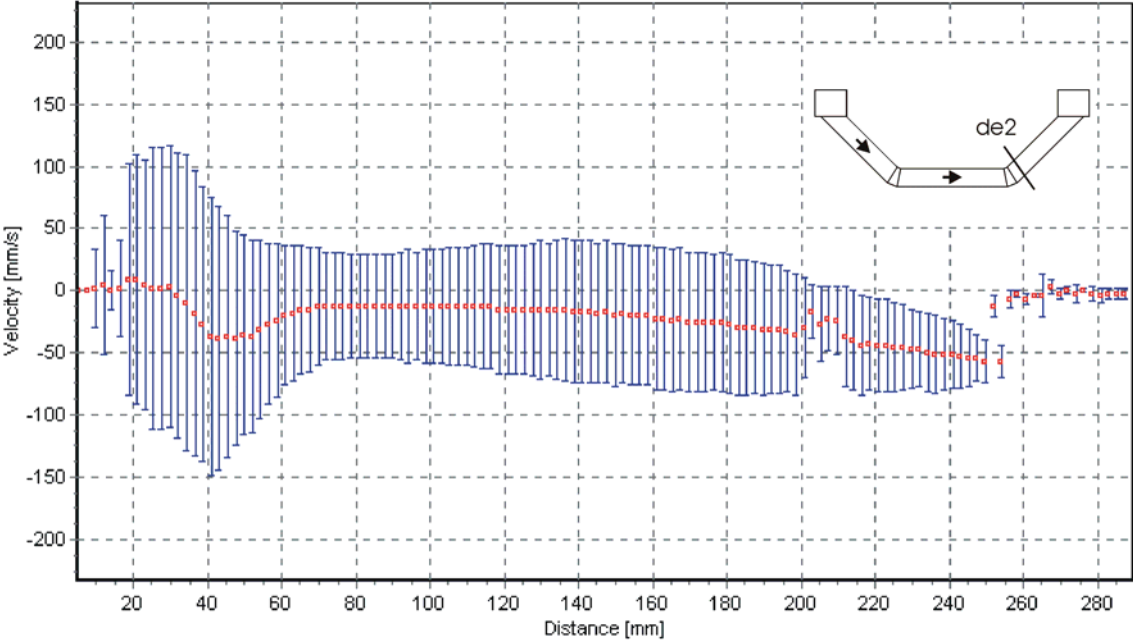


Figure 4-15: Sample velocity profile obtained at section de2 on pipe 3 showing distorted turbulent flow.

Figure 4-16 depicts a graphical representation of the flow field at the pipe elbow. As flow moves through the elbow, it accelerates around the outside of the bend and slows down near the inside of the bend. The profile is distorted with a high velocity zone occurring near the outside of the bend, as shown in Figure 4-15. The Doppler angle  $\alpha$  varies along the line of measurement due to the converging geometry of the streamlines. In the middle of the stream, flow particles typically travel perpendicular to the measurement line and fail to generate significant frequency shifts. During measurement, however, the flow direction varied so as to generate either a positive or a negative frequency shift, as indicated by the standard deviation in Figure 4-15.

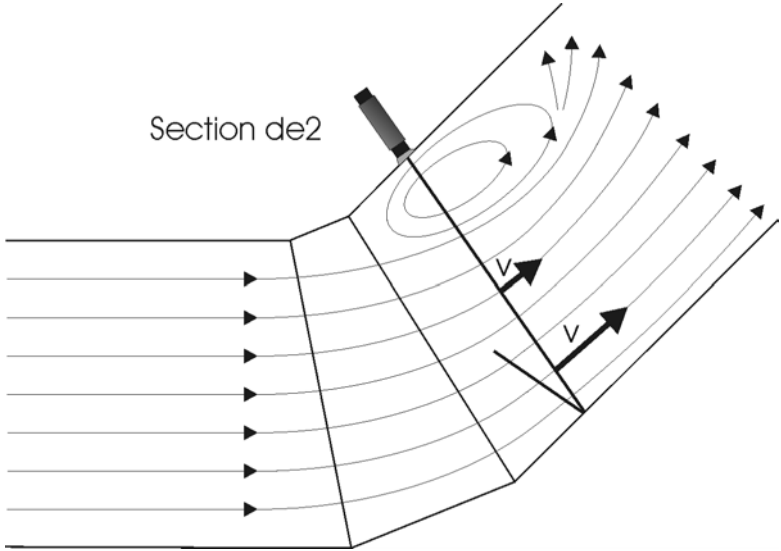


Figure 4-16: Flow pattern at the elbow showing strong eddies at the inward bend .

Irregular flow patterns are easier to identify when the obtained velocity profiles are displayed over time. This option is provided by the UVP-MFX review program with color plots. The profiles are displayed from left to right with each vertical line indicating a single velocity profile. Each sample volume is given a color that is proportional to the detected velocity. In Figure 4-17 and Figure 4-18, blue colors appear when the particles move toward the transducer while red colors appear when the particles move away. The darker the color, the faster the measured velocity. No color (white) refers to zero velocity, respectively, no echo.

The oscillating colors in Figure 4-18 are related to the varying flow direction at the elbow. The distinctively mixture of intensive colors at the bottom of the plot indicates the emergence of strong eddies at the inward bend of the pipe.



Color plots are very helpful to roughly identify the position of boundaries and whether the boundaries are fixed or not. Pipe walls, for instance, become visible within the color plot as horizontal bands of a different color. Unfortunately, ultrasound reflection may conceal the precise wall position. The white band (R) in Figure 4-17, indicating the position of the back wall in pipe 1, is approximately 8 mm in width and thus twice as wide as the real wall. This apparent enlargement is related to the fact that some of the ultrasonic wave is transmitted into the wall and reflects at the outer boundary of the pipe. Therefore the pipe wall is crossed two times, and the width of the wall apparently doubles.

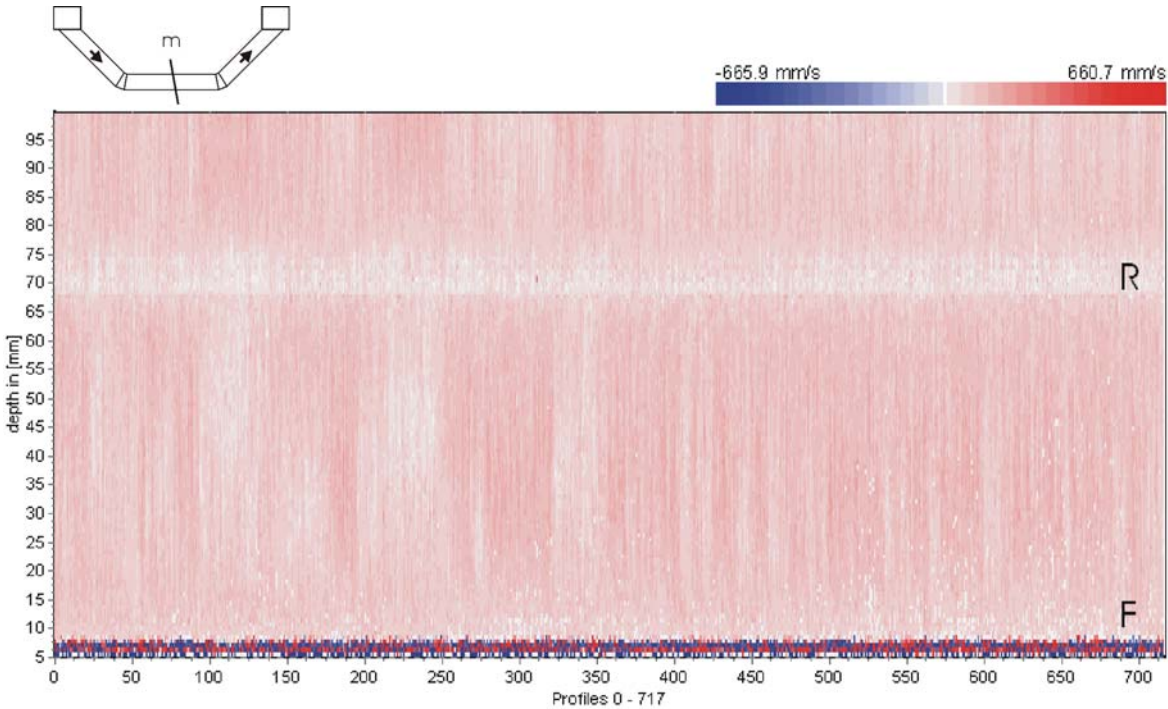


Figure 4-17: Color plot of sample profile m on pipe 1 showing velocity fluctuations (F) and rear pipe wall (R).

Figure 4-17 exposes a second horizontal band (F) at the bottom, which is characterized by a intensive mixture of red and blue colors. This specific color combination usually indicates that the flow direction varies rapidly, as in Figure 4-18, due to strong eddies. Since the band appears close to the transducer, the color fluctuations are related to the oscillating sound pressure inside the near-field zone of the transducer. In the profile plot, velocity values alter chaotically at the very beginning of the measurement window, and the standard deviation increases rapidly, as shown in Figure 4-13. Even though the influence of the oscillating sound pressure is limited to short distances, i.e., to half the near-field length ( $N/2 = 8 \text{ mm}$ ), the investigation of flow patterns close to the front pipe wall is disturbed significantly.

Figure 4-18 displays a white band (A) similar to the one in the previous color plot, but its position does not correspond to the distance between the transducer and the back wall (250 mm). At times, such artificial patterns appear during measurement and modify the shape of the velocity profile. These distortions, or *artifacts*, occur because the ultrasound reflection from the back wall interferes with subsequent ultrasonic pulses and alters their frequency. This interference pattern then appears in the measured velocity profile: in color plots, artifacts have a similar appearance to real boundaries, as Figure 4-18 illustrates, while the corresponding time-averaged profile, shown in Figure 4-13, usually indicates a region of lower velocity.

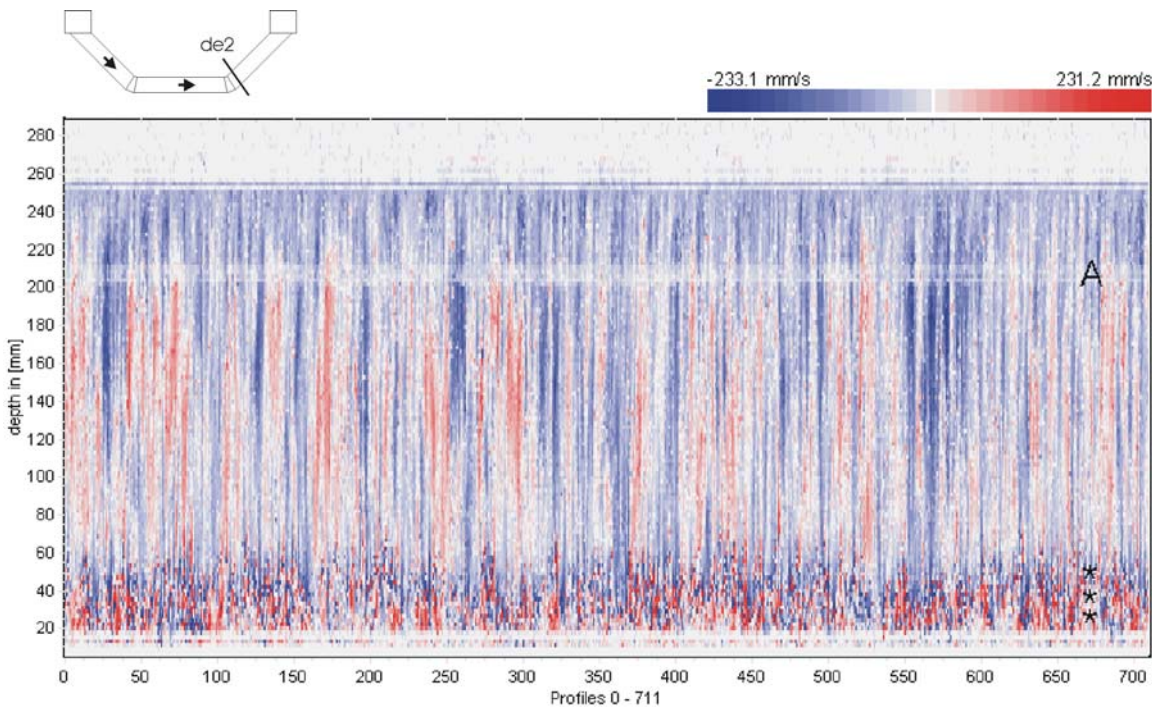


Figure 4-18: Color plot of sample profile de2 on pipe 3 showing irregular flows patterns (\*) and artifacts (A).

Currently, the profile distortions caused by ultrasound reflection cannot be eliminated by means of signal filtering [25]. Yet, the effect of boundary reflection can be undone by hand under the condition that the artifacts have been identified. A simple method for the identification of artifacts is shown in Chapter 5.

---

## 4.8 Computation of Pipe Discharge

---

It was mentioned at the beginning of this chapter that the inverted siphon model was investigated mainly to become familiar with ultrasonic velocity profile measurements. However, to make the experiments more valuable we decided to measure the flow rate in the test pipes and compare the results with the expected flow rates given in Table 4-2. To be more specific, the flow rate was computed from the obtained velocity profile data. In doing so, the author hoped to confirm the assumed flow distribution among the pipes of the inverted siphon, which was estimated by the designer of the inverted siphon.

Discharge computation by means of velocity profile measurements presents an indirect determination of flow. While direct flow measurement is made by volumetric or weight measurements, indirect flow measurement generally involves defining flow conditions and measuring one or more parameters, such as pressure or velocity.

In the case of velocity measurements, the flow rate calculation is based on the equation of continuity, which is a mathematical statement of the principle of conservation of mass. The continuity equation states that the volumetric flow rate  $Q$  is the product of average velocity  $v_{ave}$  and flow area  $A$ . Note that the flow area must be that of a plane perpendicular to the direction of flow. The flow rate in a pipe is computed by the integration of axial velocity  $v(r, \varphi)$  over the cross-sectional area of the pipe.

$$Q = \iint_{\varphi, r} v(r, \varphi) \cdot r \cdot dr \cdot d\varphi = v_{ave} \cdot A \quad (4.3)$$

|       |           |  |
|-------|-----------|--|
| where | $Q$       | volumetric flow rate [m <sup>3</sup> /s] |
|       | $v$       | mean time axial velocity [m/s]           |
|       | $r$       | local radius in the cross-section [m]    |
|       | $\varphi$ | polar angle [rad]                        |
|       | $v_{ave}$ | average axial velocity [m/s]             |
|       | $A$       | cross-sectional area [m <sup>2</sup> ]   |

Conventionally, the velocity distribution in the pipe is estimated by a relatively small number of measurement points in order to limit the time and effort put into the measurement. In ultrasonic velocity profile measurements, however, the velocity is instantly established at a multitude of measurement points.

The objective of pipe discharge determination is to deduce the total flow rate from the established velocity profile. In theory, each measurement point across the pipe has a corresponding flow area in the shape of half of a concentric ring. If the velocity in a particular annular area is considered constant, the volumetric flow rate can be determined. The total volumetric flow rate is the sum of the individual flow rates.

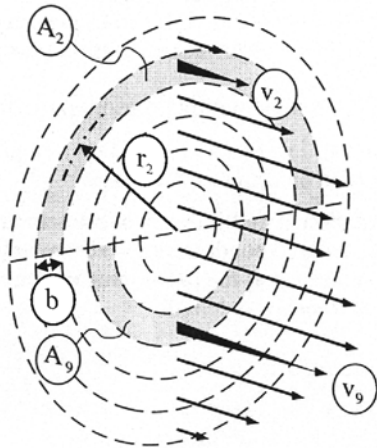


Figure 4-19: Flow rate computation by means of velocity profile measurements. [13]

An example of the procedure is illustrated in Figure 4-19. The velocity has been measured at twelve equally spaced locations across the diameter of the pipe, so the annuli remain constant in width. For each velocity measurement, the volumetric flow rate is determined based on the appropriate flow area. For example, the flow rate  $q_2$  is the product of the flow area  $A_2$  and the mean time velocity  $v_2$ . The total flow rate is the sum  $q_1$  through  $q_{12}$ .

Combining the formula for the area of an annulus with Equation 4.3 yields the total volumetric flow rate in the pipe.

$$Q = \sum q_i = \frac{1}{2} \cdot \sum (A_i v_i) = \pi \cdot b \cdot \sum (r_i \cdot v_i) \tag{4.4}$$

|       |       |  |
|-------|-------|--|
| where | $Q$   | total volumetric flow rate [m <sup>3</sup> /s]   |
|       | $q_i$ | individual annular flow rate [m <sup>3</sup> /s] |
|       | $A_i$ | individual area of annulus [m <sup>2</sup> ]     |
|       | $b$   | width of annuli (constant) [m]                   |
|       | $r_i$ | individual radius of annulus [m]                 |
|       | $v_i$ | individual mean time axial velocity [m/s]        |

The equation holds true for profiles measured in a plane perpendicular to the flow direction.

Ultrasonic velocity profile measurements, however, involve an angle  $\alpha < 90^\circ$  between the measurement plane and the flow direction. Flow rate computation then requires the determination of the velocity vector  $v_i$  perpendicular to the measurement plane. If we assume that the direction of flow is parallel to the pipe axis, the velocity vector  $v_i$  is computed from the detected vector  $v_a$  using the tangent of the Doppler angle  $\alpha$ , as indicated in Figure 4-20a.

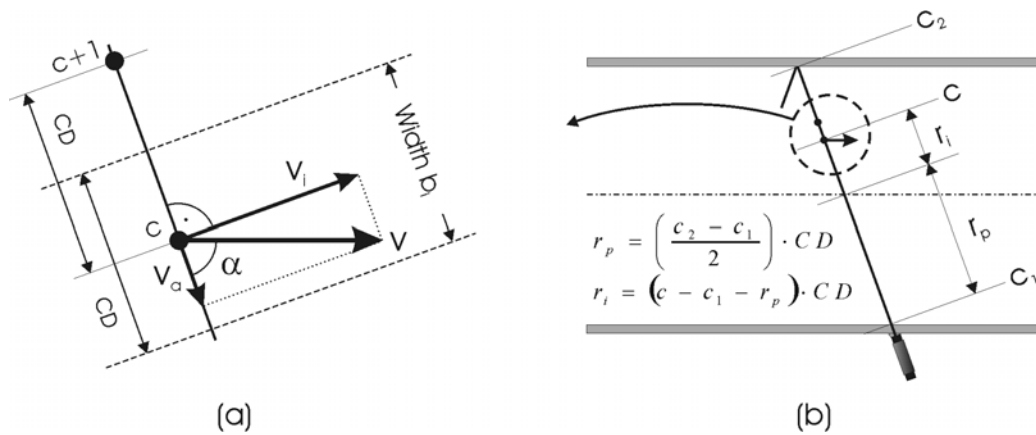


Figure 4-20: Computation of pipe discharge as implemented in the in UVP-MFX review program.

In order to calculate the pipe discharge correctly, we have to specify the flow boundaries. The boundaries are defined by selecting the appropriate channels within the measurement window, as shown in Figure 4-20b. The width  $b_i$  of the individual flow areas is determined by the channel distance and not the channel width.

Pipe discharge is given by the formula

$$Q = \pi \cdot \tan \alpha \cdot CD^2 \cdot \sum_{c=c_1}^{c_2} \left( \left| c - \frac{c_1 + c_2}{2} \right| \cdot v_c \right) \quad (4.5)$$

|       |            |   |
|-------|------------|---|
| where | $Q$        | pipe discharge [mm <sup>3</sup> /s]               |
|       | $\alpha$   | Doppler angle                                     |
|       | $CD$       | channel distance [mm]                             |
|       | $c_1, c_2$ | first and last channel representing pipe flow [-] |
|       | $v_c$      | velocity measured in channel c [mm/s]             |

The equation above is used in the UVP-MFX review program. The software calculates the flow rate for every profile obtained during measurement and displays the flow rate over time. Unfortunately, the program cannot compute the time-averaged flow rate.

An advantageous approach to computing the time-averaged flow rate is to make use of the mean time velocity profiles that are generated by the UVP-MFX program. With this method it is possible to edit the velocity profiles before the flow rate is calculated in order to undo any distortions caused by ultrasound reflection (artifacts). We suggest to establish the entire flow rate computation in Microsoft Excel or similar programs using customized worksheets. These programs also allow the display of several velocity profiles in one diagram to compare velocity profiles that have been measured, for instance, in different measurement planes

The flow rate computation for the pipes of the inverted siphon was based on the original velocity profile measurements (no data post-processing). The mean time velocity profiles were generated in the UVP-MFX review program using the **Zero Average** option. After the profile data were saved as text-files (ASCII), they were transferred into Microsoft Excel where the data were displayed in diagrams and the flow rate was computed (Doppler angle = 80°). The profiles that were measured by moving the transducer around the pipe (0°, 45°, 90° and 135°) were combined so as to contribute equally (25 percent) to the flow rate of a single test section.

To evaluate the quality of the measurements made, the pipe flow was investigated at known discharges. These calibration measurements were made while two of the three stoplog gates at the inlet structure of the inverted siphon model were closed and the total discharge passed through the remaining pipe. Table 4-6 illustrates the relative errors in the subsequent flow rate computation achieved at section m. Apart from pipe 1, the discrepancy between the given discharge  $Q$  and the computed flow rate  $Q_{UVP}$  is pretty high, the maximum being 32 percent.

| Load Case | Q [l/s] | Pipe 1                 |                 | Pipe 2                 |                 | Pipe 3                 |                 |
|-----------|---------|------------------------|-----------------|------------------------|-----------------|------------------------|-----------------|
|           |         | Q <sub>UVP</sub> [l/s] | Discrepancy [%] | Q <sub>UVP</sub> [l/s] | Discrepancy [%] | Q <sub>UVP</sub> [l/s] | Discrepancy [%] |
| MQ        | 1.06    | 1.08                   | 1.9             | -                      | -               | -                      | -               |
| HQ 1      | 4.24    | -                      | -               | 3.66                   | 13.7            | -                      | -               |
| HQ 10     | 15.9    | -                      | -               | 11.6                   | 27.2            | 13.0                   | 18.2            |
| HQ 30     | 26.5    | -                      | -               | -                      | -               | 18.0                   | 32.2            |

Table 4-6: Relative errors in the flow rate computation at section m showing poor agreement for pipe 2 and 3.

The flow rate computation for pipe 2 and pipe 3 is found to be affected by the elbow located upstream from the test section. Flow leaving the elbow is distorted and returns to an undistorted velocity profile after a certain pipe length (6 to 10 times the pipe diameter  $d$  [26]). If the test section is located within that zone, the computation of the flow rate is likely to be incorrect. The velocity profiles shown in Figure 4-21 were measured on pipe 1 ( $d = 62$  mm) where

the flow rate was established correctly. In contrast, the profiles displayed in Figure 4-22 caused the highest error in the computation of the flow rate. The profiles were measured on pipe 3 ( $d = 246$  mm) where, considering the larger diameter of the pipe, the test section was located too close to the pipe elbow.

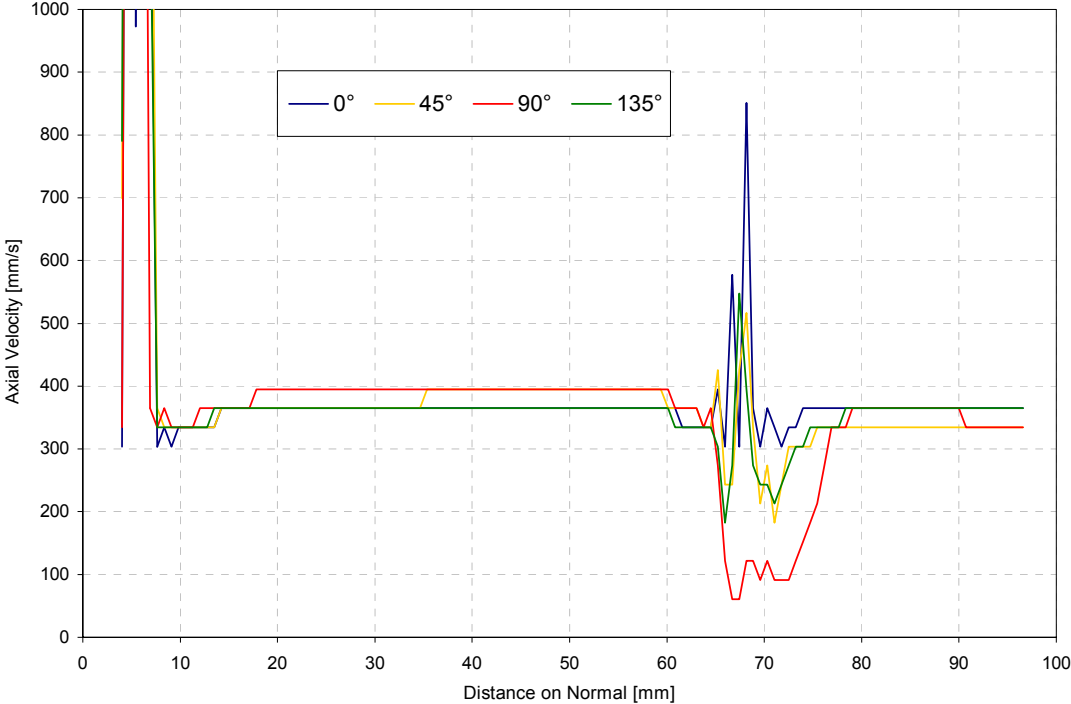


Figure 4-21: Velocity profiles obtained at section m on pipe 1 showing undistorted flow.



Figure 4-22: Velocity profiles obtained at section m on pipe 3 showing distorted flow.

---

## 4.9 Summary

---

Pipe flow was investigated non-intrusively using the UVP-Monitor model XW-3-PSi. For practical reasons, the investigations were conducted on a hydraulic model of an inverted siphon. The model included three Plexiglas pipes from 62 mm to 246 mm in diameter on which the measurements were performed. The ultrasonic transducer was placed on the pipe wall at an angle of  $10^\circ$  from normal. Water-based coupling gel was applied between the wall and the transducer. In theory, the angle of transmission through the pipe wall is then equal to the angle of incidence. A method was developed to confirm this finding but lacks accuracy due to the limited spatial resolution of the ultrasound-pulse-Doppler technique.

Each test pipe was investigated at seven measurement sections, which were divided into four measurement planes by moving the transducer around the pipe. Velocity profiles were measured in each measurement plane over a sufficient time interval (20 to 50 seconds) to obtain characteristic information about the turbulent flow studied. The profile data were then time-averaged using the UVP-Monitor software. In order to compensate for the loss of ultrasound energy at the pipe wall, the particle concentration within the flow had to be increased by seeding with sediment. Despite high SNR (signal-to-noise ratio), multiple ultrasound reflections between the pipe walls were found to affect the measurements.

Two representative measurement sections were analyzed in more detail: the first located within a straight pipe, the second situated downstream from an elbow. The time-averaged velocity profiles and the respective standard deviations are shown. The concept of streamlines was used to explain the formation of the velocity profiles, thereby illustrating the correlation between the flow fields investigated and the velocities obtained. A display of the profile data over time using color plots provided by the UVP-Monitor software is also included. These plots were found to be very useful in identifying the position of boundaries as well as interference patterns caused by ultrasound reflections.

The investigation of pipe flow was completed by the computation of the flow rate from the velocity profiles obtained. The flow rate computation was based on the determination of individual flow rates for each measurement point across the pipe. The formula given requires that the flow direction is parallel to the pipe centerline. For that reason the flow rate was found to be incorrect when the velocity profiles were measured downstream from pipe elbows or similar disturbances of the piping geometry where flow was found to be distorted.



---

## 5 Study of Open Channel Flow

---

Open channel flow, frequently encountered in hydraulic engineering, is characterized by the existence of a free surface. In contrast to pipe flow, this constitutes a boundary at which the pressure is atmospheric, and across which the shear forces are negligible. As a result, the conditions controlling the flow are different from those governing flow that is entirely enclosed. The concepts relating to flow in open channels are certainly the most complex ones in the science of hydraulics because of the unknown geometry of the free surface.

Flow in an open channel, like that in a pipe, may either be laminar or turbulent. However, laminar flow in open channels seldom occurs in cases of practical interest. For this reason, completely turbulent flow may invariably be assumed. The surface of a flowing liquid occasionally may appear smooth and glassy, but that is no indication that turbulent flow does not exist underneath. The type of flow most easily treated analytically is *steady uniform* flow, in which the depth of the liquid changes neither with distance along the channel nor with time. In practice *non-uniform*, or *varied*, flow is found more frequently.

The actual velocity distribution in an open channel is influenced both by the solid boundaries and by the free surface. The irregularities in the boundaries of open channels are usually so large, and occur in such a random manner, that each channel has its own peculiar pattern of velocity distribution. Nevertheless, it may be said that the maximum velocity usually occurs at a point slightly below the free surface (from 0.05 to 0.25 times the full depth) [18]. A typical velocity pattern for a narrow channel of rectangular cross-section is shown in Figure 5-1.

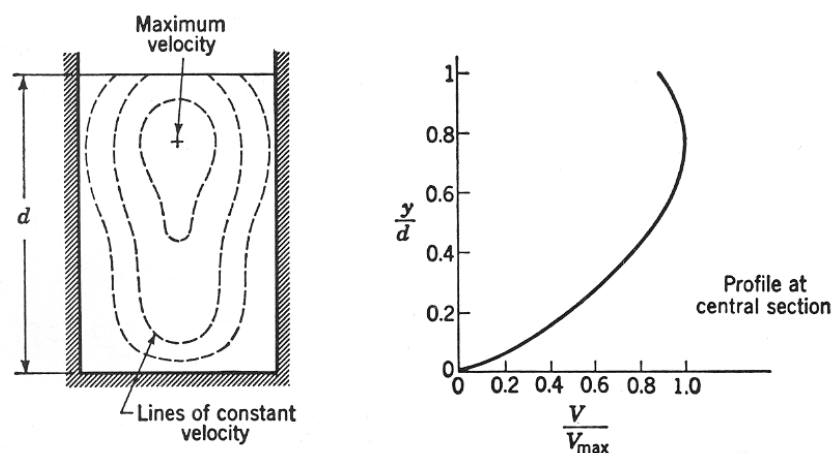


Figure 5-1: Contours of constant velocity (left) and velocity profile (right) for flow in narrow channels. [24]

---

## 5.1 Test Facilities

---

The test facilities are shown in Figure 5-2. The experiments were performed in a horizontal channel about 10 m long, 30 cm wide, and 80 cm high. The bottom of the channel was made from steel, while the sides were manufactured from glass. Water from the overhead reservoir of the laboratory entered the channel through the pipe system. The inflow was adjusted by a control valve, while the depth of the water was varied using a slide gate at the downstream end of the channel. Because of its short length, non-uniform flow was expected in the channel.



*Figure 5-2: Test facilities for employing the UVP-Monitor in the study of open channel flow.*

---

## 5.2 Measurement of Velocity Profiles

---

The movement of the free surface may affect the experimental study of open channel flow by means of ultrasonic velocity profile measurement [20][25]. The experiments described in this section were conducted to investigate the reported influence of surface movement. For the generation of wavy flow, an overflow structure was built across the upstream end of the channel. The structure produced waves with a small amplitude at the downstream end of the channel where the test section was positioned. The transducer was inserted from above the surface of the water facing the direction of flow, as shown in Figure 5-3. The axis of the transducer was placed at two different angles to the surface to test the effect of angle variation.

In order to validate the obtained velocity profiles, a Höntzsch current meter with a four-vane propeller of 18-mm diameter was used as well. Time-averaged velocity measurements were taken at 4.5-cm intervals along a vertical line, starting at the bottom of the test channel.

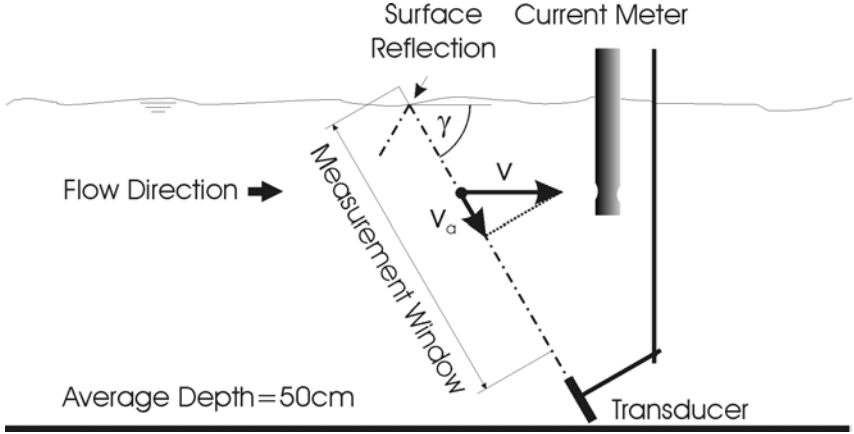


Figure 5-3: Experimental setup for velocity profile measurements in wavy flow.

The UVP-Monitor model XW-3-PSi was operated with the same 4-MHz transducer as in the pipe flow experiments (type TN4-5-8). Table 5-1 presents the measurement parameters as applied to the experiments. The water temperature was found to remain constant at 15°C, thus the speed of sound was set to  $c = 1466 \text{ m/s}$  according to Figure 2-1.

| Angle<br>$\gamma$<br>[°] | Window Parameters |                 |                |                 | Signal Parameters |           |                 | RF Gain      |            |
|--------------------------|-------------------|-----------------|----------------|-----------------|-------------------|-----------|-----------------|--------------|------------|
|                          | First Ch<br>[mm]  | Ch Dist<br>[mm] | End Ch<br>[mm] | Max Dep<br>[mm] | Cyc/Pulse<br>[-]  | NL<br>[-] | Rep/Prof<br>[-] | Start<br>[-] | End<br>[-] |
| 75                       | 5.1               | 3.66            | 474.3          | 497             | 10                | 0         | 64              | 7            | 7          |
| 60                       | 38.8              | 3.66            | 508.0          | 534             | 10                | 0         | 64              | 7            | 7          |

Table 5-1: Software parameters as applied to the free-surface flow experiments with UVP-XW 2.0 program.

Apart from the window parameters, identical software settings were used for both angles. The position of the measurement window was specified so as to cover the entire flow (End Ch). The pulse length was set to ten cycles per pulse (Cyc/Pulse) to ensure that the sample volumes were adjacent to each other without overlapping as described in Section 3.7. The noise level filter (NL) was turned off. The number of profile repetitions (Rep/Prof) was increased to improve the estimates of the measured velocity. The settings for the time-dependent amplification of the echo signal (RF Gain) were recommended by the company Met-Flow for measurements in water.

The measurable velocity and other parameters are given in Table 5-2. The theoretical temporal resolution practically matches with the resolution computed from the actual time stamps.

| Angle<br>$\gamma$<br>[°] | Measurable<br>Velocity<br>$v_{\max}$<br>[m/s] | Resolution                       |                        |   |  |
|--------------------------|---|----------------------------------|------------------------|---|--|
|                          |   | Velocity<br>$\Delta v$<br>[mm/s] | Spatial<br>$w$<br>[mm] | Temporal<br>$\Delta t_{\text{theor}}$<br>[ms] | Temporal<br>$\Delta t_{\text{meas}}$<br>[ms] |
| 75                       | 0.52  | 4                                | 3.66                   | 43  | 44   |
| 60                       | 0.25  | 2                                | 3.66                   | 47  | 48   |

Table 5-2: Measurable velocity and resolution (temporal, spatial, velocity) for the free-surface flow experiments.

The results of the experiments are displayed in Figure 5-4. The diagram compares the velocity profiles obtained by the UVP-Monitor with the measurements made by the current meter. The time-averaged velocity profiles were smoothed using a floating average computation.

For the most part, the velocity profiles are found to be in good agreement with the samples from the current meter. However, the closer the measurements are to the bottom of the channel, the less the data corresponds, which is caused by disturbances in flow near the ultrasonic transducer. The reported influence of ultrasound reflection from the free surface shows in a number of significant velocity drops. Severe distortions appear at 50 mm, 250 mm and 330 mm (UVP 60°), and at 40 mm and 300 mm (UVP 75°).

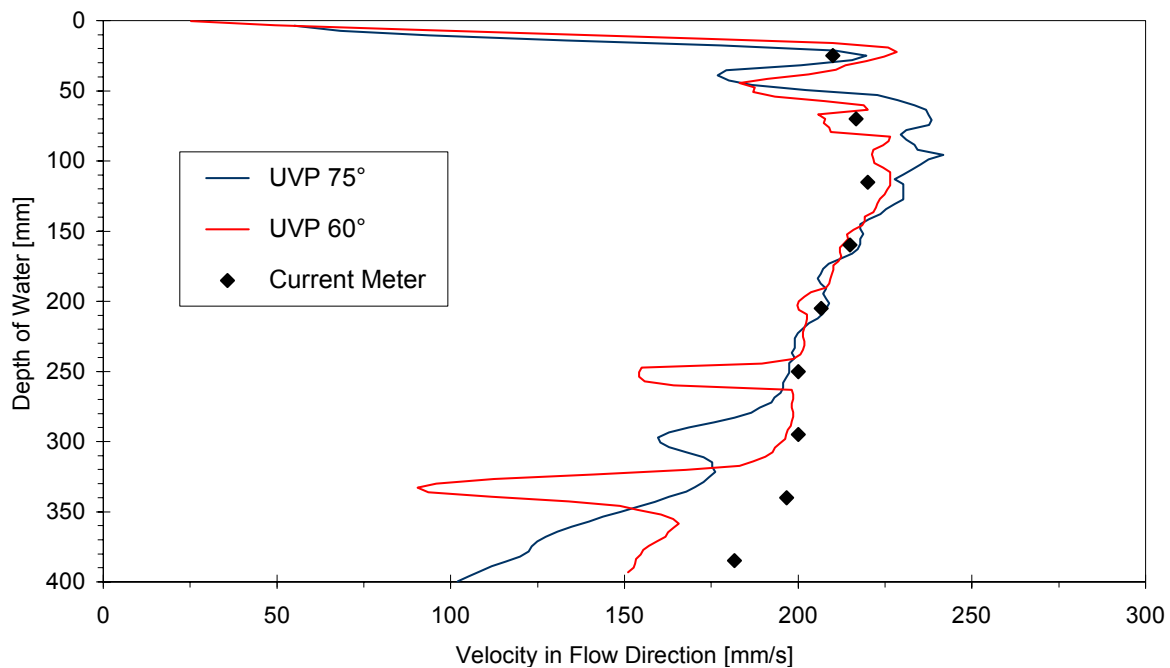


Figure 5-4: Comparative diagram showing velocity profiles obtained by UVP-Monitor and current meter.

---

### 5.3 Identification of Artifacts

---

It has been previously shown that profile distortions caused by ultrasound reflection (*artifacts*) might be mistaken for flow boundaries. As more than one artifact hardly ever occurred in the pipe flow experiments, the identification of the genuine boundary was quite simple. The investigation of open channel flow, however, was characterized by the regular appearance of numerous profile distortions, as shown in Figure 5-5. Consequently, we developed a simple yet unmistakable method for the instant identification of these artifacts.

Profile distortions occur because the ultrasound reflection from the free surface (or the back wall of the pipe) interferes with subsequent ultrasonic pulses. Thus the time interval between the pulse emissions determines the location of the interference, i.e., the depth at which the profiles are modified. If this time interval is altered by selecting a different maximum depth, some artifacts will change their position inside the measurement window. This apparent movement, best viewed within color plots, is a distinguishing feature of profile distortions caused by ultrasound reflection.

Figure 5-5 shows a comparative color plot of five UVP 75° test measurements. Apart from the maximum depth  $P_{max}$ , the measurement parameters remain unchanged. Some artifacts move toward the transducer as the measurement depth increases and can be identified easily.

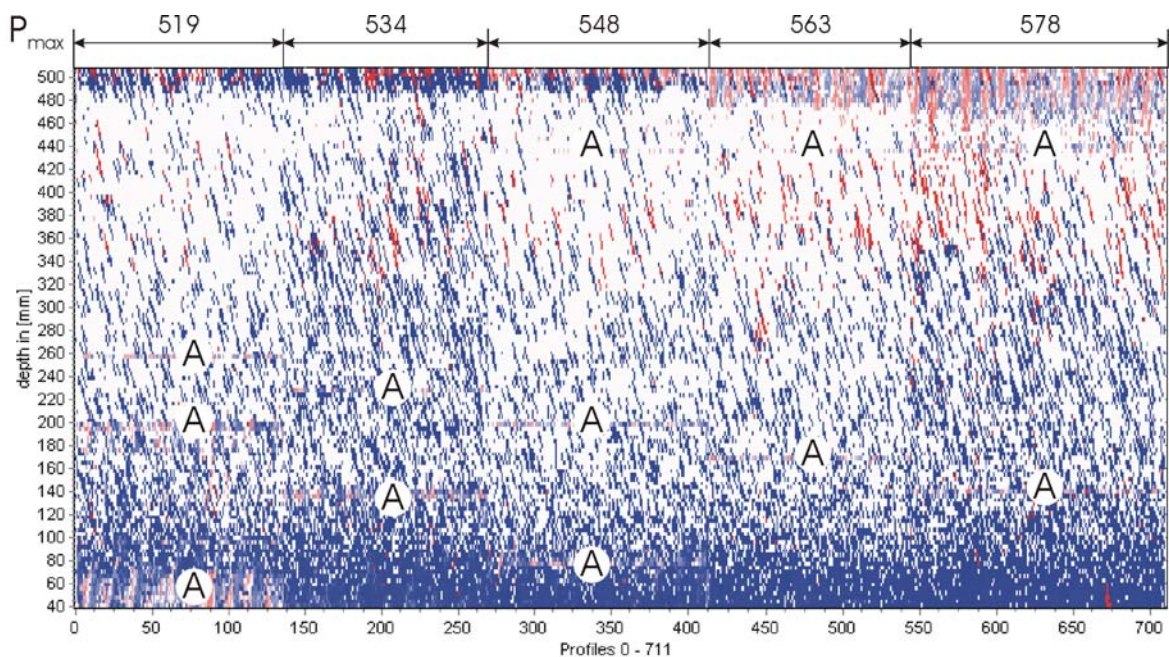


Figure 5-5: Comparative color plot showing apparent movement of artifacts (A) for different maximum depths.

---

## 5.4 Surface Level Measurement

---

For flow in open channels, the cross section is not determined entirely by the solid boundaries but is free to change. The study of open channel flow would be incomplete without knowledge of the surface level. Consideration was therefore given to ways of measuring surface levels with the instrumentation originally designed for velocity profile measurement. For this purpose, separate test runs were conducted to find the most favorable setup for the measurement of surface levels. The data were then processed with the programs Microsoft Excel and The Mathworks Matlab to generate plots of the surface level over time.

The experimental setup for the surface level measurements is shown on the left side of Figure 5-6. Again, the transducer was used at the end of the test channel, where it was inserted from above the water facing the direction of flow. The largest part of the measurements were made with the 4-MHz transducer, but a 2-MHz transducer (type TN2-10-13) was used as well. The axis of the transducer was placed at three different angles to the surface of the water. The water temperature was found to remain constant at 15°C (speed of sound  $c = 1466$  m/s).

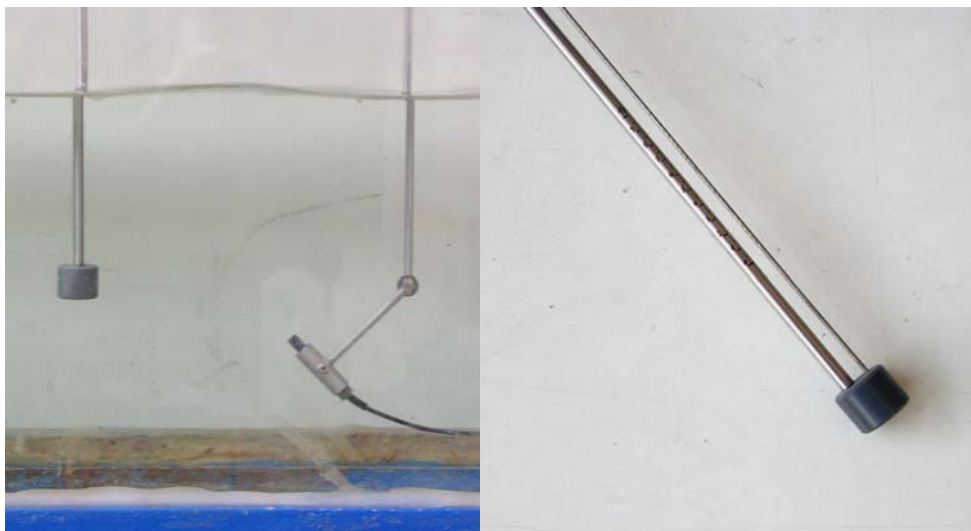


*Figure 5-6: Experimental setup for surface level measurements (left) and Fafnir probe (right).*

The surface level was simultaneously measured by an electrical conductivity method using a pair of parallel wire electrodes (Fafnir probe). The probe, shown on the right side of Figure 5-6, was placed in the flow so as to measure the surface level at the same position as the UVP-Monitor. A computer sampled the voltage generated and converted the data into a digital representation which could then be used to present the data.

| Angle<br>$\gamma$<br>[°] | Window Parameters |                 |                |                 | Signal Parameters |           |                 | RF Gain      |            |
|--------------------------|-------------------|-----------------|----------------|-----------------|-------------------|-----------|-----------------|--------------|------------|
|                          | First Ch<br>[mm]  | Ch Dist<br>[mm] | End Ch<br>[mm] | Max Dep<br>[mm] | Cyc/Pulse<br>[-]  | NL<br>[-] | Rep/Prof<br>[-] | Start<br>[-] | End<br>[-] |
| 90                       | 203.0             | 0.73            | 296.9          | 299             | 2                 | 0         | 8               | 1            | 1          |
| 75                       | 203.0             | 0.73            | 296.9          | 299             | 2                 | 0         | 8               | 1            | 5          |
| 60                       | 203.0             | 0.73            | 296.9          | 299             | 2                 | 32        | 8               | 1            | 8          |
| 90*                      | 169.3             | 0.73            | 263.1          | 394             | 2                 | 32        | 8               | 1            | 1          |

Table 5-3: Software parameters as applied to the surface level measurements with the UVP-MFX 2.0 program.

The software parameters, as applied to the surface level measurements, are shown in Table 5-3. The 2-MHz measurement is indicated by an asterisk (\*). The width of the measurement window (Ch Dist) was specified so as to cover only the area of interest, i.e., the moving surface of the water. Both the pulse length (Cyc/Pulse) and the number of profile repetitions (Rep/Prof) were set to their allowed minima to reduce the size of the sample volumes (higher spatial resolution), respectively, to increase the speed at which the profiles were measured (higher temporal resolution). The most advantageous settings for the amplification of the echo signal (RF Gain) and the noise level filter (NL) were found through trial and error.

The spatial and temporal resolution for the surface level measurements are summarized in Table 5-4. The small time interval between successive profile measurements allowed an accurate measurement of the rapidly changing surface level. The number of recorded profiles was selected so as to provide enough data for the comparison with the Fafnir probe.

| Angle<br>$\gamma$<br>[°] | Resolution           |   |  | Number<br>of<br>Profiles<br>[-] | Total<br>Measurement<br>Time<br>[s] |
|--------------------------|----------------------|---|--|---------------------------------|-------------------------------------|
|                          | Spatial<br>w<br>[mm] | Temporal<br>$\Delta t_{\text{theor}}$<br>[ms] | Temporal<br>$\Delta t_{\text{meas}}$<br>[ms] |                                 |                                     |
| 90                       | 0.37                 | 3.3   | 6.1  | 1000                            | 6.1                                 |
| 75                       | 0.37                 | 3.3   | 6.1  |                                 | 6.1                                 |
| 60                       | 0.37                 | 3.3   | 6.3  |                                 | 6.3                                 |
| 90*                      | 0.73                 | 3.3   | 7.0  |                                 | 7.0                                 |

Table 5-4: Spatial and temporal resolution of surface level measurements.

The results of the experiments are displayed on the following pages. The color plot at the top of each page shows the movement of the surface. The diagram at the bottom of each page compares the surface level obtained by the UVP-Monitor with data from the Fafnir probe. Note that the color plot shows only part of the measurement (profiles 0 – 711) due to a limited screen resolution of the review software.

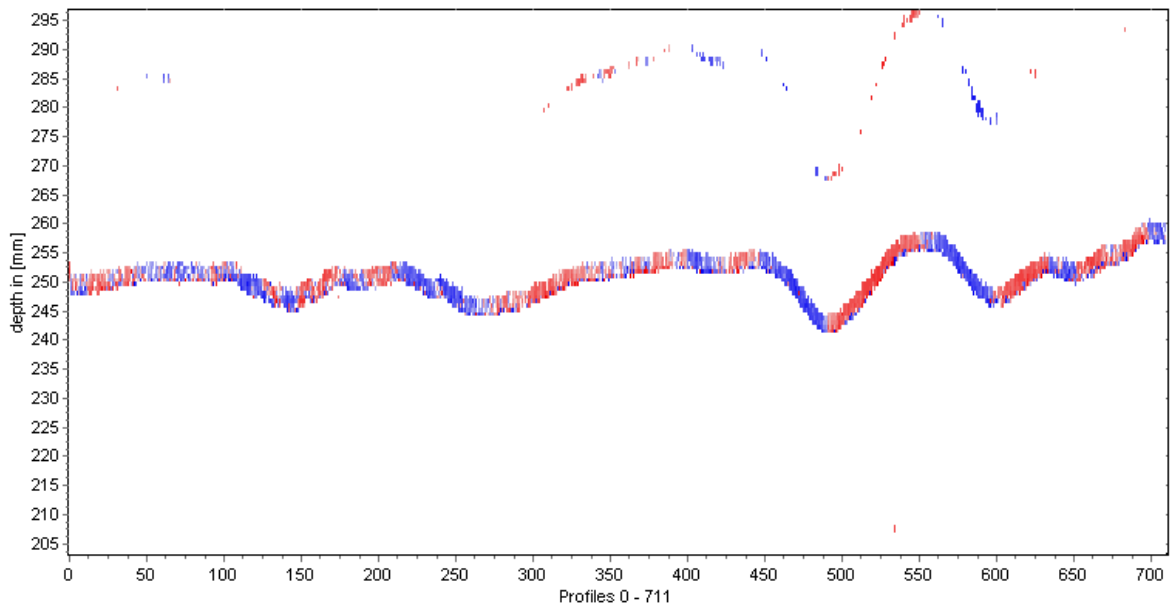


Figure 5-7: Color plot of surface level measurement completed at an angle of  $90^\circ$  to the surface (4 MHz).

Figure 5-7 and Figure 5-8 show the results for the transducer axis placed perpendicular to the surface, i.e., normal to the direction of flow. Due to this transducer arrangement, the up and down movement of the surface is converted into the well-known red and blue color combination indicating the flow direction. Note that an additional signal partly follows the original surface movement. Interestingly, this signal has twice the value of the original movement.

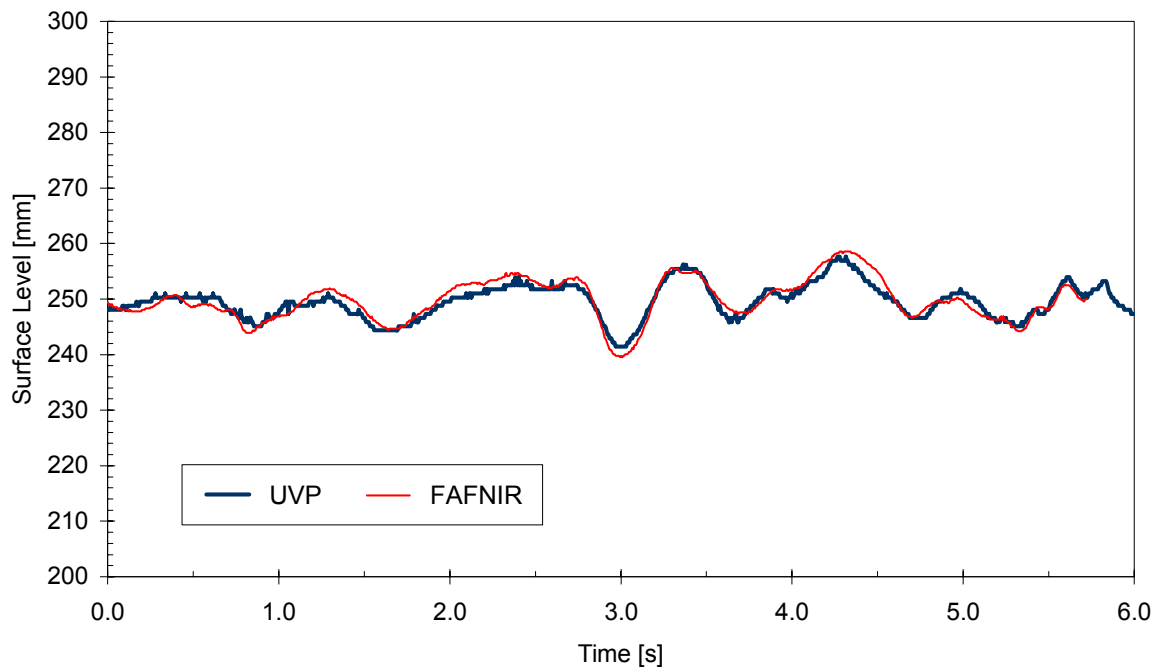


Figure 5-8: Comparative diagram showing the above plot and the output of the Fafnir probe.



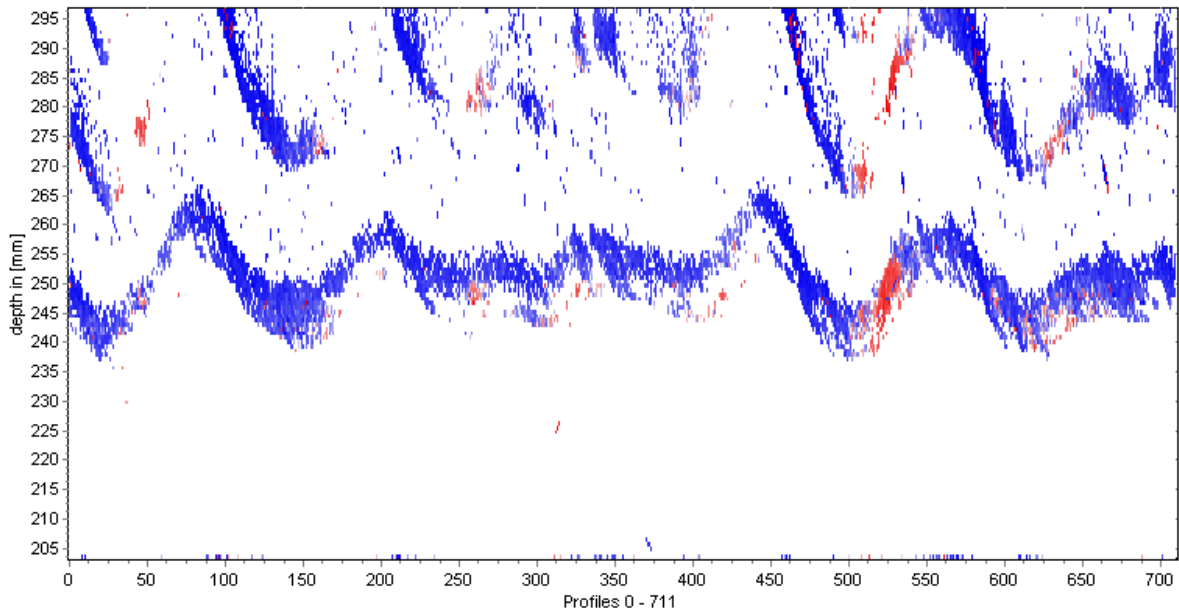


Figure 5-9: Color plot of surface level measurement completed at an angle of  $75^\circ$  to the surface (4 MHz).

Figure 5-9 and Figure 5-10 present the measurement results for the transducer axis placed at an angle of  $75^\circ$  to the flow direction. Zero flow was detected because of the poor particle concentration inside the test channel. This absence of echo signals, on the other hand, makes the surface identification easier. As the surface of the water is not recorded as sharply as in the previous figures, the measurement is found to be less precise, as indicated in Figure 5-10.

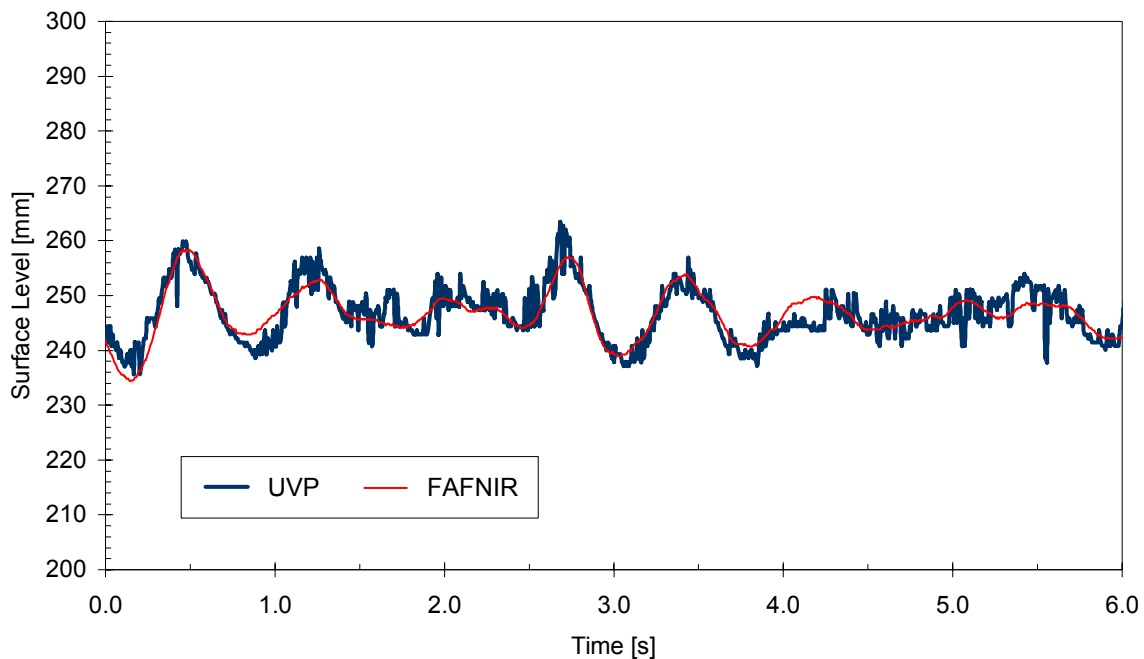


Figure 5-10: Comparative diagram showing the above plot and the output of the Fafnir probe.

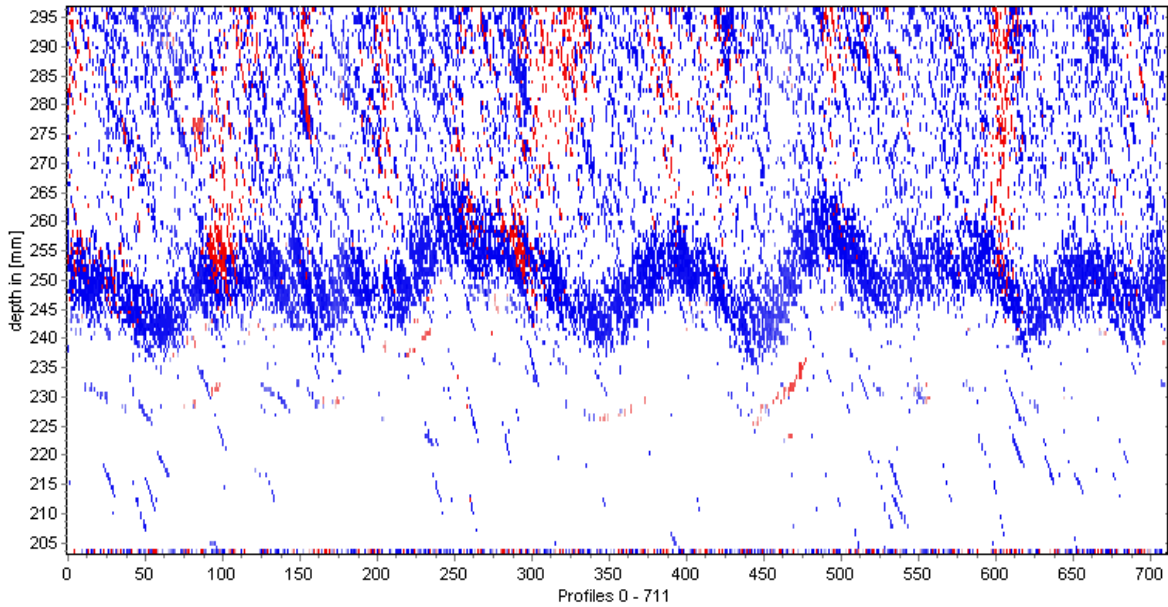


Figure 5-11: Color plot of surface level measurement completed at an angle of  $60^\circ$  to the surface (4 MHz).

Figure 5-11 and Figure 5-12 display the measurement results for the transducer axis placed at an angle of  $60^\circ$  to the flow direction. The position of the free surface can still be recognized within the color plot. However, Figure 5-12 shows poor agreement between the UVP data and the surface level obtained by the Fafnir probe. This is related to the fairly simple method that was used for the computerized identification of the surface in the profile data.

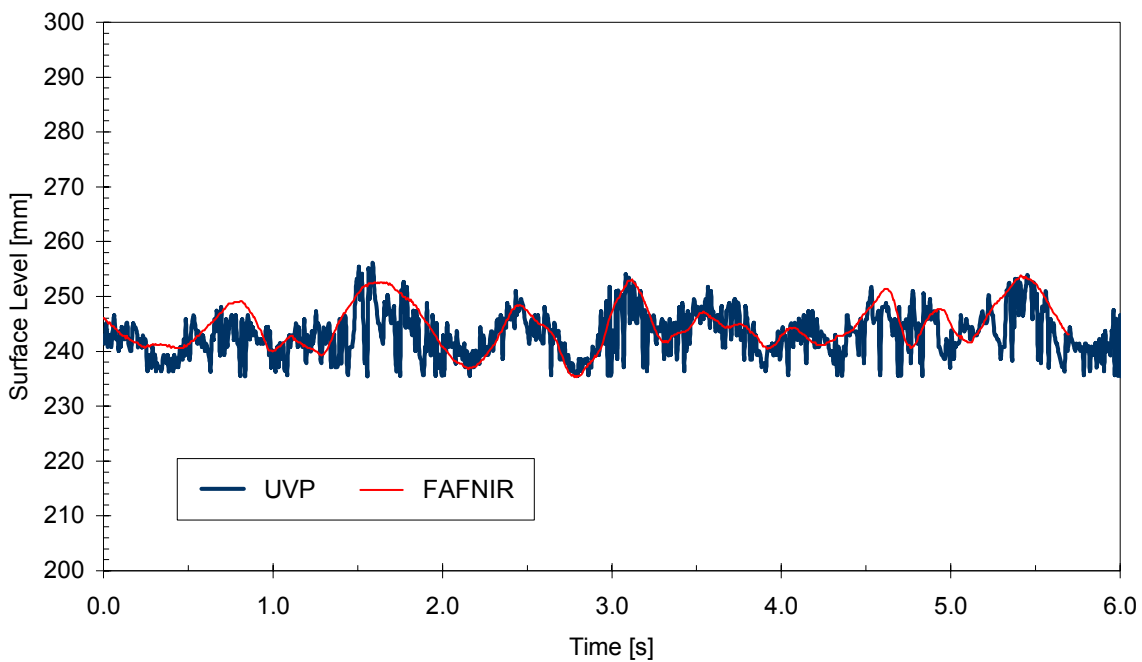


Figure 5-12: Comparative diagram showing the above plot and the output of the Fafnir probe.

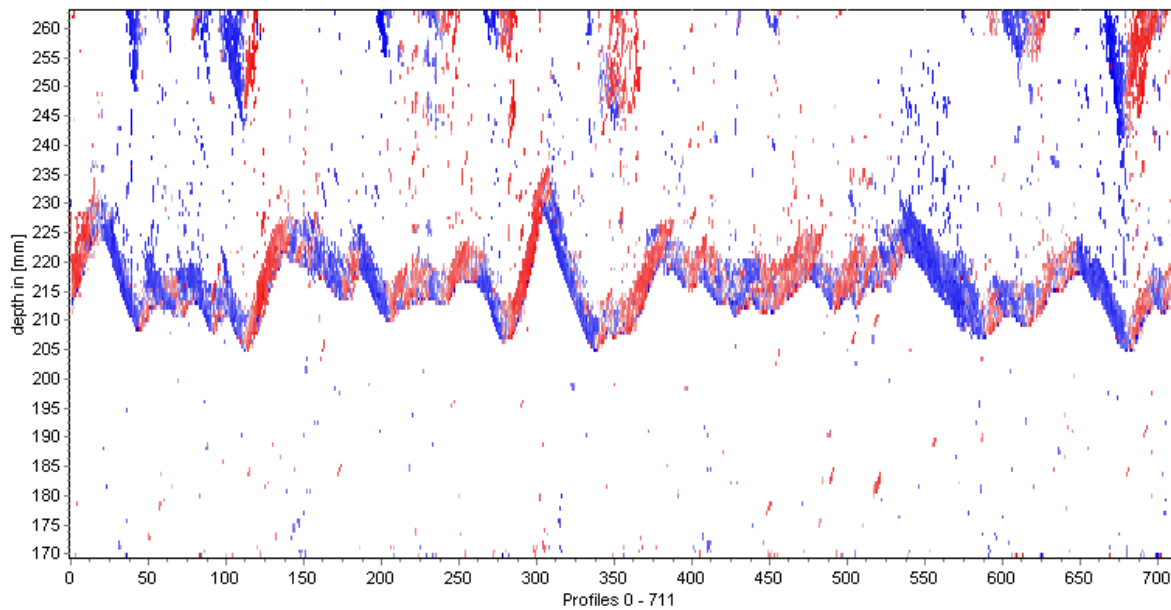


Figure 5-13: Color plot of surface level measurement completed at an angle of  $90^\circ$  to the surface (2 MHz).

Figure 5-13 shows the measurement made with the 2-MHz transducer. Due to technical problems the Fafnir probe did not record the surface level correctly. Thus a comparative diagram cannot be provided. Nevertheless, the color plot indicates that the 2-MHz transducer may be used for surface level measurements as well.

Compared to the results described previously, the color plot in Figure 5-13 looks somewhat compressed. This distortion is related to the slightly increased time interval between successive profile measurements. As the measurement speed is reduced, a longer period will be displayed within the color plot. Another difference to the 4-MHz measurement completed at the same angle (Figure 5-7) is the appearance of echo signals in the flow. These signals make the computerized method for the surface identification more erroneous.

This surface identification method is based on the assumption that channels unequal zero velocity will indicate the position of the free surface if the transducer detects no echo but the surface. By examining the profile data channel by channel, the surface level can be established. Echoes from traveling particles disturb this process and may lead to false results. The described method was put into practice for the making of the comparative diagrams shown on the previous pages. After the obtained profile data were saved as text-files (ASCII), they were transferred to Microsoft Excel. Starting at channel zero, a program then searched for the first channel that did not have zero velocity and replaced its value by a specific number (999). This number allowed the identification of the surface level.

---

## 5.5 Summary

---

Free-surface flow in a glass-walled channel was investigated experimentally using the UVP-Monitor model XW-3-PSi. The instrument performed measurements of both flow velocity and surface level. In each case, the ultrasonic transducer was inserted from above the surface of the water and faced the direction of flow, with the axis of the transducer placed at different angles to the free surface.

To evaluate accuracy, the velocity profile measurements made by the UVP-Monitor were compared to samples from a conventional current meter. For the most part, the two devices were found to be in good agreement. However, the closer the measurements were to the bottom of the channel, the less the data corresponded, which is caused by disturbances in flow near the ultrasonic transducer. Unfortunately, the measurements of the UVP-Monitor were additionally affected by multiple ultrasound reflections between the free surface and the bottom of the channel. These reflections caused characteristic velocity drops within the obtained profiles, known as artifacts. A method was devised to identify these artifacts, thereby differentiating them from velocity drops that may indicate, for instance, the free surface.

The study of open channel flow was concluded by employment of the UVP-Monitor in measurements of surface level. For this purpose, a computerized method was developed to identify the position of the free surface within the measurement window. The data from the identification process was compared to an electrical conductivity method for the measurement of surface level, showing good agreement if the transducer axis is placed perpendicular to the flow direction. Other measurement angles were tested as well, but the identification of the surface level was found to be less precise.

---

## 6 Conclusions and Recommendations

---

The experiments that were performed during the writing of this thesis have revealed a variety of important considerations for successful velocity profile measurements. These considerations mainly include a sufficient concentration of reflecting particles, the absence of artifacts, and an appropriate selection of the angle of incidence:

- The *particle concentration* in the glass-walled channel was found to be sufficient for the measurement of velocity profiles. In the pipe flow experiments, however, the loss of ultrasound energy at the pipe wall had to be compensated for by adding sediment to the flow. The seeding process required additional time and effort to complete the measurements but was essential for establishing entire velocity profiles. Difficulties may arise with wall materials that offer a substantially lower transmission coefficient than Plexiglas (e.g. glass).
- Interference patterns caused by ultrasound reflections (*artifacts*) affected the measurements significantly. The rate at which the patterns occurred was influenced by the type of flow investigated: more than one artifact hardly ever occurred in the pipe flow experiments, whereas the study of free-surface flow was characterized by the regular appearance of numerous profile distortions. The investigation of flow with a free surface is thus affected more easily by ultrasound reflections. The severity of the profile distortions appears to vary with the angle to the free surface.
- When performing non-invasive measurements, the *angle of incidence* is limited to angles below the critical angle. Small angles of incidence, however, are known to be sensitive to angle uncertainties that can lead to errors in the computation of velocity. The angle of incidence as applied in the pipe flow experiments ( $\theta_i = 10^\circ$ ) appears to be a good selection for the flow speeds measured ( $v_{max} \approx 1$  m/s). This finding is confirmed by the accurate computation of the pipe discharge from the velocity profiles obtained (error 1.9 %).

Since the whole measurement process is controlled via software, careful consideration is essential in specifying the software parameters. The multitude of possible parameter combinations first appears confusing, but familiarity can be gained over time. However, the software cannot compensate for mistakes that have been made in the experimental setup, for instance, selection of an inappropriate transducer frequency.

The experiments conducted have demonstrated the successful application of the ultrasound-pulse-Doppler method in the field of experimental hydraulics. The following recommendations can be given concerning future investigations of pipe flow and free-surface flow:

- A frequency of 2 MHz instead of 4 MHz should be used to investigate the effects of frequency variation in measurements. The echo conditions are likely to improve as the size of the sample volumes increases and more particles contribute to the frequency shift detected. The use of a low-frequency transducer could thus be a potential alternative to the time-consuming process of flow seeding. Low frequencies should particularly be used when performing non-invasive measurements on wall materials other than Plexiglas.
- Further test runs are recommended to clarify the formation of artifacts. In the study of open channel flow, absorbing material may be placed on the bottom of the channel, as suggested by [20]. Artifacts may also be reduced by particle seeding, because low SNR (signal-to-noise ratio) caused by poor particle concentration is considered to promote the occurrence of artifacts. However, flow seeding cannot avoid profile modifications completely, as the pipe flow experiments indicate.
- Simultaneous measurements of surface level and flow velocity were prevented by the opposing requirements for the positioning of the transducer. For the measurements of velocity profiles, the transducer axis may not be placed perpendicular to the flow direction, whereas measurements of surface level provide the most promising results at this specific position. A more sophisticated method for the identification of the free surface within the profile data may solve this problem.

---

## 7 References

---

- [1] AMERICAN SOCIETY OF NONDESTRUCTIVE TESTING (1991): *Nondestructive Testing Handbook, Volume 7: Ultrasonic Testing*. Second edition, ASNT, Columbus (USA). [www.asnt.org](http://www.asnt.org)
- [2] ANDERSON, M. E. and TRAHEY, G. E. (April 2000): *A Seminar on k-Space applied to Medical Ultrasound*. Department of Biomedical Engineering, Duke University, Durham (USA). <http://dukemil.egr.duke.edu/ultrasound/k-space/bme265.pdf>
- [3] ANGELSEN, B. A. J. (2000): *Ultrasound Imaging – Waves, Signals and Signal Processing*. First edition, Emantec, Norway. [www.ultrasoundbook.com](http://www.ultrasoundbook.com)
- [4] DE CESARE, G. and SCHLEISS, A. (August 1999): Turbidity current monitoring in a physical model flume using ultrasonic Doppler method. *Proceedings of the International Association for Hydraulic Research (IAHR), 28th Biannual Congress, Graz 1999*. [www.iahr.org/membersonly/grazproceedings99/pdf/D096.pdf](http://www.iahr.org/membersonly/grazproceedings99/pdf/D096.pdf)
- [5] DOBLER, R. (1997): “Durchfluss- und Geschwindigkeitsmessungen bei Rohrströmungen in der Hydraulik mit einem Ultraschallverfahren”. Diploma Thesis, Department of Foundations of Machine Design, Johannes Kepler University of Linz. <http://aml.jku.at>
- [6] FARAN, J. J. (1951): Sound scattering by solid cylinders and spheres. *Journal of the Acoustical Society of America*, Vol 23, pp 405-418. <http://asa.aip.org>
- [7] GOLDSTEIN, A. and POWIS, R. L. (1999): Medical Ultrasonic Diagnostics. In: *Ultrasonic Instruments and Devices: Reference for modern Instrumentation, Techniques, and Technology*. First edition, Academic Press, San Diego.
- [8] GONDARD, C. and FLEURY, G. (1995): Improvements of ultrasonic inspections through the use of piezo composite transducers. *Proceedings of the Sixth European Conference on Non-Destructive Testing (ECNDT), Nice 1994*. [www.ndt.net/article/fleury/fleury.htm](http://www.ndt.net/article/fleury/fleury.htm)
- [9] HE, P. (January 1998): Simulation of ultrasound pulse propagation in lossy media obeying a frequency power law. *IEEE Transactions on Ultrasonics, Ferroelectrics, and Frequency Control*, Vol 45, No 1, pp 114-125. [www.cs.wright.edu/~phe/Research/UFFC-98.pdf](http://www.cs.wright.edu/~phe/Research/UFFC-98.pdf)

- [10] HERMANN-GRENGG LABORATORIES GRAZ (June 2000): “*Modellversuch Düker Oitenbach*”. Report on Hydraulic Model Test Nr. 294.
- [11] IMITZER, P. (2000): “*Messung von Geschwindigkeitsfeldern an einer Verteilrohrleitung (Tri-furcator) mit einem Laser-Doppler-Anemometer*”. Diploma Thesis, Institute of Hydraulic Structures and Water Resources Management, Graz University of Technology.
- [12] INGENIEURBÜRO WÖLFLE (Nov 1999): “*Wasserbautechnisches Projekt Düker Oitenbach*”. Ingenieurbüro Wölfler ZT-GmbH, Salzburg.
- [13] INSTRUMENT SOCIETY OF AMERICA (1991): *Flow Measurement: Practical Guides for Measurement and Control*. ISA, Research Triangle Park (USA). [www.isa.org](http://www.isa.org)
- [14] KRAUTKRÄMER, J. and KRAUTKRÄMER, H. (1986): “*Werkstoffprüfung mit Ultraschall*”. Fifth edition, Springer-Verlag, Berlin.
- [15] LACH, M., PLATTE, M. and RIES, A. (September 1996): Piezoelectric materials for ultrasonic probes. *NDTnet (The E-journal of Nondestructive Testing & Ultrasonics)*, Vol 1, Nr 9. [www.ndt.net/article/platte2/platte2.htm](http://www.ndt.net/article/platte2/platte2.htm)
- [16] LOCTITE (1998): *The Loctite Design Guide for Bonding Plastics, Volume 2*. Loctite Literature LT -2197. [www.loctite.com/literature/design\\_plastic.html](http://www.loctite.com/literature/design_plastic.html)
- [17] LUBBERS, J. and GRAAFF, R. (1998): A simple and accurate formula for the sound velocity in water. *Ultrasound in Medicine and Biology*, Vol 24, No 7, pp 1065-1068.
- [18] MASSEY, B. S. (1989): *Mechanics of Fluids*. Sixth edition, Chapman & Hall, London.
- [19] MET-FLOW (2000): *User's Guide UVP-Monitor UVP-XW*. Second edition, Met-Flow SA, Lausanne. [www.metflow.com](http://www.metflow.com)
- [20] NAKAMURA, H., KONDO, M. and KUKITA, Y. (1996): Simultaneous measurement of liquid velocity and interface profiles of horizontal duct wavy flow by ultrasonic velocity profile meter. *Proceedings of the First International Symposium on Ultrasonic Doppler Methods for Fluid Mechanics and Fluid Engineering (ISUD)*. Paul Scherrer Institute, Villigen (CH). [www.psi.ch/index\\_e](http://www.psi.ch/index_e)



- [21] PANAMETRICS (2001): *Ultrasonic Transducers*. Panametrics Inc., NDT Division, Waltham (USA). [www.panametrics.com/div\\_ndt/pdfs/transducers/catalog.pdf](http://www.panametrics.com/div_ndt/pdfs/transducers/catalog.pdf)
- [22] PEDERSEN, L. (2000): *Spreadsheet of Acoustic Properties*. Specialty Engineering Associates, Soquel (USA). [www.ultrasonic.com/tables/pix/table.zip](http://www.ultrasonic.com/tables/pix/table.zip)
- [23] SELFRIDGE, A. R. (May 1985): Approximate material properties in isotropic materials. *IEEE Transactions on Sonics and Ultrasonics*, Vol 32, No 3, pp 381-387. [www.ultrasonic.com/pix/material.pdf](http://www.ultrasonic.com/pix/material.pdf)
- [24] SHAMES, I. H. (1992): *Mechanics of Fluids*. Third edition, McGraw-Hill, New York.
- [25] SIGNAL PROCESSING (1999): *Introducing DOP Ultrasonic Velocimeter*. Revision 2, Signal Processing SA, Lausanne. [www.signal-processing.com/tech/introducing\\_dop.htm](http://www.signal-processing.com/tech/introducing_dop.htm)
- [26] SIMON, A. L. (1976): *Practical Hydraulics*. First edition, John Wiley & Sons, New York.
- [27] SUTILOV, V. A. (1984): *“Physik des Ultraschalls”*. Second edition, Springer-Verlag, Wien.
- [28] TAKEDA, Y. (1999): Ultrasonic Doppler method for velocity profile measurement in fluid dynamics and fluid engineering. *Experiments in Fluids*, Vol 26, pp 177-178.
- [29] WUNDERLICH, T. and BRUNN, P. O. (2000): A wall layer correction for ultrasound measurement in tube flow: comparison between theory and experiment. *Flow Measurement and Instrumentation*, Vol 11, pp 63-69.